Mass loss in α Scorpii

A hydrodynamic study of the extended envelope of Antares

Dissertation
zur Erlangung des Doktorgrades
des Fachbereichs Physik
der Universität Hamburg

vorgelegt von
Kilian Braun
aus Herdecke

Hamburg
2012

Gutachter der Dissertation:	Prof. Dr. Dieter Reimers Prof. Dr. Rolf-Peter Kudritzki Prof. Dr. Wolf-Rainer Hamann
Gutachter der Disputation:	Prof. Dr. Peter Hauschildt Prof. Dr. Robi Banerjee
Datum der Disputation:	22. Februar 2012
Vorsitzender des Prüfungsausschusses:	Dr. Robert Baade
Vorsitzender des Promotionsausschusses:	Prof. Dr. Peter Hauschildt
Dekan der Fakultät für Mathematik, Informatik und Naturwissenschaften:	Prof. Dr. Heinrich Graener

Zusammenfassung

Masseverlust von Sternen ist ein universelles Phänomen, das sowohl die Sternentwicklung als auch die chemische Zusammensetzung des interstellaren Mediums beeinflusst. Das Verständnis der Mechanismen, die diese Winde bei späten Riesen und Überriesen antreiben, ist jedoch bis heute unzureichend, und es gibt weiterhin einen Bedarf an empirischen Massenverlustraten. In den meisten bisherigen Studien, die sich mit der Bestimmung der Massenverlustrate des Überriesen im α Sco-(Antares-) System (M1 Ib + B2.5 V) beschäftigt haben, wurde angenommen, dass die zirkumstellare Hülle sphärisch symmetrisch expandiert und die Dichteverteilung durch ein einfaches Potenzgesetz beschrieben werden kann. In den vergangenen Jahren haben Beobachtungen gezeigt, dass diese Annahme unhaltbar ist.

Ziel dieser Arbeit ist es, ein realistisches Modell des α Sco-Systems zu konstruieren, um einen quantitativen Einblick in die Dynamik der zirkumstellaren Hülle zu gewinnen. In Kombination mit den verfügbaren Beobachtungen wird dieses Modell zur Bestimmung der Massenverlustrate verwendet.

Beobachtungen mit UVES/VLT bieten die einmalige Gelegenheit, die Linienemission aus der zirkumstellaren Hülle von α Sco, dem Antares-Nebel, mit räumlicher Auflösung zu untersuchen. Diese Beobachtungen werden mit den Ergebnissen einer Kombination aus hydrodynamischen Modellrechnungen und Plasmasimulationen verglichen, die Informationen sowohl über die Emissionsstruktur als auch die Dichte- und Geschwindigkeitsverteilung liefern. Zusätzlich werden aus den Simulationen abgeleitete theoretische Profile von Absorptionslinien im Spektrum von α Sco B mit Beobachtungen verglichen.

Der Vergleich der Beobachtungen mit den Ergebnissen der Modellrechnungen zeigt, dass die in den Absorptionslinien im Spektrum von α Sco B beobachtete Multikomponentenstruktur teilweise aus Dichtestrukturen resultiert, die durch die heiße H II-Region hervorgebracht werden, die sich mit dem B-Stern durch den Wind des Primärsterns bewegt. Darüber hinaus ergibt sich eine nicht-monotone Geschwindigkeitsverteilung, wodurch die Struktur der Linienprofile ebenfalls beeinflusst wird. Die resultierende Massenverlustrate ist $2 \times 10^{-6}\ M_{\odot}\,\mathrm{yr}^{-1}$ und damit doppelt so hoch wie der auf einer sphärisch symmetrisch expandierenden zirkumstellaren Hülle basierende Wert. Die beobachtete [Fe II]-Linienemission kann nicht reproduziert werden, was vermutlich an der vereinfachten Behandlung des Strahlungstransports liegt. Allerdings wird die aus den Absorptionslinien abgeleitete Massenverlustrate durch die komplementäre Analyse der räumlichen Verteilung der beobachteten Hα-Emission bestätigt.

Abstract

Stellar mass-loss is a universal phenomenon that affects the evolution of stars as well as the chemical composition of the interstellar medium. However, the mechanisms that drive these winds in late giants and supergiants are only poorly understood, and there is still a need for empirical mass-loss rates. In most of the previous studies that dealt with the determination of the mass-loss rate of the supergiant in the α Scorpii (Antares) binary system (M1 Ib + B2.5 V) it was assumed that the circumstellar envelope expands with spherical symmetry and its density distribution can be described by a simple power law. In recent years observations have shown that this assumption is untenable.

The goal of this work is to construct a realistic model of the α Sco system in order to gain quantitative insight into the dynamics of the circumstellar envelope. In combination with the available observations, this model is used to determine the mass-loss rate.

Observations with UVES/VLT provide the unique possibility to study the line emission from the circumstellar envelope of α Sco, the Antares nebula, with spatial resolution. These observations are compared to the results of a combination of hydrodynamic and plasma simulations, which give information about the emission structure as well as the density and velocity distribution. In addition, theoretical profiles of absorption lines in the spectrum of α Sco B derived from the simulations are compared to observations.

The comparison of the observations to the results of the model calculations shows that the multi-component structure observed in the absorption lines in the spectrum of α Sco B is partly a result of density structures produced by the hot H II region that is moving with the B star through the wind of the primary star. In addition, the resulting velocity structure is non-monotonic, which also affects the structure of the line profiles. The resulting mass-loss rate is $2 \times 10^{-6}\ M_{\odot}\,\mathrm{yr}^{-1}$, which is twice as high as the value based on a circumstellar envelope that expands with spherical symmetry. The observed [Fe II] line emission cannot be reproduced, which is probably due to the simplified treatment of the radiative transfer. However, the mass-loss rate derived from the absorption lines is confirmed by the complementary analysis of the spatial distribution of the observed Hα emission.

Contents

Chapter 1

Introduction

Knowledge of stellar mass-loss is important in modern astrophysics, in particular in stellar astrophysics. It determines the evolution of the chemical composition of the universe and strongly affects the evolution of stars. On the other hand, the driving mechanisms that are responsible for mass loss are still only partly understood and research in this field holds out the prospect of new insights into the structure and dynamics of the outer layers of stars. Calculations of the late stages of stellar evolution have still to rely on empirical mass-loss rates.

Mass loss enriches the interstellar medium and thus yields the material for future generations of stars and planets. Stellar winds play a major role in this context. When stars leave the main sequence and enter later evolutionary stages they exhibit very high mass-loss rates. The identification of the mechanisms that drive these stellar winds is an ongoing issue, especially in the case of red giants and supergiants.

In a number of theoretical studies different mechanisms have been proposed that are able to drive winds, e. g. Alfvén waves, acoustic waves, shock waves, radiation pressure on dust grains, and pulsations (see the reviews of Lafon & Berruyer 1991; Willson 2000). However, the question which mechanisms drive the wind in red giants and supergiants remains unanswered, and there is still a need for both theoretical and observational studies of the mass-loss processes that occur in these stars.

The study of mass loss from red giants and supergiants is most accurate in binary systems like those of ζ Aur or VV Cep type (see Sect. 2.4.1). The visual binary α Scorpii (Antares) provides the additional advantage that the circumstellar shell can be observed with spatial resolution, which was done by Reimers et al. (2008) with the UVES spectrograph at the VLT. These observations and the absorption lines seen in the HST/GHRS spectra of α Sco B (Baade & Reimers 2007) revealed the presence of asymmetries and density inhomogeneities in the common envelope of α Sco. Therefore, it was suggested that the mass-loss rate is time dependent and the presence of the H II region around α Sco B produces deviations from spherical symmetry.

In this work I present hydrodynamic simulations of the α Sco system calculated with the AMRCART code of Walder & Folini (2000) (see Sect. 5.1), includ-

ing a model of the H II region calculated with the plasma code Cloudy (Ferland et al. 1998). The goal is to achieve new insights into the dynamics and structure of the circumstellar envelope of α Sco and into the various processes producing its complex spectrum. The data resulting from the combination of hydrodynamic and plasma simulations allow a comparison to observations. The hope was to improve the empirical mass-loss rate of α Sco A using both nebula emission lines and absorption lines in the line of sight of α Sco B observed with the VLT and the HST in combination with a dynamical model of the Antares nebula.

After a brief summary of the current state of research concerning stellar mass-loss in Sect. 2 I present results of previous studies of the α Sco system in Sects. 3 and 4. In Sect. 5 I describe the hydrodynamic and plasma simulations of the α Sco system and its H II region. The resulting density and velocity distributions are presented in Sect. 6, and they are compared to observed spectra in Sects. 7 and 8.

Chapter 2

Current state of mass-loss research

Mass-loss processes have been investigated in many different types of stars by means of observations as well as theoretical studies (see e. g. the textbook of Lamers & Cassinelli 1999). For some types of stars, the mechanism that drives the wind has been identified. For example, radiative forces exerted by spectral lines constitute the dominant mechanism that drives the winds of luminous hot stars such as O and B stars (see Sect. 2.2). In cool giants on the asymptotic giant branch (AGB) the driving mechanism is related to pulsations and dust formation (Sect. 2.3).

For most other types of stars, probably combinations of different effects such as large temperature gradients (coronal winds), sound waves, transfer of angular momentum due to magnetic fields (magnetic rotator theory), and Alfvén waves drive the stellar wind. Naturally, the most extensive observational material related to mass loss is available for the Sun. However, the mechanisms driving the solar wind are still not well understood.

After a short discussion of the present knowledge of the solar wind in Sect. 2.1 I briefly outline observational methods and theories related to mass loss in different kinds of hot stars and cool giants in Sects. 2.2 to 2.4 with emphasis on late-type supergiants on the RGB.

2.1 The solar wind

Recent reviews about observations and theories concerning the solar wind were presented by Ofman (2010), who focused on waves as a possible origin of heating and acceleration in the solar wind, and Marsch (2006), who addressed the microphysical aspects of energy dissipation in the solar wind.

The solar wind consists of a slow component with a terminal velocity of $\sim 400\,\mathrm{km\,s^{-1}}$, a fast component at $\sim 800\,\mathrm{km\,s^{-1}}$, and transient coronal mass ejections (CMEs). While the fast wind is steady and originates from coronal holes in the polar region of the Sun, the slow wind is unsteady and typically emerges in the equatorial region at solar minimum. At solar maximum, the solar wind is dominated by the slow component and CMEs.

Parker (1958) proposed a mechanism based on heat conduction that produces a steady wind. His model constitutes a coronal wind that is driven by gas pressure. He showed that a hot corona that is maintained at a temperature of $T_0 \sim 2 \times 10^6$ K produces a wind with a terminal velocity of $\sim$ 500 km s^{-1} and a mass-loss rate of $\sim 5 \times 10^{-13}\ M_\odot\,\mathrm{yr}^{-1}$ (Parker 1960). He used a fixed coronal temperature as a boundary condition and did not make any specific assumption about the mechanisms that are responsible for the heating of the corona.

Later works led to the conclusion that the mechanism proposed by Parker (1958) can explain the observed terminal speed of the slow solar wind, but it cannot yield the observed properties of the fast solar wind. Model calculations showed that Alfvén waves may constitute an additional source of acceleration of the coronal plasma to produce the fast solar wind (see e. g. Suzuki & Inutsuka 2005).

The explanation of the observed properties of the solar wind remains a research area with many open questions. The mechanisms driving the solar wind probably involve magnetohydrodynamic (MHD) as well as kinetic plasma waves and associated wave-particle interactions (Marsch 2006). The remaining open questions relate to the role of plasma and MHD waves, small-scale turbulence, and electrons for the heating and acceleration of the solar wind, as well as to the velocity distributions of protons and ions in the slow and fast solar wind (Ofman 2010).

2.2 Winds of luminous hot stars

Comparisons of observations and theoretical models showed that the mass loss of luminous hot stars is driven by spectral-line photons that are absorbed in the atmosphere of the stars, thereby transferring momentum to the absorbing particles. This led to the so-called CAK theory, which was developed by Castor et al. (1975) for O-type stars. Later improvements of the theory showed that the model of a line-driven wind is also consistent with observations of B and A supergiants (see e. g. Pauldrach et al. 1986; Curé et al. 2011), but there are discrepancies in the case of Wolf-Rayet (WR) stars. The contemporary theory of line-driven winds yields precise predictions of the mass-loss rate as a function of stellar parameters and also reproduces the observed dependence on metallicity (see also the reviews of Lamers 1997; Kudritzki & Puls 2000; Puls et al. 2008).

Empirical mass-loss rates and wind velocities for hot stars are based on observations of P Cyg profiles in the UV, Hα emission, free-free emission in the radio region, and lines or continua at radio, submillimeter, or IR wavelengths. These observational data are then combined with detailed simulations of non-LTE model atmospheres (Kudritzki & Puls 2000).

Observations of WR stars seem to indicate mass-loss rates that are much higher than the corresponding theoretical values (see e. g. Barlow et al. 1981; Gräfener & Hamann 2008). However, the recent study of Vink et al. (2011), based on Monte Carlo radiative transfer models, apparently resolves this contradiction.

2.3 Winds of cool stars

The mechanisms driving mass loss in cool giants are only partly understood. For asymptotic-giant-branch (AGB) stars, including Mira and OH/IR stars, there is a correlation between the pulsation period and the mass-loss rate, and the stellar wind appears to be caused by the interplay of pulsations, dust formation, and radiation pressure on dust grains.

The mechanism responsible for mass loss in red-giant-branch (RGB) stars is unknown. Computer programs that simulate stellar evolution of RGB stars normally include mass loss in the form of semi-empirical formulas relating the mass-loss rate to basic stellar parameters (cf. the review of Willson 2009), many of which are based on the formula proposed by Reimers (1975), which has the form $\dot{M} \propto L/(gR)$, where $\dot{M}$ is the mass-loss rate, L the luminosity, g the surface gravity, and R the radius of the star.

There have been various theoretical approaches trying to explain the generation of mass loss in cool giants (see the review of Willson 2000). Acoustical and Alfvén waves might play an important role in generating the outflow. The driving mechanism is probably related to pulsations that cause shock waves in the outer layers of the star. Other effects of pulsations are mechanical heating, and an enhancement of the density scale-height h, both of which cause or facilitate the escape of material from the gravitational potential of the star. The density scale-height is defined as

$$h = \left[\frac{\mathrm{d}(\ln \rho)}{\mathrm{d}r} \right]^{-1}, \tag{2.1}$$

where ρ is the density and r the radial distance to the star.

For single cool stars mass-loss rates can be obtained by observing the infrared (IR) continuum emission caused by the dust that is formed in the outflowing gas. For the determination of the corresponding velocity, observations of CO lines in the radio region can provide velocity information (Lamers & Cassinelli 1999). The most accurate determinations for RGB stars are based on the binary technique (see Sect. 2.4.1).

2.4 Measuring mass-loss rates of late-type supergiants

Mass-loss rates of late-type supergiants can be determined on the basis of profile fits of absorption or P Cyg-type lines in their spectra. The authors of most studies assume that the distributions of the density and the velocity are radially symmetric in the circumstellar shell, i. e.

$$\dot{M} = 4\pi r^2 v(r) \rho(r), \tag{2.2}$$

where r is the radial distance to the supergiant, and $v(r)$ and $\rho(r)$ the velocity and mass density, respectively. In analogy to the winds in luminous hot stars, the

velocity can be expressed as the β power law

$$v(r) = v_\infty \left(1 - \frac{R_0}{r}\right)^\beta , \tag{2.3}$$

which leads to the expression for the density

$$\rho(r) = \rho_0 \left(\frac{R_0}{r}\right)^2 \left(\frac{r}{r - R_0}\right)^\beta \tag{2.4}$$

with

$$\rho_0 = \frac{\dot{M}}{4\pi v_\infty R_0^2} \tag{2.5}$$

(cf. Baade 1998).

The measured column densities equal the integral of the density over the line of sight and depend sensitively on the lower bound of integration, i. e. the inner radius R_i of the circumstellar envelope, which is normally not known. When the supergiant has a companion as an additional light source illuminating the circumstellar envelope, this problem can be solved as shown in the next section.

2.4.1 The binary technique

The mass-loss rates of supergiants that are part of binary systems with companion stars of main-sequence type can be determined with high accuracy and a minimum of model parameters as outlined in the review of Reimers (1987b) (see also Reimers 1987a). If the circumstellar envelope is observed in the spectrum of the secondary star, the problem of determining the inner radius R_i of the circumstellar envelope does not arise, and the boundary of the observed circumstellar material is given by the position of the secondary, which can be determined by radial velocity measurements covering the whole orbit or by direct measurement of the angular separation.

Deutsch (1956) was the first who took advantage of the binary character of a stellar system in the study of mass-loss processes. He found absorption features in the spectrum of the M-type supergiant α Her as well as in the spectrum of its visual companion, a spectroscopic binary of type G.

When it is based on UV observations, this method is also called the "UV binary technique" (Baade et al. 1996b) and has been applied successfully to a number of ζ Aur- and VV Cep-type binaries. It takes advantage of the fact that the spectrum of a late-type supergiant has its maximum in the near infrared, whereas the maximum of the spectrum of a hot main-sequence star is situated in the UV. Thus, the UV spectrum of the secondary is not contaminated by the primary. ζ Aur-type stars are supergiants of type G or K with main-sequence companions of type A or B, and the components of VV Cep-type stars are of type M and B, respectively.

Kudritzki & Reimers (1978) and Hagen et al. (1987) applied the binary technique to the α Sco system on the basis of optical and UV observations, respectively (see Sect. 4.1).

Chapter 3

System parameters of α Sco

α Scorpii (α Sco, Antares) is a visual binary system consisting of an M1 Ib-type red supergiant and a B2.5 V-type dwarf, and its distance is $d = 185^{+84}_{-44}$ pc according to the Hipparcos catalogue (ESA 1997). Van Leeuwen (2007) finds $d = 170^{+35}_{-25}$ pc in his new reduction of the raw Hipparcos data, but the earlier value, which is consistent with the distances adopted in most studies of the α Sco system, is used in this work. Hopmann (1958) determined the inclination of the orbit and found $i \sim 90°$. However, this value is rather uncertain. The angular separation is 2.″73 and the B star is ∼ 224 AU behind the supergiant, which corresponds to a position angle $\delta = 23 \pm 5°$ (Reimers et al. 2008). The M star loses mass and creates an envelope containing the whole system. The B star illuminates this envelope and creates an H II region and the so-called Antares nebula.

According to Kudritzki & Reimers (1978) the effective temperature of the B star is $T_{\rm eff} = 18\,500 \pm 1500$ K, and its surface gravity is $\log g = 3.9 \pm 0.2$ (in cgs units). These values result from profile fits of Balmer and He I lines, and the mass $M_{\rm B}$ of the B star was determined by a comparison of these values with theoretical evolutionary tracks, yielding $M_{\rm B} = 7.2 \pm 0.5\ M_\odot$ and $R_{\rm B} = 5.2 \pm 1.3\ R_\odot$. Applying more recent evolutionary models (Bressan et al. 1993) gives similar results, i. e. $M_{\rm B} = 6.7 \pm 0.7\ M_\odot$ and $R_{\rm B} = 4.8 \pm 1.1\ R_\odot$. Brott et al. (2011) presented calculations including rotational effects. Their evolutionary sequence for $7\ M_\odot$ and $v_{\rm rot} = 284$ km s^{-1} matches the surface gravity and effective temperature derived for α Sco B by Kudritzki & Reimers (1978), who observed a projected rotational velocity of $v_{\rm rot} \sin i = 250$ km s^{-1} (see Fig. 3.1). Based on these results and the analysis of Hjellming & Newell (1983) (see Sect. 5.2.2), I adopted $T_{\rm eff} = 18\,200$ K.

For the mass of α Sco A I adopted the value $M_{\rm A} \sim 18\ M_\odot$ found by Kudritzki & Reimers (1978). Table 3.1 lists the system parameters used in this work. The values of d and the position angle δ yield the semi-major axis, for a circular orbit, $D \sim 549$ AU.

Table 3.1: System parameters of α Sco used in this work.

Parameter	Value
$T_{\mathrm{eff,B}}$	18 200 K
$\log g$	3.9 (cgs)
d	185 pc
M_{B}	6.7 $M_{\odot}$
M_{A}	18 $M_{\odot}$
R_{B}	4.8 $R_{\odot}$
δ	$23 \pm 5°$
Separation from A (in 2006)	$2\farcs73$
$\sin i$	1

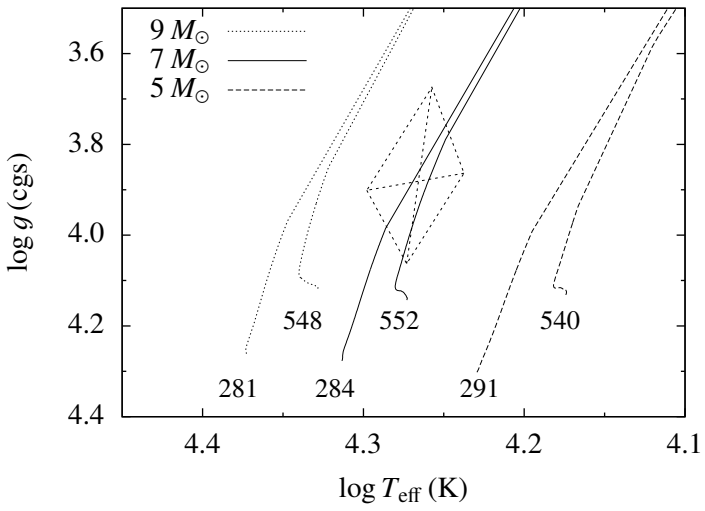

Figure 3.1: Evolutionary tracks calculated by Brott et al. (2011) for different initial masses. The dashed quadrangle shows the observational constraints on $\log g$ and T_{eff} derived by Kudritzki & Reimers (1978). The labels of the curves give the corresponding rotational velocity v_{rot} (km s^{-1}) on the zero-age main sequence.

Chapter 4

Previous studies of mass loss in α Sco

4.1 The rate of mass loss

The mass-loss rate of α Sco has been determined by many authors. In the earlier works, information about the mass loss was obtained by analyzing observations of circumstellar absorption lines in the spectrum of the supergiant (see Sanner 1976a,b; Bernat 1977). Later work took advantage of satellite-borne telescopes that provided access to circumstellar absorption lines in the UV range of the spectrum of the companion.

Hagen (1978, 1982) observed a number of late-type (super)giants in the optical and infrared range to derive the column densities of gas and dust in their circumstellar envelopes. For α Sco A, with an assumed inner radius of $R_\mathrm{i} = 10\ R_\mathrm{A}$ and $R_\mathrm{A} = 840\ R_\odot$, she found that the dust density ρ_d falls off with the radial distance r according to $\rho_\mathrm{d}(r) \propto r^{-2}$, and deduced a total mass-loss rate of $10^{-6}\ M_\odot\,\mathrm{yr}^{-1}$.

Kudritzki & Reimers (1978) analyzed photospheric absorption lines and circumstellar absorption lines (mainly Ti II mult. 1 and 2) in the spectrum of α Sco B, as well as emission lines of the Antares nebula and constructed a model of the system that yielded $\dot{M} = (7 \pm 3.5) \times 10^{-7}\ M_\odot\,\mathrm{yr}^{-1}$. They adopted a configuration with the B star at 629 AU in front of the plane defined by the supergiant, and a spherically symmetric density distribution around the supergiant. They concluded that the H II region created by the B star inside the circumstellar envelope is unlimited in the direction of the observer.

Van der Hucht et al. (1980) presented observations of circumstellar lines in the spectrum of α Sco B in the UV range obtained with the Balloon-borne Ultraviolet Stellar Spectrometer (BUSS) and deduced $\dot{M} = (7.1 \pm 3.5) \times 10^{-6}\ M_\odot\,\mathrm{yr}^{-1}$. They also assumed a spherically symmetric density distribution and found that the position of the B star is 783 ± 261 AU in front of the plane of the M star. The H II region in their model is bounded in all directions.

Bernat (1982) observed the absorption spectrum of α Sco B with the International Ultraviolet Explorer (IUE) and pointed out that the mass-loss rate depends on which element is chosen to derive it. He gives a mean value of $\dot{M} = 6.4 \times 10^{-6}\ M_\odot\,\mathrm{yr}^{-1}$. Hjellming & Newell (1983) observed the Antares

Table 4.1: Previous determinations of the mass-loss rate of α Sco A

Author(s)	Analyzed spectrum	$\dot{M}$
Sanner (1976a,b)	Optical absorption lines	$\gtrsim 1$
Bernat (1977)	Optical absorption lines (3200-5000 Å)	22
Kudritzki & Reimers (1978)	Ti II mult. 1 and 2 absorption lines	7 ± 3.5
Van der Hucht et al. (1980)	Various UV absorption lines (BUSS)	71 ± 35
Bernat (1982)	Various UV absorption lines (IUE)	64
Hjellming & Newell (1983)	Radio emission (VLA)	20
Hagen et al. (1987)	Unblended P Cyg-type UV-lines (IUE)	10
Haas et al. (1995)	IR emission ([O I] 63 μm, [Si II] 35 μm)	130
Baade & Reimers (2007)	UV absorption lines (HST/GHRS)	3; 100
Reimers et al. (2008)	Hα emission (VLT/UVES)	10 ± 3

Notes. The mass-loss rate $\dot{M}$ is given in units of $10^{-7}\ M_\odot\,\mathrm{yr}^{-1}$. The UV absorption lines as well as the Ti II lines analyzed by Kudritzki & Reimers (1978) refer to observations of α Sco B, while the other optical and IR lines were observed in the spectrum of α Sco A. The two mass-loss rates determined by Baade & Reimers (2007) represent the continuous part and the time-averaged rate due to episodic events, respectively.

emission nebula with the Very Large Array (VLA) and derived the mass-loss rate of α Sco A based on the spatial extent of the radio emission, which yielded $\dot{M} = 2 \times 10^{-6}\ M_\odot\,\mathrm{yr}^{-1}$.

Hagen et al. (1987) showed that blends with interstellar lines must be considered in mass-loss determinations that are based on circumstellar absorption lines in the UV spectrum of the B star. They pointed out that the lines that remain after excluding blended lines have P Cygni (P Cyg) profiles, for which appropriate radiative transfer calculations have to be performed in the analysis. They found $\dot{M} \sim 10^{-6}\ M_\odot\,\mathrm{yr}^{-1}$.

Observations of infrared fine-structure emission lines with the Cryogenic Grating Spectrometer (CGS) aboard the Kuiper Airborne Observatory (KAO) served as an indicator for the amount of mass in the wind-acceleration region of α Sco A (Haas et al. 1995). Assuming optically thin emission, the flux in the [O I] 63 μm line was used to derive a mass-loss rate of $1.3 \times 10^{-5}\ M_\odot\,\mathrm{yr}^{-1}$. This value depends on a theoretical temperature distribution in the wind-acceleration region and the assumption that O I is the dominant ionization state in this region.

Baade & Reimers (2007) performed multi-component fits of absorption lines in GHRS/HST spectra of the B star (see next section) and derived a time-averaged mass-loss rate of up to $\dot{M} = 10^{-5}\ M_\odot\,\mathrm{yr}^{-1}$ due to episodic events with a continuous part of $\dot{M} = 3 \times 10^{-7}\ M_\odot\,\mathrm{yr}^{-1}$. The most recent mass-loss determination was carried out by Reimers et al. (2008) and was based on high-resolution spectra obtained with the Ultraviolet and Visual Echelle Spectrograph (UVES) at the Very Large Telescope (VLT). The observed spatial extent of the Hα emission was used to derive $\dot{M} = (1.05 \pm 0.3) \times 10^{-6}\ M_\odot\,\mathrm{yr}^{-1}$.

Table 4.1 gives an overview of the studies mentioned in this section.

4.2 Evidence for inhomogeneous outflow

Sanner (1976b) found multiple components in optical absorption lines in the spectrum of α Sco A. At a resolution of $\lesssim 2\ \mathrm{km\,s^{-1}}$, he observed two components in the Na I mult. 1 lines (Na D), and three components in the K I mult. 1 line at 7698.965 Å, indicating deviations from a smooth outflow scenario.

Mid-infrared observations at the Keck II telescope of the dust in the circumstellar envelope of α Sco indicate a non-uniform dust distribution that appears to be related to discrete ejections of mass from α Sco A (Marsh et al. 2001). This is consistent with interferometric observations that were carried out at the William Herschel Telescope by Tuthill et al. (1997) and revealed asymmetric structures ("hotspots") at the surface of the supergiant.

An analysis of UV absorption lines in the spectrum of α Sco B obtained with the Goddard High-Resolution Spectrograph (GHRS) at the Hubble Space Telescope (HST) revealed that the wind material from the supergiant is concentrated in discrete condensations (Baade 1998; Baade & Reimers 2007). Four absorption systems at distinct velocities were identified.

4.3 Limitations of the current picture of mass loss in α Sco

Many of the previous studies of mass-loss processes in the α Sco system were subject to large systematic errors. In the early works that were based on absorption lines in the spectrum of the supergiant (Sanner 1976a,b; Bernat 1977) and in the analysis of infrared emission lines by Haas et al. (1995) the most important uncertainty was that the results depended on the inner radius R_i of the circumstellar envelope, which cannot be measured exactly (see Sect. 2.4). In the studies that were based on absorption lines in the spectrum of α Sco B (see Table 4.1), the uncertainty resided in the measurement of the locations of the two stars relative to the plane of the sky and their radial velocities.

Baade & Reimers (2007) were able to give a reliable measurement of the relative positions of the two stars based on circumstellar Al III absorption in the spectrum of the B star. They also showed that the abundances of many elements are not constant throughout the circumstellar envelope, which is probably due to differential dust depletion. The presence of multiple components in the observed absorption line profiles rendered it impossible to determine a unique value of the mass-loss rate.

Reimers et al. (2008) presented detailed observations of the line emission that is mostly associated with the H II region around the B star, which yielded precise information with spatial resolution about the complex density structure. Their analysis included a theoretical model of the H II region that was based on a spherically symmetric density distribution given by Eq. 2.4, which can only be regarded as a first approximation and probably does not yield a realistic picture of the physical properties of the emission nebula. Most notably, the complex structure seen

in the Fe II emission lines could not be explained with this simplified model of the circumstellar envelope.

The most recent observations of the α Sco system revealed that its circumstellar envelope is characterized by complex dynamics that lead to large-scale density inhomogeneities (see previous section). These findings show that the mass loss in α Sco can only be completely understood if hydrodynamic effects are included in the analysis of the observed spectrum, and that is the aim of my work. In this work I focus on the hydrodynamics and neglect possible advection effects in the treatment of ionization (see Sect. 6.4 for a discussion), which may be the subject of future research.

Chapter 5

Simulation of the circumstellar envelope of α Sco

5.1 Hydrodynamic simulations

For the simulation of the hydrodynamic effects occuring in α Sco I have chosen the AMRCART code. AMRCART is part of the A-MAZE package (Walder & Folini 2000), which comprises MHD and radiative transfer codes. For my work I used the pure hydro version of AMRCART that is designed to solve the Euler equations with source terms in three dimensions. It uses a finite-volume integrator based on a modified Lax-Friedrichs approach (cf. Barmin et al. 1996), which is outlined in Sect. 5.1.2, and the adaptive mesh refinement (AMR) algorithm developed by Berger & Colella (1989) (see Sect. 5.1.3).

The AMRCART code has been extensively tested in the context of binary stars with colliding winds (see e. g. Walder & Folini 2003). Unfortunately, it cannot be run in parallel on modern HPC clusters. It is written in FORTRAN 77, but I rewrote parts of the code to introduce some features provided by more modern Fortran standards such as modules and allocatable arrays, which improved the user interface and made it possible to allocate arbitrary amounts of memory to the large array that is used by AMRCART for storing the variables at all grid points.

5.1.1 Basic equations

The Euler equations govern the dynamics of compressible, nonviscous fluids for which heat conduction can be neglected (Toro 2009, p. 2). In differential conservative form the Euler equations read

$$\frac{\partial \boldsymbol{U}}{\partial t} + \frac{\partial \boldsymbol{F}(\boldsymbol{U})}{\partial x} + \frac{\partial \boldsymbol{G}(\boldsymbol{U})}{\partial y} + \frac{\partial \boldsymbol{H}(\boldsymbol{U})}{\partial z} = \boldsymbol{0}, \tag{5.1}$$

where

$$\boldsymbol{U} = \begin{pmatrix} \rho \\ \rho v_x \\ \rho v_y \\ \rho v_z \\ E \end{pmatrix} \tag{5.2}$$

is the vector of conserved variables, and the flux vectors are given by

$$\boldsymbol{F} = \begin{bmatrix} \rho v_x \\ \rho v_x^2 + p \\ \rho v_x v_y \\ \rho v_x v_z \\ v_x(E+p) \end{bmatrix}, \boldsymbol{G} = \begin{bmatrix} \rho v_y \\ \rho v_x v_y \\ \rho v_y^2 + p \\ \rho v_y v_z \\ v_y(E+p) \end{bmatrix}, \text{ and } \boldsymbol{H} = \begin{bmatrix} \rho v_z \\ \rho v_x v_z \\ \rho v_y v_z \\ \rho v_z^2 + p \\ v_z(E+p) \end{bmatrix} \tag{5.3}$$

(see e. g. Toro 2009). ρ denotes the mass density, E the total energy density, p the pressure, and v_x, v_y, and v_z the components of the velocity $\boldsymbol{v}$ in x, y, and z direction, respectively. It is assumed that the equation of state for an ideal gas

$$e = \frac{p}{(\gamma - 1)\rho} \tag{5.4}$$

gives the relation between the pressure and the specific internal energy

$$e = \frac{E - \frac{1}{2}\rho \boldsymbol{v}^2}{\rho}, \tag{5.5}$$

where γ is the ratio of the specific heat at constant volume c_V and the specific heat at constant pressure c_p, i. e. $\gamma = c_p/c_V$. Then the expression for the temperature T reads

$$T = \frac{p}{R\rho}, \tag{5.6}$$

where $R = k_\mathrm{B}/m$ is the specific gas constant, which is inversely proportional to the mean particle mass m, with the Boltzmann constant k_B.

5.1.2 Numerical scheme

The numerical scheme used by AMRCART to integrate the Euler equations (Eq. 5.1) has been developed by Barmin et al. (1996). Their method is based on the Lax-Friedrichs scheme originally described by Lax (1954), which is first-order accurate in space and time. They used a predictor-corrector procedure to obtain a scheme with a second-order accuracy. The finite-volume scheme used in AMRCART to solve the Euler equations reads

$$\begin{aligned} \boldsymbol{U}_{i,j,k}^{n+1} = \boldsymbol{U}_{i,j,k}^{n} + \frac{\Delta t}{\Delta x}\left(\boldsymbol{F}_{i-1/2,j,k}^{n+1/2} - \boldsymbol{F}_{i+1/2,j,k}^{n+1/2}\right) + \frac{\Delta t}{\Delta y}\left(\boldsymbol{G}_{i,j-1/2,k}^{n+1/2} - \boldsymbol{G}_{i,j+1/2,k}^{n+1/2}\right) \\ + \frac{\Delta t}{\Delta z}\left(\boldsymbol{H}_{i,j,k-1/2}^{n+1/2} - \boldsymbol{H}_{i,j,k+1/2}^{n+1/2}\right), \end{aligned} \tag{5.7}$$

where the indices i, j, and k refer to the positions $x = i\Delta x$, $y = j\Delta y$, and $z = k\Delta z$ in x, y, and z direction, respectively, and n denotes the time $t = n\Delta t$. The calculation of the fluxes $\boldsymbol{F}$, $\boldsymbol{G}$, and $\boldsymbol{H}$ is described in the following. They are given at the boundaries between two grid cells at the intermediate time $t = (n + 1/2)\Delta t$.

The calculation of the fluxes by means of a predictor-corrector scheme is the same for each direction. Therefore, the following outline of the procedure for the flux $\boldsymbol{F}$ in the x direction is the same for the fluxes $\boldsymbol{G}$ and $\boldsymbol{H}$ in the y and z direction. The predictor step advances the solution by half a time-step, $\Delta t/2$, using the FTCS (forward- time, centered-space) scheme, which is unstable when used as a stand-alone method (cf. Fletcher 1991, Sect. 9.1.1),

$$\boldsymbol{U}_i^{n+1/2} = \boldsymbol{U}_i^n + \frac{\Delta t}{4\Delta x}\left(\boldsymbol{F}_{i-1}^n - \boldsymbol{F}_{i+1}^n\right), \tag{5.8}$$

where Δx is the width of a grid cell, i specifies the position in space $x = i\Delta x$, and n the current time $t = n\Delta t$.

The following corrector step is the modified Lax-Friedrichs scheme

$$\boldsymbol{U}_i^{n+1} = \boldsymbol{U}_i^n + \frac{\Delta t}{\Delta x}\left(\boldsymbol{F}_{i-1/2}^{n+1/2} - \boldsymbol{F}_{i+1/2}^{n+1/2}\right) \tag{5.9}$$

(cf. Eq. 5.7), where the fluxes $\boldsymbol{F}$ differ from the original scheme in that the factor $\Delta x/\Delta t$ is replaced by the spectral radius r of the Jacobian matrix $\partial\boldsymbol{F}/\partial\boldsymbol{U}$, i. e.

$$\boldsymbol{F}_{i+1/2}^{n+1/2} = \frac{1}{2}\left[\boldsymbol{F}\left(\boldsymbol{U}_{i+1/2,\mathrm{L}}^{n+1/2}\right) + \boldsymbol{F}\left(\boldsymbol{U}_{i+1/2,\mathrm{R}}^{n+1/2}\right) + r\left(\boldsymbol{U}_{i+1/2,\mathrm{L}}^{n+1/2} - \boldsymbol{U}_{i+1/2,\mathrm{R}}^{n+1/2}\right)\right]. \tag{5.10}$$

The value of the spectral radius is $r = |\overline{v}_x| + \overline{a}$ with the mean value of the velocity in x direction $\overline{v}_x$ and the speed of sound $\overline{a}$,

$$|\overline{v}_x| = \frac{1}{2}\left(\left|v_{x,\,i+1/2,\mathrm{L}}^{n+1/2}\right| + \left|v_{x,\,i+1/2,\mathrm{R}}^{n+1/2}\right|\right), \tag{5.11}$$

$$\overline{a} = \frac{1}{2}\left(a_{i+1/2,\mathrm{L}}^{n+1/2} + a_{i+1/2,\mathrm{R}}^{n+1/2}\right), \tag{5.12}$$

where the speed of sound $a = \sqrt{\gamma p/\rho}$ is calculated using the values of the density and the pressure at the given grid points.

For the calculation of the values at the boundaries between two grid cells, $\boldsymbol{U}_{i+1/2,\mathrm{L}}^{n+1/2}$ on the left side and $\boldsymbol{U}_{i+1/2,\mathrm{R}}^{n+1/2}$ on the right side of the boundary, a linear distribution of the data is assumed inside each grid cell. The slopes of these linear functions are determined with the minmod function

$$\mathrm{minmod}\,(x,\,y) = \mathrm{sgn}(x)\max\left\{0,\,\min\left[|x|\,,\,y\,\mathrm{sgn}(x)\right]\right\}. \tag{5.13}$$

For this procedure, the conservative variables $\boldsymbol{U}$ are transformed to the primitive variables $\boldsymbol{V}$,

$$\boldsymbol{V} = \begin{pmatrix}\rho\\ v_x\\ v_y\\ v_z\\ p\end{pmatrix} = \begin{pmatrix}1 & 0 & 0 & 0 & 0\\ 0 & \rho^{-1} & 0 & 0 & 0\\ 0 & 0 & \rho^{-1} & 0 & 0\\ 0 & 0 & 0 & \rho^{-1} & 0\\ 0 & \frac{1}{2}(1-\gamma)v_x & \frac{1}{2}(1-\gamma)v_y & \frac{1}{2}(1-\gamma)v_z & \gamma-1\end{pmatrix}\boldsymbol{U}, \tag{5.14}$$

cf. Eqs. 5.2, 5.4, and 5.5.

The values at the cell boundaries for each component V of $\boldsymbol{V}$ are computed according to

$$V_{i+1/2,\,\mathrm{R}}^{n+1/2} = V_{i+1}^{n+1/2} - \frac{1}{4}\left[(1-\eta)\,\mathrm{minmod}\left(\Delta_{i+3/2},\,\omega\Delta_{i+1/2}\right) + (1+\eta)\,\mathrm{minmod}\left(\Delta_{i+1/2},\,\omega\Delta_{i+3/2}\right)\right], \tag{5.15}$$

$$V_{i+1/2,\,\mathrm{L}}^{n+1/2} = V_{i}^{n+1/2} + \frac{1}{4}\left[(1-\eta)\,\mathrm{minmod}\left(\Delta_{i-1/2},\,\omega\Delta_{i+1/2}\right) + (1+\eta)\,\mathrm{minmod}\left(\Delta_{i+1/2},\,\omega\Delta_{i-1/2}\right)\right], \tag{5.16}$$

where η and ω are dimensionless parameters, and the minmod slopes result from the differences in V between adjacent grid cells, namely

$$\begin{aligned} \Delta_{i-1/2} &= V_{i}^{n+1/2} - V_{i-1}^{n+1/2}, \\ \Delta_{i+1/2} &= V_{i+1}^{n+1/2} - V_{i}^{n+1/2}, \text{ and} \\ \Delta_{i+3/2} &= V_{i+2}^{n+1/2} - V_{i+1}^{n+1/2}. \end{aligned} \tag{5.17}$$

Then a transformation back to conservative variables is performed and the results are inserted in Eq. 5.10.

Barmin et al. (1996) calculated a set of 1D Riemann problems with different values for ω and η. They obtained the best results with $\eta = 1/3$ and $\omega = 2$, with the exception of the pressure p, for which $\omega = 1$ was used. These values were adopted for most of the simulations presented in this work.

5.1.3 The adaptive mesh

The computing time required by AMRCART is mainly determined by the number of grid cells that have to be advanced in time. One possibility of limiting the computing time is to use high resolution only in the regions where it is required and to use a lower resolution in the rest of the domain. This can be achieved by using adaptive mesh refinement (AMR).

The algorithm used by AMRCART for the adaptive mesh refinement was described by Berger & Colella (1989). The idea is to estimate the local truncation error TE of the density ρ periodically during the simulation and to refine those parts of the grid that contain cells whose error is larger than a given tolerance limit.

The method for calculating the truncation error is based on Richardson extrapolation (see also Berger & Oliger 1984). The local truncation error is the difference between the exact solution $\overline{\rho}$, which is unknown, and the approximate solution ρ resulting from the numerical scheme,

$$TE = \overline{\rho}_i^{n+1} - \rho_i^{n+1} \equiv \overline{\rho}(\boldsymbol{r}, t+\Delta t) - Q\rho(\boldsymbol{r}, t), \tag{5.18}$$

where Q denotes the application of the numerical scheme given in Eq. 5.7 and $\boldsymbol{r}$ is the position (x, y, z).

An estimate of TE can be calculated by comparing the truncation errors resulting from two integrations with different increments in space[1] (Δx) and time (Δt). The truncation error resulting from two integration steps (see Eq. 5.7) with the current values of Δx and Δt is given by

$$\overline{\rho}(\boldsymbol{r}, t + 2\Delta t) - Q^2\rho(\boldsymbol{r}, t) = 2TE(\boldsymbol{r}, t) + O\left[(\Delta x)^{q+2}, (\Delta t)^{q+2}\right], \tag{5.19}$$

where

$$TE(\boldsymbol{r}, t) = O\left[(\Delta x)^{q+1}, (\Delta t)^{q+1}\right] \tag{5.20}$$

is the truncation error resulting from one single integration step (see Eq. 5.18) and q is the order of accuracy of the numerical scheme. The truncation error resulting from an integration with increments increased by a factor of two reads

$$\overline{\rho}(\boldsymbol{r}, t + 2\Delta t) - Q_2\rho(\boldsymbol{r}, t) = 2^{q+1}TE(\boldsymbol{r}, t) + O\left[(\Delta x)^{q+2}, (\Delta t)^{q+2}\right], \tag{5.21}$$

where Q_2 denotes the application of the numerical scheme with the doubled increment. Thus, an estimate of the truncation error $TE(\boldsymbol{r}, t)$ can be obtained by subtracting Eq. 5.19 from Eq. 5.21, which yields

$$TE(\boldsymbol{r}, t) + O\left[(\Delta x)^{q+2}, (\Delta t)^{q+2}\right] = \frac{Q^2\rho(\boldsymbol{r}, t) - Q_2\rho(\boldsymbol{r}, t)}{2^{q+1} - 2} \tag{5.22}$$

(Berger & Colella 1989).

When $TE(\boldsymbol{r}, t)$ exceeds a given tolerance limit ε, the grid cell is flagged and a higher resolution will be used in the following integration steps. In a subsequent step cuboid-shaped subgrids are generated that include all flagged cells. When the coarse grid has a resolution Δx and Δt in space and time, respectively, these subgrids have a resolution of $\Delta x/R$ and $\Delta t/R$ defined by a refinement ratio R, an integer, which can be adjusted as required. The positions and sizes of the subgrids depend on the number of flagged cells, which is determined by the tolerance limit ε, and on the minimum percentage f of flagged cells in each subgrid, which is also predefined by the user. Figure 5.1 shows an example of the distribution of fine grids in a simulation of the α Sco system. Obviously, the higher resolution is used only in the vicinity of inhomogeneities in the density structure.

For the simulation presented in Fig. 5.1 two levels of refinement were used, i. e. one level of refined subgrids in addition to the base level that comprises the whole computational domain. The refinement ratio was $R = 2$ in this simulation, and I used $\varepsilon = 4 \times 10^{-4}$ and $f = 0.7$ for the tolerance limit and the minimum percentage of flagged cells in the subgrids. As the subgrids are cuboid-shaped, they must be allowed to contain cells that are not flagged to limit the total number of subgrids to be generated. If the number of subgrids is too large, the time needed to generate and integrate the subgrids compensates the saving of time that is due to the reduced number of fine grid cells (cf. next section).

[1] In the simulations presented in this work the spatial resolution is equal in all directions, i. e. $\Delta x = \Delta y = \Delta z$.

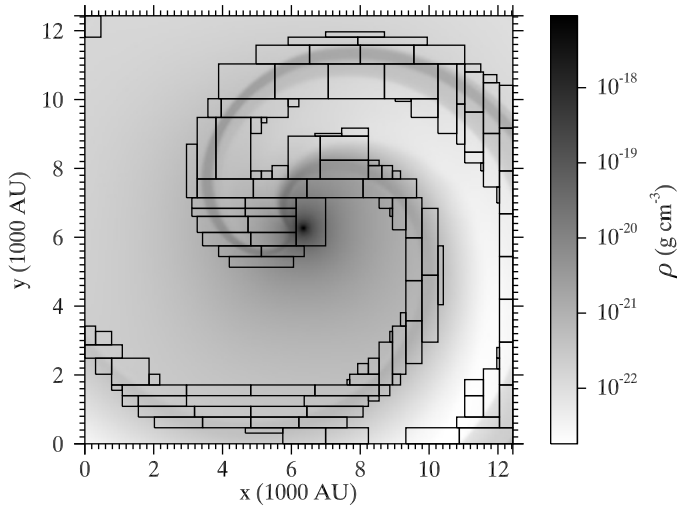

Figure 5.1: Density structure after about one orbit in a simulation using $\dot{M} = 7.5 \times 10^{-7}\ M_\odot\,\mathrm{yr}^{-1}$ and $v_\infty = 15\ \mathrm{km\,s}^{-1}$. The rectangles indicate the positions of fine grids in the plane of the orbit.

For the example shown in Fig. 5.1 and the other simulations presented in this work, the error tolerance ε was not applied to the absolute truncation error $TE(\boldsymbol{r}, t)$ but to its relative value, i. e.

$$\frac{TE(\boldsymbol{r}, t)}{Q^2 \rho(\boldsymbol{r}, t)} \leq \varepsilon, \tag{5.23}$$

where $TE(\boldsymbol{r}, t)$ is the estimated value of the truncation error as given by Eq. 5.22.

5.1.4 Stability and computing time of the simulations

The stability of a numerical simulation is influenced by the grid spacing in time, Δt, and space, Δx. In AMRCART, stability is achieved by choosing an appropriate Courant-Friedrichs-Lewy (CFL) condition. This condition constrains the time increment via the relation

$$\frac{v \Delta t}{\Delta x} \leq CFL, \tag{5.24}$$

where v is the maximum velocity at the current time and CFL the so-called CFL number. As the velocity changes with time, the time increment may have to be changed many times during the simulation. For the simulations presented in this work I used $CFL = 0.15$. With higher CFL numbers the code tends to become unstable.

As the total computing time scales with the number of integration steps the time increment, and thus the CFL number, determines the computing time. It also scales with the total number of grid cells, which can be reduced using AMR as described in the previous section. Table 5.1 lists typical CPU and wall-clock times (t_{CPU} and t_{wc}) for simulations of the α Sco system, as presented in this work, with different numbers of refinement levels. All these simulations were performed

Table 5.1: Total CPU and wall-clock times required by AMRCART/Cloudy simulations for different numbers of refinement levels.

$\Delta x\ \left(10^{-2}\right)$	N_{level}	$\varepsilon\ (10^{-4})$	t_{CPU} (h:min)	t_{wc} (h:min)
1.25	3	4	319:17	47:31
0.625	2	4	258:55	41:14
0.3125	1		308:27	43:05

Notes. Δx is the spatial increment in the coarsest grid, N_{level} the number of levels of refinement, and ε the error tolerance (see Sect. 5.1.3).

with $f = 0.7$ and $R = 2$, and the edge lengths of the computational domain are $a_x \times a_y \times a_z \sim 12\,433 \times 12\,433 \times 3419$ AU, with the center of mass at (6216.5, 6216.5, 3108.25) AU. As the system is symmetric with respect to the orbital plane, the upper half, i. e. the part above the plane of the orbit, is just the mirror image of the lower half and the center of mass is placed near the upper boundary of the computational domain to save computing time. The spatial increments in y and z direction are equal to Δx, which is chosen such that the resolution on the finest grids is equal for all simulations. All the simulations correspond to different values of $\dot{M}$ and v_∞.

The hydrodynamic part of the simulations takes about 13 % of the total CPU times presented in Table 5.1, which apply to simulations including 45 Cloudy models corresponding to 45 directions[2] covering the computational domain, which are executed at intervals of four time steps as counted on the finest grid. However, it takes up to 90 % of the wall-clock time, because it is serial, whereas the Cloudy runs are executed on different processors, so that the Cloudy part of the wall-clock time optimally equals the time $t_{\mathrm{opt}} \sim 0.02 t_{\mathrm{CPU}}$ needed if the number of processors $N_{\mathrm{proc}} = 45$. Thus, the wall-clock time t_{wc} can roughly be estimated as a function of N_{proc} and t_{CPU},

$$t_{\mathrm{wc}} = \left(\frac{0.85}{N_{\mathrm{proc}}} + 0.13\right) t_{\mathrm{CPU}},\ N_{\mathrm{proc}} \leq N_{\mathrm{Cl}}, \tag{5.25}$$

where N_{Cl} is the number of Cloudy simulations executed at regular intervals and t_{CPU} is the total CPU time required by the simulation.

With $N_{\mathrm{level}} = 2$ the wall-clock time can be reduced by ~ 5 %. With $N_{\mathrm{level}} = 3$, the time consumed by generating new subgrids compensates the saving of time by the reduction of the number of grid cells. I adapted AMRCART in a way that it can execute Cloudy as required and assign the different models to different processors. On shared-memory clusters, this parallelization is implemented by use of OpenMP, while on distributed-memory clusters MPI commands are used. For the simulations presented in Table 5.1, an SGI UV parallel cluster was used, which is composed of Intel Xeon Beckton (X7560, 2.23 GHz) CPUs, with eight cores per CPU and a shared memory architecture. The operating system installed

[2] $N = 9$, cf. Eqs. A.3 and A.2

on the cluster was SLES 11, and the programs were compiled using version 12.0 of the Intel compilers.

5.1.5 Initial and boundary conditions

Assuming that the wind has reached its terminal velocity v_∞, the initial mass-density distribution falls off with increasing distance from the primary star according to the formula

$$\rho = \frac{\dot{M}}{4\pi r^2 v_\infty}, \tag{5.26}$$

where r is the radial distance to the primary. Thus, the initial flow field consists of a radially symmetric component with a velocity of v_∞ and the velocity of the primary star $\boldsymbol{v}_\mathrm{A}$, which is added at each point to the wind velocity, giving the total velocity

$$\boldsymbol{v} = \frac{v_\infty}{r} \begin{pmatrix} x - x_\mathrm{A} \\ y - y_\mathrm{A} \\ z - z_\mathrm{A} \end{pmatrix} + \boldsymbol{v}_\mathrm{A}, \tag{5.27}$$

where $(x_\mathrm{A}, y_\mathrm{A}, z_\mathrm{A})$ are the coordinates of the primary star. The initial temperature is set to 300 K, which is consistent with the estimate of Kudritzki & Reimers (1978). With lower values of this temperature the simulations become unstable.

At the outer boundaries of the computational domain "free flow" is assumed, i. e., density and velocity in boundary grid cells equal the values of the cells at the edge of the domain. The surface of the secondary star is not included as a boundary, and the surface cells of the primary star are handled according to Eqs. 5.26 and 5.27.

5.2 Plasma simulations of the H II region

In the α Sco system the secondary star ionizes a large fraction of the circumstellar envelope. This produces a hot ionized region moving with the secondary star through the material that is ejected by the primary. The thermal front at the edge of the ionized region is expected to produce hydrodynamic effects resulting from the interaction with cool neutral wind material.

Ionization, heating, and cooling mechanisms can be simulated using the Cloudy code (see Sect. 5.2.1). I used version 08.00 of Cloudy to produce a realistic temperature distribution for the binary system. Then I used this temperature distribution to update the energy terms in the AMRCART code. This procedure is executed at regular intervals during the hydro simulation. The basis for the Cloudy calculations is the current density distribution extracted from AMRCART.

5.2.1 The Cloudy program

The program Cloudy is "a large-scale spectral synthesis code designed to simulate fully physical conditions within an astronomical plasma and then predict

the emitted spectrum" (Ferland et al. 1998). It calculates the thermal and ionization balance with a simultaneous treatment of radiative transfer. The considered ionization processes include photo, Auger, and collisional ionization and charge transfer. The recombination processes include radiative, low-temperature dielectronic, high-temperature dielectronic, three-body recombination, and charge transfer (Ferland et al. 1998).

The prediction of line intensities includes collisional as well as pumping effects and is based on solving the equations of statistical equilibrium. Cloudy includes atoms and ions of the lightest 30 elements and mostly treats them as multi-level atoms. The radiative transfer is calculated using an escape probability formalism (EPF).

The EPF considerably simplifies the radiative transfer problem. Taking as an example the calculation of the diffuse radiation for two-level atoms, the EPF makes the assumption

$$n_\mathrm{u} A_\mathrm{ul} + n_\mathrm{u} B_\mathrm{ul} \bar{J} - n_\mathrm{l} B_\mathrm{lu} \bar{J} \equiv n_\mathrm{u} A_\mathrm{ul} \left(1 - \frac{\bar{J}}{S}\right) = n_\mathrm{u} A_\mathrm{ul} P_\mathrm{esc} \tag{5.28}$$

(see e. g. Rybicki 1984, p. 46), where n_l and n_u are the number densities of atoms in the lower and upper state, $\bar{J}$ is the mean intensity at the frequency of the transition, and A_ul, B_ul, and B_lu are the Einstein coefficients for spontaneous and induced emission, and absorption, respectively. S denotes the source function and P_esc the angle-averaged escape probability, averaged over the line profile $\phi(\nu)$, i. e.

$$P_\mathrm{esc} = \frac{1}{4\pi} \int \mathrm{d}\Omega \int_0^\infty \mathrm{d}\nu \phi(\nu) p_\nu \tag{5.29}$$

with the escape probability

$$p_\nu = \mathrm{e}^{-\tau_\nu}, \tag{5.30}$$

where τ_ν is the monochromatic optical depth, measured from the considered point to the boundary of the region (Rybicki 1984, pp. 31 f.).

This implies the on-the-spot approximation, which states that all photons created at a given point in the region are either absorbed at the same point, "on the spot", or escape without further interactions. If these on-the-spot conditions are satisfied, the EPF described above is exact (Rybicki 1984, p. 46).

5.2.2 The spectrum of the B star

The spectrum of the B star is an important boundary conditions for the simulations. Its shape affects the temperature of the irradiated gas, and the total Lyman-continuum flux determines the size of the resulting H II region. Hjellming & Newell (1983) derived a Lyman-continuum luminosity of $L_\mathrm{Ly} = 3.1 \times 10^{43}\ \mathrm{s}^{-1}$ for the spectrum of the B star by means of radio observations of the Antares nebula. This result served as a constraint on the model spectrum used in the Cloudy simulations. I used the TLUSTY grid of theoretical B-star spectra calculated by

Table 5.2: $L_{\rm Ly}$ as a function of $T_{\rm eff}$ for $\log g = 3.9$ and $R = 4.8\,R_\odot$, derived from models presented by Lanz & Hubeny (2007).

$T_{\rm eff}$ (K)	$L_{\rm Ly}$ (10^{43} s^{-1})
18 000	2.65
18 100	2.86
18 200	3.07
18 300	3.33
18 400	3.59
18 500	3.87

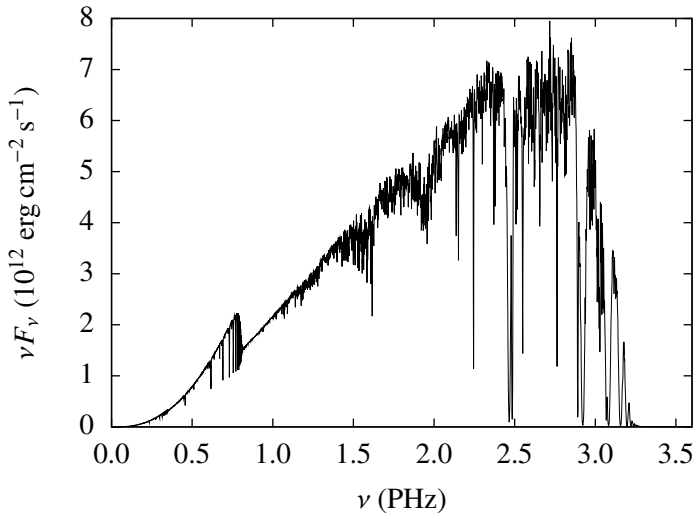

Figure 5.2: TLUSTY spectrum corresponding to $T_{\rm eff} = 18\,200$ K, $\log g = 3.9$, and the adopted radius $R_{\rm B} = 4.8\,R_\odot$ (Lanz & Hubeny 2007).

Lanz & Hubeny (2007) to interpolate spectra corresponding to different values of $T_{\rm eff}$ and $\log g$.

The definition of the Lyman continuum luminosity reads

$$L_{\rm Ly} = 4\pi R_{\rm B}^2 \int_{\nu_0}^{\infty} \frac{F_\nu}{h\nu}\,{\rm d}\nu, \tag{5.31}$$

where $\nu_0 \sim 3.3$ PHz denotes the threshold frequency for the ionization of hydrogen, F_ν is the flux at the surface of the star (erg cm^{-2} s^{-1} Hz^{-1}), and h is Planck's constant. The model spectrum corresponding to the values derived by Kudritzki & Reimers (1978) with a radius $R_{\rm B} = 4.8\,R_\odot$ (see Sect. 3) yields $L_{\rm Ly} = 3.9\times10^{43}$ s^{-1}. Table 5.2 lists $L_{\rm Ly}$ for different values of $T_{\rm eff}$, a fixed surface gravity $\log g = 3.9$ and a radius $R_{\rm B} = 4.8\,R_\odot$. For the Cloudy simulations I used the model atmosphere corresponding to $T_{\rm eff} = 18\,200$ K, whose spectrum is shown in Fig. 5.2. The Lyman-continuum luminosity of this spectrum lies closest to the value derived by Hjellming & Newell (1983).

5.2.3 Calculating the temperature distribution

Cloudy uses a spherical geometry in one dimension (1D). In order to obtain a three-dimensional (3D) temperature distribution of the α Sco system I calculated different Cloudy models, each one corresponding to a different direction (θ, ϕ), starting from the position of the source of ionizing radiation, i. e. the secondary star. See Sect. A.1 for details.

Density interpolation and coordinate transformation

The density disribution along the different directions of the 1D Cloudy-models is taken from intermediate results given by AMRCART. AMRCART uses normalized cartesian coordinates, i. e. all distances are divided by the length a of the longest edge of the rectangular computational domain, and the origin is located at one of the lower edges of the domain.

Cloudy reads the density as a function of radial distance r from the secondary star so that a coordinate transformation has to be performed. When a Cloudy simulation corresponding to the direction (θ, ϕ) requests the density at a position r, first the coordinates (r, θ, ϕ) are transformed to normalized cartesian coordinates $\boldsymbol{r}_{\mathrm{Cl}} \equiv (x_{\mathrm{Cl}}, y_{\mathrm{Cl}}, z_{\mathrm{Cl}})$ via

$$\boldsymbol{r}_{\mathrm{Cl}} = \frac{r}{a} \begin{pmatrix} \sin\theta\cos\phi \\ \sin\theta\sin\phi \\ \cos\theta \end{pmatrix}. \tag{5.32}$$

θ denotes the angle measured from the upper pole (positive z_{Cl} direction) downward in the range $[0, \pi]$, while ϕ gives the angle between the positive x_{Cl} direction and the projection of $\boldsymbol{r}_{\mathrm{Cl}}$ on the xy plane in the range $[0, 2\pi)$. The spherical coordinates are defined such that the x_{Cl} axis points to the primary star and ϕ is measured counterclockwise from the positive x_{Cl} direction to the positive y_{Cl} direction etc.

Now the cartesian coordinates $\boldsymbol{r}_{\mathrm{AC}} = (x_{\mathrm{AC}}, y_{\mathrm{AC}}, z_{\mathrm{AC}})$ used by AMRCART are given by

$$\boldsymbol{r}_{\mathrm{AC}} = \boldsymbol{r}_{\mathrm{B}} + \begin{pmatrix} \cos\alpha & -\sin\alpha & 0 \\ \sin\alpha & \cos\alpha & 0 \\ 0 & 0 & 1 \end{pmatrix} \boldsymbol{r}_{\mathrm{Cl}}, \tag{5.33}$$

where $\boldsymbol{r}_{\mathrm{B}}$ is the position of the secondary star in the AMRCART coordinate system and α is the orbital rotation angle measured in the plane of the orbit starting from the position $(x_{\mathrm{B}}, 0.5, 0.5)$ in the direction of the orbital motion (see Fig. 5.3), i. e.

$$\alpha = \mathrm{atan2}(0.5 - y_{\mathrm{B}}, 0.5 - x_{\mathrm{B}}), \tag{5.34}$$

where the function atan2 is defined as described in Sect. A.2. Thus, Eqs. 5.32 and 5.33 provide an interface between Cloudy and the cartesian grid used by AMRCART. The requested density information is obtained by linear interpolation using the grid cells nearest to $\boldsymbol{r}_{\mathrm{AC}}$ (see Sect. A.3.1).

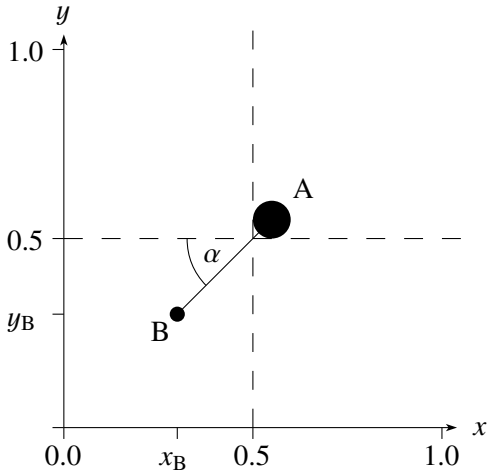

Figure 5.3: Geometry of the binary system in AMRCART in the *xy* plane parallel to the orbit. A is the primary supergiant, B the secondary star.

Temperature interpolation and coordinate transformation

As Cloudy uses an adaptive mesh in r, the temperature information resulting from the Cloudy runs corresponding to different directions (θ, ϕ) is distributed irregularly in 3D space on a grid in spherical coordinates. When AMRCART requests the temperature at a grid point $\boldsymbol{r}_{\mathrm{AC}}$ given in cartesian coordinates, the backward transformation

$$\boldsymbol{r}_{\mathrm{Cl}} = \begin{pmatrix} \cos\alpha & \sin\alpha & 0 \\ -\sin\alpha & \cos\alpha & 0 \\ 0 & 0 & 1 \end{pmatrix} (\boldsymbol{r}_{\mathrm{AC}} - \boldsymbol{r}_{\mathrm{B}}) \tag{5.35}$$

(cf. Eq. 5.33) is applied. Then the expressions of r, θ and ϕ as functions of $\boldsymbol{r}_{\mathrm{Cl}}$ read

$$r = \sqrt{x_{\mathrm{Cl}}^2 + y_{\mathrm{Cl}}^2 + z_{\mathrm{Cl}}^2} \tag{5.36}$$

$$\theta = \mathrm{atan2}\left(\sqrt{x_{\mathrm{Cl}}^2 + y_{\mathrm{Cl}}^2}, z_{\mathrm{Cl}}\right), \text{and} \tag{5.37}$$

$$\phi = \begin{cases} \mathrm{atan2}(y_{\mathrm{Cl}}, x_{\mathrm{Cl}}), & y > 0 \\ \mathrm{atan2}(y_{\mathrm{Cl}}, x_{\mathrm{Cl}}) + 2\pi, & y < 0 \end{cases}. \tag{5.38}$$

Now the corresponding temperature is determined by interpolation involving the nearest grid points.

At the end of the Cloudy simulations a routine is accessed that transfers the temperature distribution to a uniform cartesian grid in the AMRCART coordinate system. The position of every grid point (i, j, k) (cf. Eq. A.6) is transformed to the Cloudy coordinate system via Eqs. 5.35 to 5.38. For the resulting points (r, θ, ϕ) the nearest Cloudy models are determined, i. e. values $(\theta_i, \phi_{\theta,i})$ that satisfy $\theta_1 \leq \theta \leq \theta_2$, $\phi_{\theta_1,1} \leq \phi \leq \phi_{\theta_1,2}$ and $\phi_{\theta_2,1} \leq \phi \leq \phi_{\theta_2,2}$. This results in up to four ϕ values

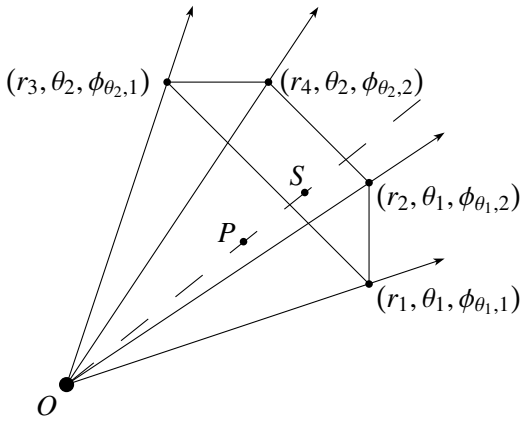

Figure 5.4: Examination of the position of the grid point $P \equiv (r, \theta, \phi)$ relative to the H II region. S marks the position of the H II-region boundary in the direction (θ, ϕ).

and two θ values that correspond to different Cloudy models, and the temperature at the grid point is calculated by interpolation between these models.

First, a cubic spline interpolation in the r coordinate is performed along each of the 1D Cloudy-models using the algorithm provided by Press et al. (1992, § 3.3) as a C program. Then the interpolated value of the temperature at the requested grid point is obtained by linear interpolation in θ and ϕ. The thermal front at the edge of the ionized region around the secondary star represents a large temperature gradient that can lead to inconsistent results when interpolating linearly in θ or ϕ between the hot H II region and the cool neutral region. Therefore, it is checked first whether the grid point is inside the H II region and then either only the points that also lie inside the H II region are used for the interpolation or the temperature is given the value[3] $T_{\rm out} = 300$ K, respectively.

Figure 5.4 illustrates the procedure of determining whether a point $P = (r,\ \theta,\ \phi)$ is outside or inside the H II region in the case that the grid points of four Cloudy models are involved. The four points defining the quadrangle mark the positions of the H II-region boundary in the different directions whose distances to the origin O, which is the position of the secondary star, are given by r_i, where $i = 1, \ldots, 4$. The ionization fraction of hydrogen, i. e. the ratio of the densities of ionized and neutral hydrogen, determines the position of this boundary by defining r_i as the radial distance from B at which $n_{\rm H\,II}/n_{\rm H\,I} \sim 0.9$. Clearly, P lies inside the H II region if $r < r_S$ or

$$\frac{r_S}{r} > 1, \tag{5.39}$$

where r_S marks the position of the boundary in the direction (θ, ϕ).

The quadrangle defines the approximate position of the boundary of the H II

[3] As the mean particle mass depends on the degree of ionization, this temperature actually corresponds to different energies (see Eqs. 5.4 and 5.6). In the hydro simulations a constant mean particle mass of $m = 0.61$ u is used.

region in 3D space and includes the point $S \equiv (r_S, \theta, \phi)$. In cartesian coordinates the positions of P, S and the corners are given by $\boldsymbol{r}, \boldsymbol{r}_S$ and $\boldsymbol{r}_i, i = 1, \ldots, 4$, respectively (see Eqs. A.9 to A.11 in Sect. A.3.2). Because the orientations of $\boldsymbol{r}_S$ and $\boldsymbol{r}$ are identical, r_S can be expressed as $\boldsymbol{r}_S = r_S \boldsymbol{r}/r$. Moreover, $\boldsymbol{r}_S$ is lying in the plane described by the quadrangle so that

$$\boldsymbol{r}_S = \frac{r_S}{r}\boldsymbol{r} = \boldsymbol{r}_1 + a\boldsymbol{d}_1 + b\boldsymbol{d}_2, \tag{5.40}$$

where a and b are unknown constants, $\boldsymbol{d}_1 = \boldsymbol{r}_2 - \boldsymbol{r}_1$, and $\boldsymbol{d}_2 = \boldsymbol{r}_3 - \boldsymbol{r}_1$ or $\boldsymbol{d}_2 = \boldsymbol{r}_4 - \boldsymbol{r}_1$ (cf. Eq. A.12). Rearranging Eq. 5.40 gives the linear system of equations

$$\mathsf{A}\boldsymbol{u} = -\boldsymbol{r}_1, \tag{5.41}$$

where the columns of the (3×3) matrix A constitute the vectors appearing in Eq. 5.40, i. e. $\mathsf{A} = (\boldsymbol{d}_1, \boldsymbol{d}_2, -\boldsymbol{r})$, and $\boldsymbol{u} = (a, b, r_S/r)^{\mathrm{t}}$. The solution of this system using the standard LU decomposition algorithm with subsequent forward substitution and backsubstitution provided by Press et al. (1992, § 2.3) as a C program gives the value of r_S/r that determines whether the point P lies inside the H II region or not (see Eq. 5.39).

See Sect. A.3 for further details about the exchange of data between AMRCART and Cloudy.

Chapter 6

Effects of the H II region

The temperature distribution obtained with the plasma simulations is fed into the hydrodynamic simulations in the form of a boundary condition. In order to get an idea of the basic effects that are to be expected of a hot region inside the cool wind of the supergiant I first studied a simplified 1D-problem. This so-called Riemann problem can be solved analytically. In the subsequent sections I present results of the detailed 3D-simulations.

6.1 Considering a simplified 1D-model

In one dimension, the application of the Euler equations to the initial-value problem of two constant states at different pressures that are separated by a discontinuity, see Fig. 6.1, constitutes a Riemann problem. Typical values of the physical quantities characterizing the conditions in the circumstellar envelope in the vicinity of the boundary between the H II and the H I region are summarized in Table 6.1. The quantities of the right state in the Riemann problem, labeled with subscript R, correspond to the physical conditions inside the H II region, while the quantities of the left state, labeled with subscript L, correspond to the neutral wind (H I region).

Table 6.1: Initial values for the Riemann problem at the boundary of the H II region.

Left state		Right state	
Quantity	Value	Quantity	Value
T_L	300 K	T_R	5000 K
ρ_L	5.18×10^{-14} g cm^{-3}	ρ_R	5.18×10^{-14} g cm^{-3}
m_L	1.67×10^{-24} g	m_R	8.37×10^{-25} g
p_L	1.28×10^{-9} dyn cm^{-2}	p_R	4.27×10^{-8} dyn cm^{-2}

Notes. m_L and m_R are the mean particle-masses in the left and right state, respectively.

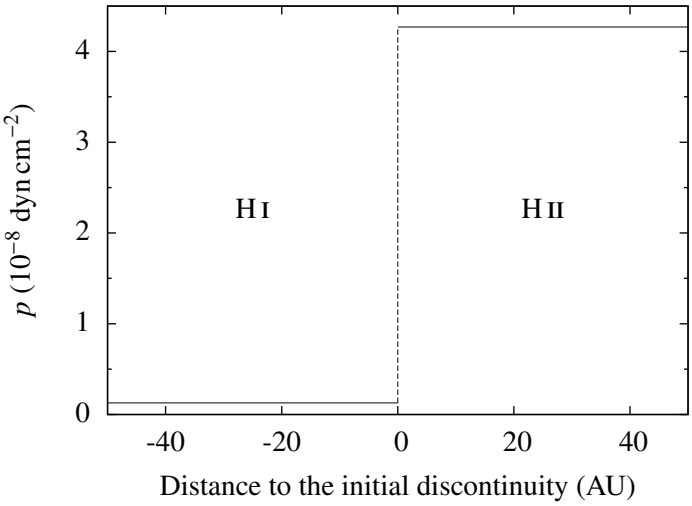

Figure 6.1: Left and right state of the Riemann problem corresponding to the situation at the boundary of the H II region of α Sco.

The pressure is related to the temperature via

$$p = \frac{k_\mathrm{B}}{m}\rho T, \tag{6.1}$$

where k_B is Boltzmann's constant, m is the mean particle-mass, ρ is the mass density and T the temperature. The value of the mass density is assumed to be $\rho(r_\mathrm{B})$ in both initial states and results from Eq. 5.26 using the radial distance of the B star

$$r_\mathrm{B} = \frac{\sin(2\farcs73)}{\cos\delta}d \tag{6.2}$$

(cf. Table 3.1). The values of m_L and m_R result from the assumption that the left state contains pure atomic hydrogen, and the right state pure ionized hydrogen, respectively. By the use of the rest frame of the initial discontinuity, the initial velocities on either side are 0, assuming a wind velocity that is constant throughout the computational domain.

The one-dimensional Riemann problem can be solved analytically. I used the exact Riemann solver provided as a Fortran program in the library NUMERICA (Toro 1999). Figure 6.2 shows the results at the time $t = 10\,\mathrm{yrs}$, which include a shock wave traveling to the left, i. e. in the direction of the low temperature in the neutral wind, at a velocity v_SL of about three times the sound speed, and a rarefaction wave moving into the hot region.

Two velocities characterize the rarefaction wave: the velocity v_SRH of its *head* and v_SRT of its *tail*. The head of the wave is moving at a greater speed as the tail and marks the beginning of the yet undisturbed region to the right (see Fig. 6.2). The tail marks the transition between the wave and the material it has already passed. Table 6.2 lists the velocities characterizing the two waves and the sound speeds corresponding to the initial left and right states.

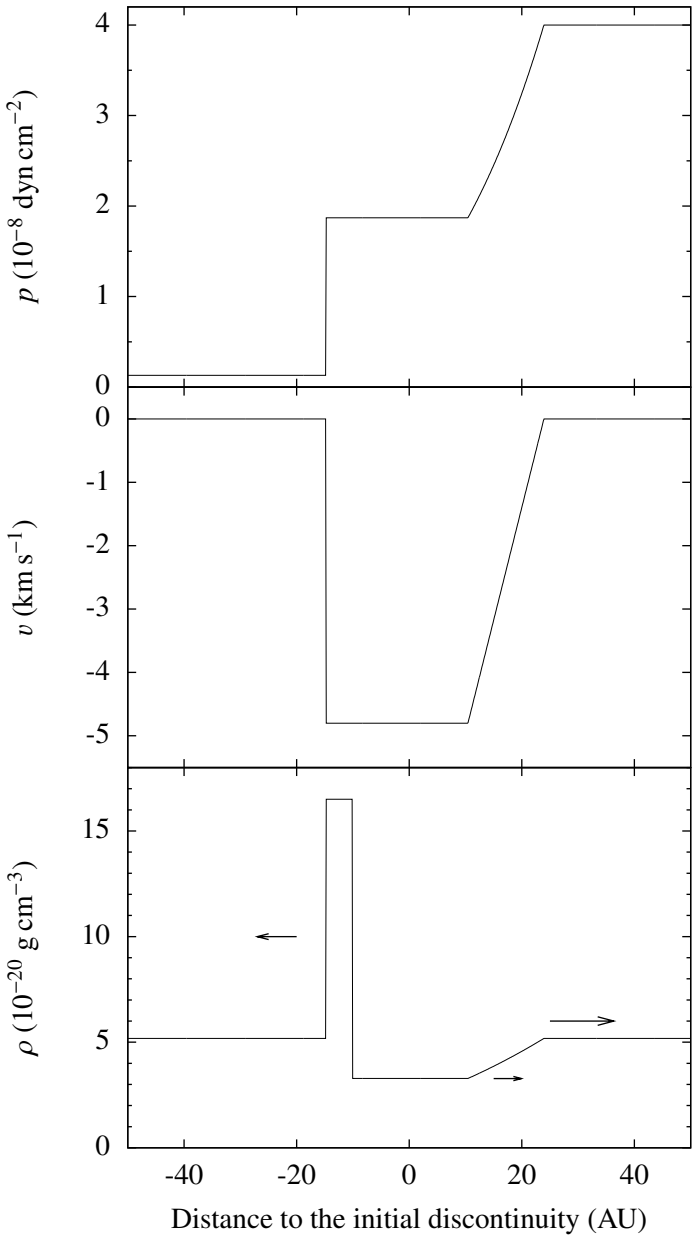

Figure 6.2: Solution at $t = 10$ yrs of the Riemann problem presented in Fig. 6.1. The arrows in the plot of the density indicate the velocitiy of the shock wave that is moving to the left at $v_{\mathrm{SL}} = -6.99$ km s^{-1} and of the rarefaction wave moving to the right. The head and tail of the rarefaction wave are moving at velocities of $v_{\mathrm{SRH}} = 11.34$ and $v_{\mathrm{SRT}} = 4.94$ km s^{-1}, respectively.

Table 6.2: Wave and sound speeds in the solution of the Riemann problem (see Fig. 6.2).

Quantity	Value ($\mathrm{km\,s^{-1}}$)
a_L	2.05
v_SL	-6.99
a_R	11.34
v_SRH	11.34
v_SRT	4.94

Notes. a_L and a_R are the sound speeds in the left and right state, respectively (cf. Fig. 6.1), v_SL the velocity of the shock wave, and v_SRH and v_SRT the velocity of the head and tail of the rarefaction wave, respectively.

6.2 Resulting density and velocity distributions

As the results of the previous section suggest, the presence of the hot H II region inside the circumstellar envelope of α Sco produces severe disturbances in the distributions of density and velocity, which are smooth in the undisturbed initial state. Figure 6.3 shows the density distribution resulting from a simulation of the α Sco system at different time steps. The effects of the heating by the radiation of the B star are density enhancements that form at the shock front at the boundary to the cool wind and then move outward with the wind. Inside the H II region and behind it, in its wake, the density is reduced with respect to the undisturbed spherically expanding case. The curved shape results from the orbital motion.

After about one half of an orbit, i. e. at a phase of 0.5, the density distribution reaches a quasi-stationary state. The low-density region produced by the influence of the H II region and its high-density boundaries do not change their shape anymore but merely move with the B star around the center of mass.

The velocity vectors, which are initially the sum of the terminal wind velocity v_∞ in radial direction and the velocity of the supergiant, change considerably when the H II region is included (see Fig. 6.4). They change mainly in their absolute values, while changes in direction are hardly noticeable. The absolute value of the velocity in the resulting low-density region is up by about 50 % with respect to the undisturbed region.

Figure 6.5 shows the pressure distribution corresponding to the final states presented in Figs. 6.3 and 6.4. The pressure was derived from the total energy E according to

$$p = (\gamma - 1)\left(E - \frac{1}{2}\rho \boldsymbol{v}^2\right) \tag{6.3}$$

(see Eqs. 5.4 and 5.5), with $\gamma = 5/3$, which applies to a monatomic gas.

As an illustration of the whole three-dimensional structure, Fig. 6.6 shows the density and velocity distribution perpendicular to the plane of the orbit. The left panel shows a transverse section perpendicular to the y axis, the right panel a transverse section perpendicular to the x axis. Both transverse sections refer to a position equal to 3/4 of the edge length, i. e. $y \sim 4672$ AU in the left panel and

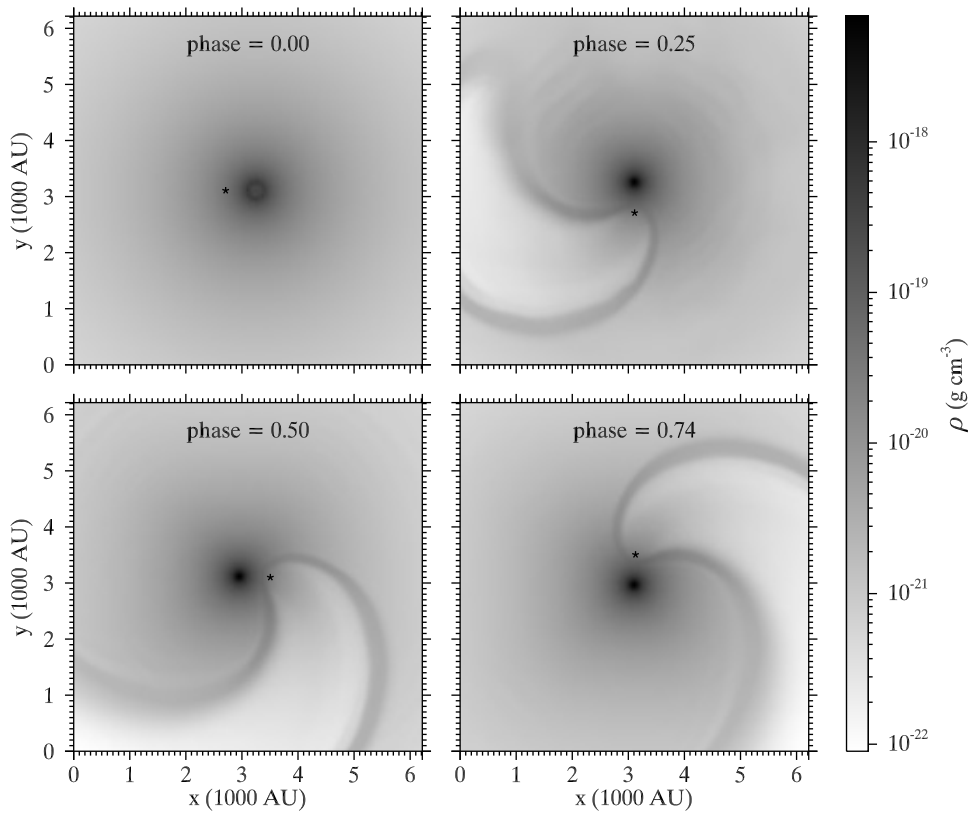

Figure 6.3: Density structure at different time steps (binary phases) in a simulation using $\dot{M} = 1.05 \times 10^{-6}\ M_{\odot}\,\mathrm{yr}^{-1}$ and $v_{\infty} = 20\ \mathrm{km\,s}^{-1}$. The asterisk marks the position of the B star.

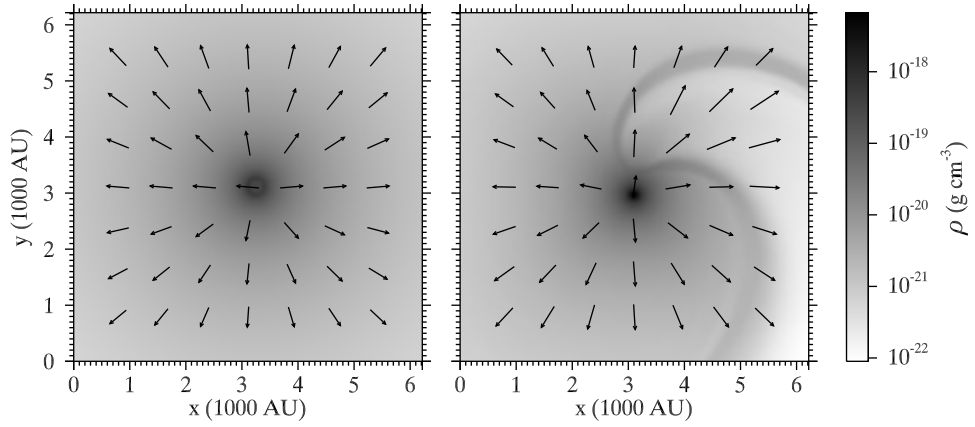

Figure 6.4: Velocity and density distributions in the undisturbed initial state (left, phase = 0) and at a phase of 0.74 (right). The length of the arrows indicates the absolute value of the velocity. Note the increased velocity inside the low-density region. The data result from the same simulation as those presented in Fig. 6.3.

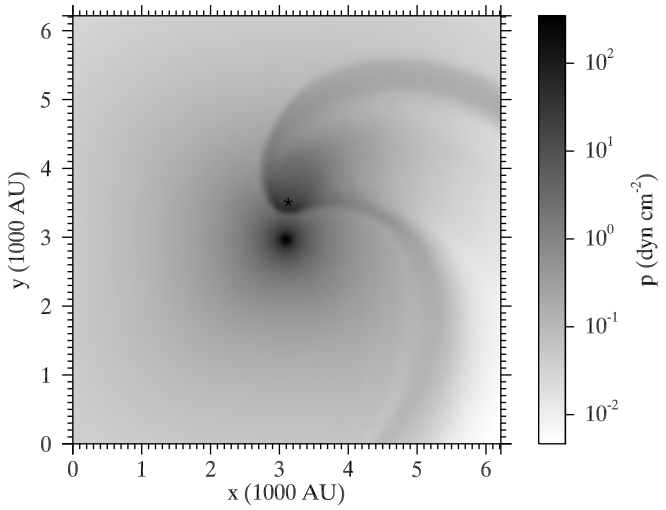

Figure 6.5: Pressure distribution at a phase of 0.74. The data result from the same simulation as those presented in Figs. 6.3 and 6.4.

$x \sim 4672$ AU in the right panel. These transverse sections also show the symmetry with respect to the plane of the orbit, which is located at $z \sim 3108$ AU.

In order to include density structures at larger distances in the analysis, I extended the edge lengths of the computational domain a_x in x and a_y in y direction and took advantage of the symmetry of the system by leaving out most of the region above the plane of the orbit. The resulting domain has edge lengths of $a_x = a_y \sim 12\,433$ and $a_z \sim 3419$ AU, and the z coordinate of the plane of the orbit, which equals the z position of the center of mass (cms), is $z_{\rm cms} \sim 3108$ AU.

The values of the parameters $\dot{M}$ and v_∞ used for the simulations presented in this work range from 2×10^{-7} to 5×10^{-6} $M_\odot\,{\rm yr}^{-1}$ and from 10 to 40 $\rm km\,s^{-1}$, respectively. Figure 6.7 shows results from simulations with a mass-loss rate of $\dot{M} = 10^{-6}$ $M_\odot\,{\rm yr}^{-1}$ and different values for v_∞. The density scale inside the expanding envelope is determined by the mass-loss rate and the wind velocity via

$$\rho(r) = \frac{\dot{M}}{4\pi r^2 v(r)} \tag{6.4}$$

(see Eq. 2.2). Thus, an increase of the velocity implies a decrease of the density, which leads to a more extended H II region with a more extended wake. Therefore, the simulation based on the terminal wind velocity $v_\infty = 40$ $\rm km\,s^{-1}$ exhibits the most extended, and the simulation with $v_\infty = 10$ $\rm km\,s^{-1}$ the least extended density structure.

Figure 6.8 shows the density and velocity distributions corresponding to simulations with a mass-loss rate of $\dot{M} = 2 \times 10^{-7}$ $M_\odot\,{\rm yr}^{-1}$, respectively, and three different values of v_∞. The density in the simulations corresponding to $v_\infty = 40$ and 20 $\rm km\,s^{-1}$ is so low that the H II region is no longer bounded in the directions away from the supergiant, and the resulting density structures are less pronounced than those presented in Fig. 6.7. In the simulation corresponding to

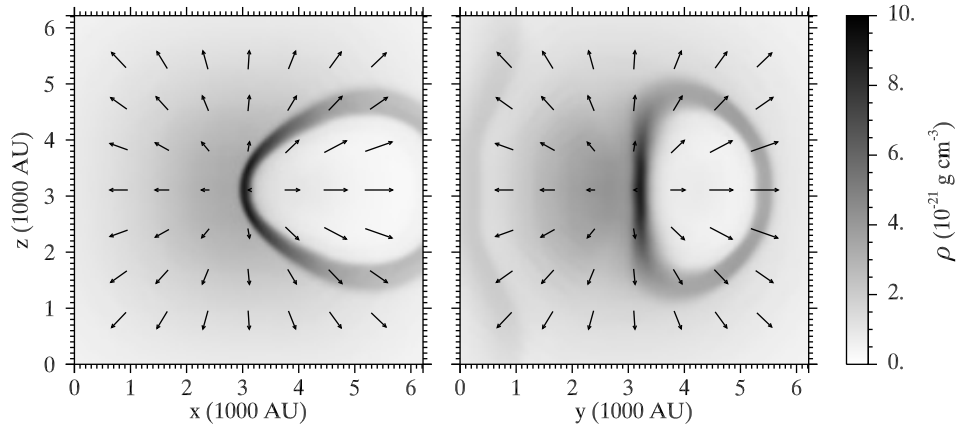

Figure 6.6: Density and velocity distributions perpendicular to the plane of the orbit, resulting from the same simulation as the data presented in Figs. 6.3 to 6.5. The left panel is a transverse section perpendicular to the y axis ($y = 3/4$ of the edge length), the right panel a transverse section perpendicular to the x axis ($x = 3/4$ of the edge length). The z axis is perpendicular to the plane of the orbit.

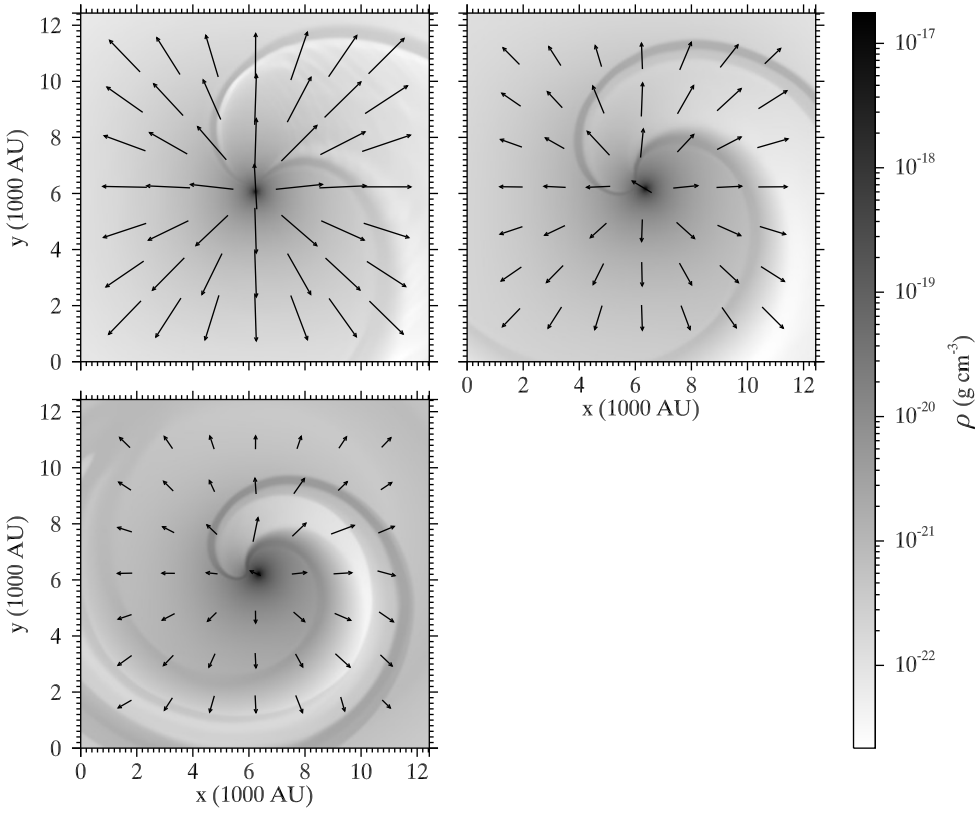

Figure 6.7: Density and velocity distributions in the plane of the orbit for a mass-loss rate of $\dot{M} = 10^{-6}\ M_\odot\,\mathrm{yr}^{-1}$ and a terminal wind velocity of $v_\infty = 40$ (top left), 20 (top right), and 10 $\mathrm{km\,s}^{-1}$ (bottom left).

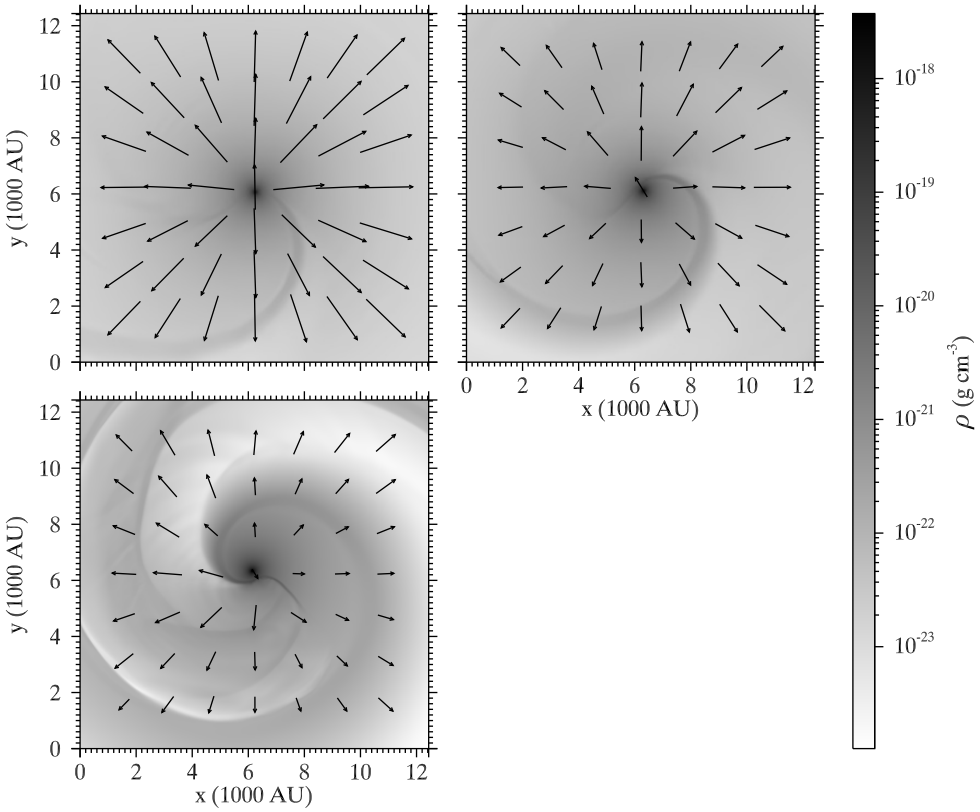

Figure 6.8: Density and velocity distributions in the plane of the orbit for a mass-loss rate of $\dot{M} = 2 \times 10^{-7}\ M_\odot\,\mathrm{yr}^{-1}$ and a terminal wind velocity of $v_\infty = 40$ (top left), 20 (top right), and 10 $\mathrm{km\,s}^{-1}$ (bottom left).

$v_\infty = 10\ \mathrm{km\,s}^{-1}$, a closed H II region is present, which is yet so extended that the travel time $t_{\max} = r_{\max}/v_\infty \sim 2790$ yrs corresponding to the maximum extension $r_{\max} \sim 5800$ AU of the H II region is of the same order of magnitude as the orbital period. Thus, parts of the material that leave the range of influence of the ionizing radiation of the B star come again into its range after one orbit. This is the reason for the higher complexity of the density structure as compared to the top panels of Fig. 6.8.

Similarly, Fig. 6.9 shows density and velocity distributions resulting from simulations with a mass-loss rate of $\dot{M} = 5 \times 10^{-6}\ M_\odot\,\mathrm{yr}^{-1}$.

6.3 Time scales of cooling and heating

The simulations of the α Sco system involve hydrodynamic as well as radiative and microphysical processes, which take place on different time scales. The plasma simulations performed with the Cloudy program that yield the temperature of the material in the expanding envelope (see Sect. 5.2) are based on the assumption that the material is at rest and that all processes have become time steady.

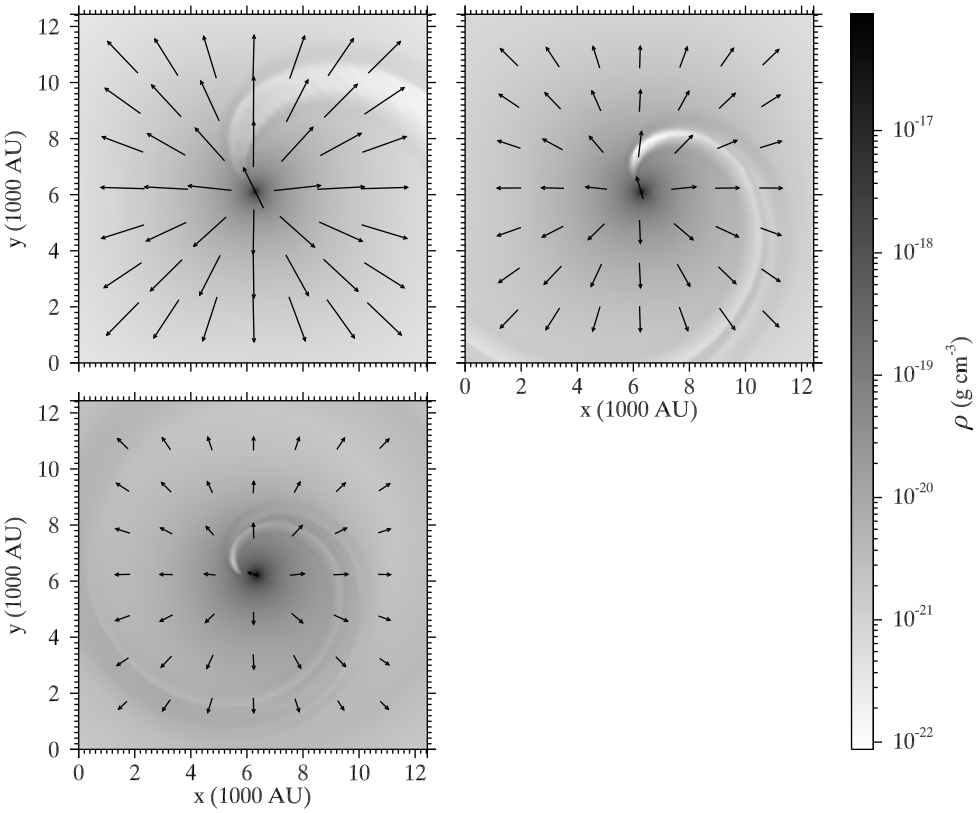

Figure 6.9: Density and velocity distributions in the plane of the orbit for a mass-loss rate of $\dot{M} = 5 \times 10^{-6}\ M_{\odot}\,\mathrm{yr}^{-1}$ and a terminal wind velocity of $v_{\infty} = 40$ (top left), 20 (top right), and 10 km s^{-1} (bottom left).

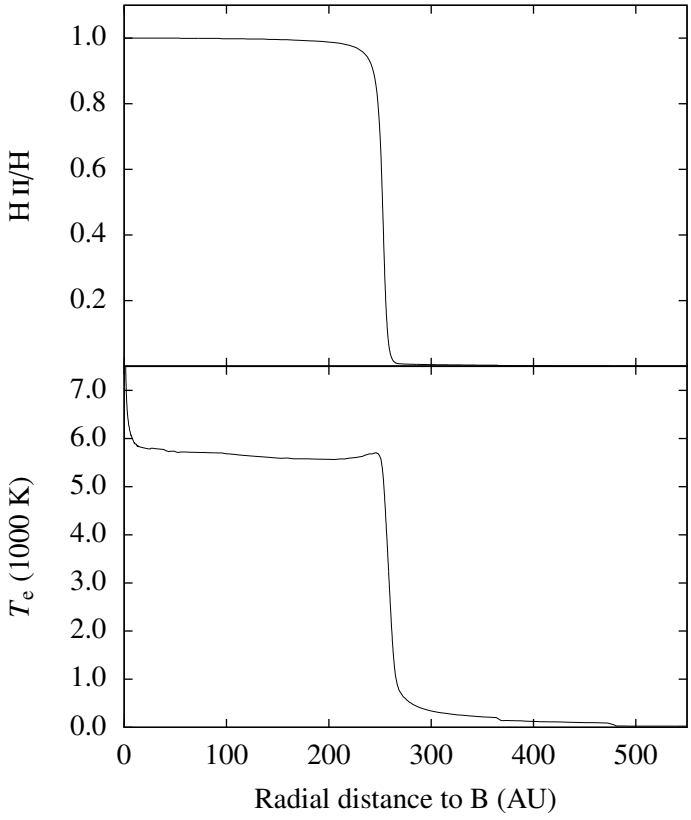

Figure 6.10: $n_{\mathrm{H\,II}}/n_{\mathrm{H}}$ and electron temperature in the direction $\phi = 4.712$ from the B star (cf. Fig. 6.11).

They result in an ionized region with a high temperature that is surrounded by a cool region, in which all hydrogen has recombined. See Fig. 6.10 as an example for the temperature and H II/H fraction as a function of distance to the B star in a simulation with $\dot{M} = 10^{-6}\ M_\odot\,\mathrm{yr}^{-1}$ and $v_\infty = 20\ \mathrm{km\,s}^{-1}$.

The temperature $T_{\mathrm{Cl}}(r, \theta, \phi)$ resulting from the Cloudy calculations was introduced into the hydro simulation as a boundary condition, which means that the temperature in the grid cells that come into range of the ionizing radiation of the B star or leave this range undergo instantaneous temperature changes. This is only a good approximation if the microphysical and radiative processes take place on much smaller time scales than the macroscopic dynamics of the α Sco system that are related to the expansion of the common envelope and the orbital motion, and it may not be valid near the boundary of the H II region, where large gradients are present in the temperature and the ionization fraction (see Fig. 6.10).

The temperature derives from the total energy E according to

$$T_{i,j,k} = \frac{\gamma - 1}{R}\left(\frac{E_{i,j,k}}{\rho_{i,j,k}} - \frac{\boldsymbol{v}^2_{i,j,k}}{2}\right) \tag{6.5}$$

(cf. Eqs. 5.4 to 5.6), where the subscripts indicate the position of the grid cell in x, y, and z direction. The boundary condition was implemented in two different ways. In one approach, the temperature in every grid cell (x_i, y_j, z_k) of the hydro model is set equal to the value given by the Cloudy data at every time step. In the other approach, the Cloudy data are only used for increasing the temperature in grid cells whose temperatures are smaller than the temperatures resulting from the Cloudy simulation, i. e. where $T_{i,j,k} < T_{\mathrm{Cl}}$. Thus, in both cases, the heating of the wind material takes place instantaneously in grid cells that come into range of the ionizing radiation of the B star. The approach that uses the Cloudy results only for heating implies that the only cooling mechanism is adiabatic expansion (see below).

In order to decide which of these approaches is a better approximation of the exact physical processes that take place at the boundary of the H II region, the heating and cooling rates must be compared to a characteristic dynamic time scale of the α Sco system, which can be derived from the velocity scale, i. e. the terminal wind velocity v_∞, and a characteristic length scale, e. g. the separation $D \sim 549$ AU of the two components. As the orbital velocity of the B star $v_\mathrm{B} \sim 4.6\,\mathrm{km\,s^{-1}}$ is much smaller than v_∞, the latter is chosen as the characteristic velocity scale. The resulting time scale, the wind travel time (see Reimers et al. 2008), is $t_\mathrm{wind} = D/v_\infty \sim 129$ yrs.

6.3.1 Static thermal balance

The cooling and heating rates that result from the ionization balance and radiative losses depend on the local density and temperature. Table 6.3 lists the parameters describing the physical conditions at the boundary of the H II region, i. e. at the point where the fraction $n_{\mathrm{H\,II}}/n_\mathrm{H}$ has fallen below 0.9, in four different directions from the B star in the orbital plane. The direction $\phi = 0$ represents the line connecting the two stars, the direction $\phi = 1.169$ is the line of sight to α Sco B, and $\phi = 3\pi/2 \sim 4.712$ is the direction of orbital motion on the far side of the B star. In these directions from the B star, the H II region is bounded by a shock front with an enhanced density, as shown in Fig. 6.11. The other direction, $\phi = 2.985$, is chosen such that the H II region extends further outwards and ends inside the low-density region in the wake of the H II region.

The values result from a simulation with a mass-loss rate of $10^{-6}\,M_\odot\,\mathrm{yr^{-1}}$ and a terminal wind velocity of $v_\infty = 20\,\mathrm{km\,s^{-1}}$. Cloudy assumes that the material is in thermal balance, so that the cooling rate and cooling time scale equal the heating rate and heating time scale, respectively. The cooling time scale is given by

$$t_\mathrm{cool} = \frac{3n\mathrm{k_B}T_\mathrm{e}}{2C}, \tag{6.6}$$

where n is the total particle density and C the total cooling rate due to processes included in the Cloudy simulations, such as radiative cooling and cooling by recombination.

Table 6.3: Physical conditions at the boundary of the H II region in the plane of the orbit.

Direction (ϕ)	$r_{\rm bnd}$ (AU)	$n_{\rm H}$ (10^3 cm^{-3})	$T_{\rm e}$ (K)	C	$t_{\rm rec}$ (yrs)	$t_{\rm cool}$ (yrs)
0.000	160	44.78	6250	1782.3	2.27	2.07
1.169 (los)	213	26.67	5900	665.87	3.65	3.14
2.985	895	1.17	4030	1.70	62.15	36.47
4.712	244	19.44	5700	357.82	4.85	4.09

Notes. $n_{\rm H}$ is the total number density of hydrogen, $r_{\rm bnd}$ the radial distance of the boundary to the B star, $T_{\rm e}$ the electron temperature, C the cooling rate in units of 10^{-18} erg cm^{-3} s^{-1}, $t_{\rm rec}$ the hydrogen recombination time scale and $t_{\rm cool}$ the cooling time scale. The boundary of the H II region is defined here as the point where the H II/H fraction has fallen below 0.9.

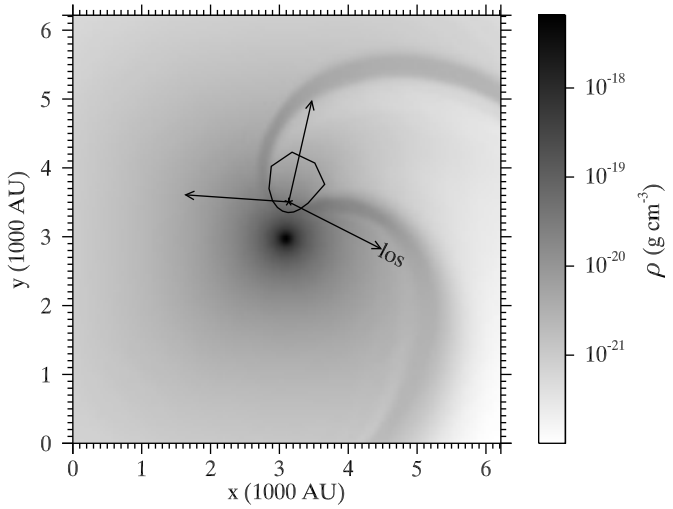

Figure 6.11: Density distribution in the orbital plane with a contour indicating roughly the boundary of the H II region in a simulation with $\dot{M} = 1.05 \times 10^{-6}\ M_\odot\,{\rm yr}^{-1}$ and $v_\infty = 20\ {\rm km\,s}^{-1}$. The arrows indicate the line of sight (los, $\phi = 1.169$) to the B star, and the directions $\phi = 2.985$ and $\phi = 4.712$, where ϕ is measured counterclockwise.

6.3.2 Cooling by adiabatic expansion

Another cooling mechanism results from the expansion of the circumstellar envelope, which is adiabatic outside the range of the radiation of the B star and consequently leads to a loss of internal energy. The cooling rate can be estimated by use of the relation

$$T = T_0 \left(\frac{n}{n_0} \right)^{\gamma - 1}, \tag{6.7}$$

which applies to adiabatic processes of ideal gases with the starting temperature and (number) density T_0 and n_0 and the final values T and n after the expansion. For the ratio of specific heats the value for a monatomic gas, $\gamma = 5/3$, is used.

For a comparison with the cooling rates presented in Table 6.3 the loss of internal energy by adiabatic expansion can be estimated by considering the density and temperature in the region of the western boundary of the H II region, which is located in the direction $\phi \sim \pi$ at a distance $r_{\mathrm{bnd}} = 1444$ AU to the primary star. Assuming a distance $\Delta r = 50$ AU to the boundary of the H II region, the values of the internal energy $e = 3nk_{\mathrm{B}}T_{\mathrm{e}}/2$ are $e_0 \sim 3.6 \times 10^{-9}$ erg cm^{-3} at $r = r_{\mathrm{bnd}} - \Delta r$ (inside the H II region) and $e \sim 2.9 \times 10^{-9}$ erg cm^{-3} at $r = r_{\mathrm{bnd}} + \Delta r$ (outside the H II region), with the densities n_0 and n given by Eq. 2.4, $T_0 = 5000$ K as a mean electron temperature inside the H II region and $T \sim 4560$ K given by Eq. 6.7. Now the travel time $\Delta t \sim 2\Delta r / v_\infty \sim 23.7$ yrs yields the estimation

$$C_{\mathrm{exp}} = \frac{e_0 - e}{\Delta t} \sim 10^{-18} \text{ erg cm}^{-3} \text{ s}^{-1} \tag{6.8}$$

for the cooling rate C_{exp} caused by adiabatic expansion. This value is much smaller than the cooling rate due to radiative and microphysical processes in most directions, but it is of the same order of magnitude in the direction $\phi = 2.985$ (see Table 6.3). Thus, cooling by adiabatic expansion is only important near the western boundary of the H II region.

The results listed in Table 6.3 show that the cooling (heating) time scales in the directions where the H II region is bounded by the high-density shock front ($\phi = 0$, $\phi = 1.169$, and $\phi = 4.712$) are small in comparison to t_{wind} so that the assumption of instantaneous heating and cooling seems reasonable. In the direction $\phi = 2.985$ this assumption is not valid. To get an idea of the effects of cooling and heating time scales, see Fig. 6.12 for a comparison of the results of two simulations using the two different approaches described above for heating and cooling. The left panel of Fig. 6.12 shows the density distribution resulting from a simulation using instantaneous heating and cooling. The right panel results from a simulation using instantaneous heating and no microphysical or radiative cooling, i. e. the cooling is only due to adiabatic expansion.

The main difference between the two results presented in Fig. 6.12 resides in the extension of the wake of the H II region in the direction of motion of the B star. When the cooling is governed by adiabatic expansion, as in the right panel of Fig. 6.12, the shock wave can expand freely, so that the extension of the wake of the H II region is larger than in the results obtained with instantaneous cooling.

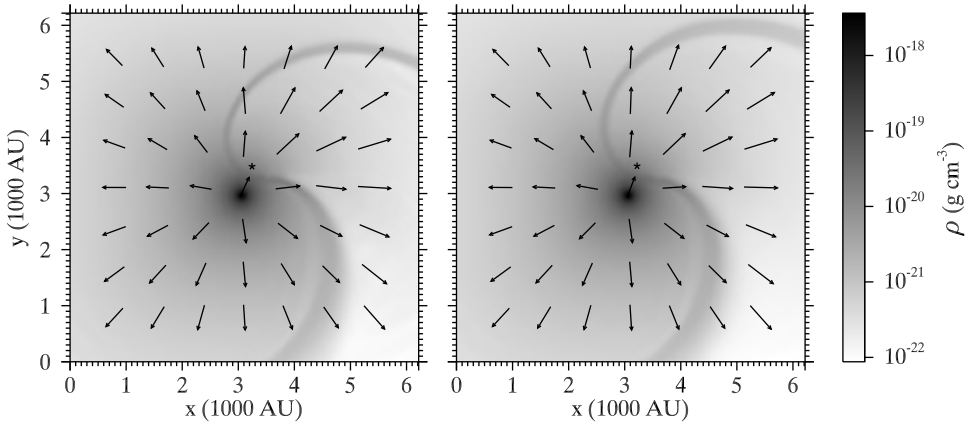

Figure 6.12: Density and velocity distribution for a simulation assuming instantaneous cooling (left) and a simulation neglecting radiative and microphysical cooling effects (right).

The difference in the extensions resulting from the two calculations amounts to $\sim$ 300 AU in the outer parts of the domain in the top right of the plots in Fig. 6.12.

This discrepancy shows that the lacking knowledge of the real dynamic cooling rates introduces a systematic error. Moreover, the fact that Cloudy calculates the ionization balance only for the time-steady case and does not include effects of advection also introduces an error in the calculation of the ionization structure of the common envelope of the α Sco system (see the next section). Most of the hydrodynamic results presented in this work are based on the assumption of instantaneous heating without radiative cooling effects.

6.4 Advection effects at the ionization front

The calculation of the temperature and ionization structure of the H II region around α Sco B, which was carried out with the Cloudy program (see Sect. 5.2.1), does not include any dynamic effects. This might introduce a systematic error, as has already been shown in the previous section in the context of the cooling time scale at the western boundary of the H II region.

The recombination time scale of hydrogen is listed in Table 6.3. In the directions $\phi = 0$, $\phi = 1.169$ and $\phi = 4.712$ it is much smaller than the wind travel time $t_{\rm wind} \sim 129$ yrs (see previous section), but at the western boundary ($\phi = 2.985$) it is of the same order of magnitude. Cloudy comprises a preliminary version of a subroutine that includes advective source and sink terms in the equilibrium balance equations of ionization and energy (see Henney et al. 2005), which makes it possible to include advection effects for a flow towards the source of ionizing radiation, i. e. for a flow from the cool part of the circumstellar envelope towards the B star in the case of α Sco.

Figure 6.13 shows the temperature and hydrogen ionization as a function of

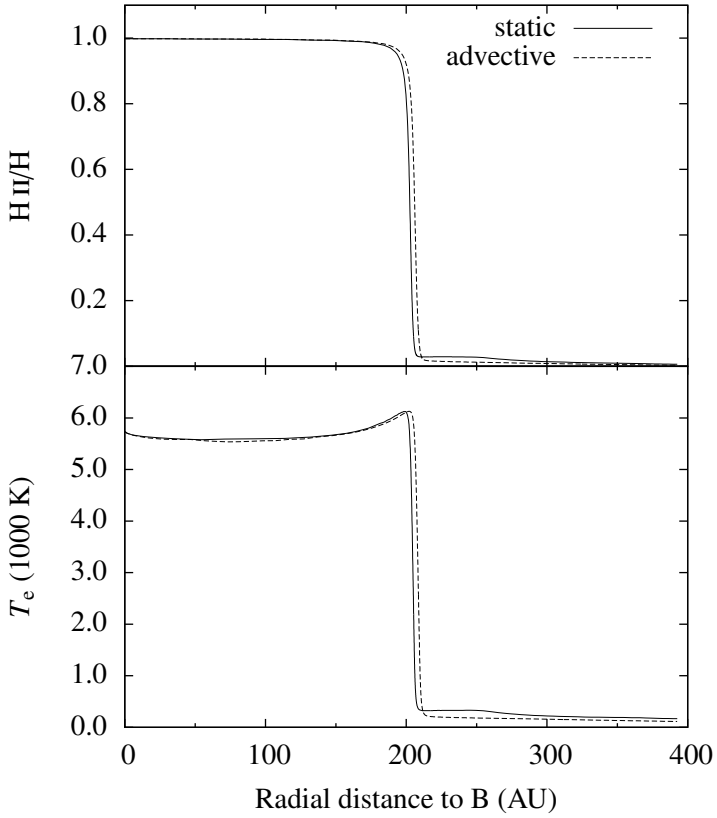

Figure 6.13: $n_{\mathrm{H\,II}}/n_{\mathrm{H}}$ and electron temperature in the direction $\phi = 0$ from the B star, towards the supergiant, with and without advective effects.

distance to the B star in the direction $\phi = 0$ for simulations with and without advective effects caused by a wind with a velocity of 20 km s^{-1}. The calculations were performed for a plane-parallel geometry and a density distribution as given by Eq. 2.4 with $\dot{M} = 10^{-6}\ M_{\odot}\,\mathrm{yr}^{-1}$ and $v_{\infty} = 20$ km s^{-1}. As expected, advective effects do not play a major role in the direction towards the supergiant but only induce a change of ~ 4 AU of the position of the ionization front.

6.5 Spatial resolution of the hydrodynamic simulations

The spatial step size Δx and the number of levels of refinement (see Sect. 5.1.4) of the hydro simulations determine the size of the smallest structures the simulation can resolve. These parameters also determine the number of grid cells for a given size of the computational domain and thus the computing time. Most of the calculations presented in this work were carried out with a step size of $\Delta x \sim 77.7$ AU and 2 levels of refinement, resulting in a step size of $\Delta x_{\mathrm{fine}} \sim 38.9$ AU on the finest

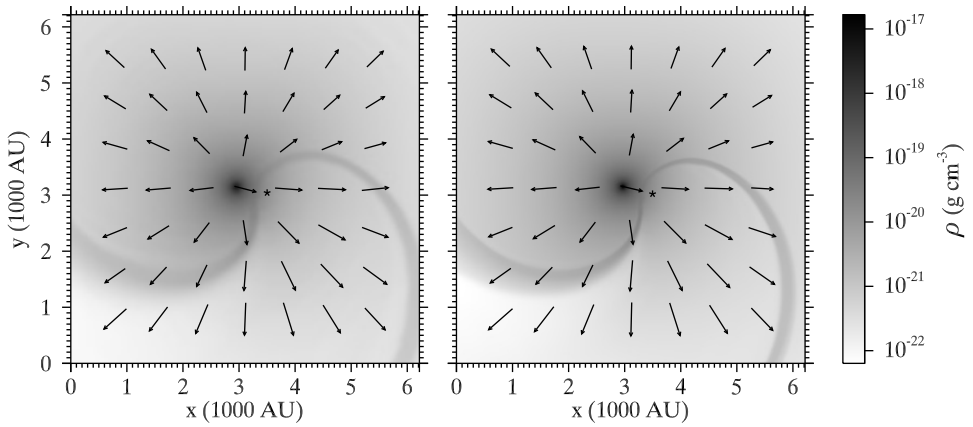

Figure 6.14: Density and velocity distributions for simulations with $\Delta x_{\rm fine} \sim 38.9$ AU (left) and $\Delta x_{\rm fine} \sim 19.4$ AU (right).

grids.

Figure 6.14 shows a comparison of the density and velocity distributions resulting from simulations of the α Sco system with different resolutions. The left panel results from a simulation with $\Delta x_{\rm fine} \sim 38.9$ AU, with a mass-loss rate of $\dot{M} = 5 \times 10^{-7}\ M_\odot\,{\rm yr}^{-1}$ and a terminal wind velocity of $v_\infty = 20\ {\rm km\,s}^{-1}$. The right panel results from a simulation with the same $\dot{M}$ and v_∞, but with a step size of $\Delta x_{\rm fine} \sim 19.4$ AU, i. e. with a spatial resolution that is twice as high. Obviously, the shape of the density structures and the velocity do not change at large when the resolution is increased, but the density enhancement at the shock front becomes narrower and more pronounced.

Chapter 7

Prediction of absorption-line profiles

The wind from α Sco A produces absorption features in the spectrum of α Sco B (see e. g. Baade & Reimers 2007). If the aperture of the telescope is so large that it also covers a large part of the circumstellar envelope, P Cygni-type profiles are observed.

For the time-independent case the formal solution of the radiative transfer equation along a ray reads

$$I_x = I_\mathrm{B} e^{-\tau_x} + \int_0^{\tau_\mathrm{max}} S_x(\tau_x) e^{-\tau_x} \,\mathrm{d}\tau_x \tag{7.1}$$

(e. g. Rybicki 1984, p. 27), where S_x is the source function, $x = (\nu - \nu_0)/\Delta\nu_D$ gives the relative frequency divided by the Doppler width

$$\Delta\nu_D = \frac{\nu_0}{c}\sqrt{v_{th}^2 + \xi^2} \tag{7.2}$$

that results from constant thermal (v_{th}) and microturbulent (ξ) motions, and I_B is the specific intensity of the B-star spectrum at that frequency for rays starting at the surface of the B star. τ_x is the optical depth integrated over the path length s along the line of sight,

$$\tau_x = \int \chi_x \,\mathrm{d}s, \tag{7.3}$$

where the opacity χ_x relates to the line-profile function Φ_x according to

$$\chi_x = \frac{\pi e^2}{m_\mathrm{e} c} n_\mathrm{l} f_\mathrm{lu} \left(1 - \frac{g_\mathrm{l} n_\mathrm{u}}{g_\mathrm{u} n_\mathrm{l}}\right) \Phi_x \tag{7.4}$$

(cf. Mihalas 1978, p. 80). n_l, n_u, g_l, and g_u are the number density of ions in the lower and upper state l and u, respectively, and the statistical weights of these states, while f_lu is the oscillator strength of the transition. In my analysis I used resonance lines, for which $n_\mathrm{u} \ll n_\mathrm{l}$, so that Eq. 7.4 reduces to

$$\chi_x = \frac{\pi e^2}{m_\mathrm{e} c} n_\mathrm{l} f_\mathrm{lu} \Phi_x. \tag{7.5}$$

The dominant mechanism determining the line-profile function is the change of radial velocity v_r of the material along the line of sight, which gives the Doppler profile

$$\Phi_x = \frac{1}{\sqrt{\pi}} e^{-(x-V)^2}, \tag{7.6}$$

where

$$V = \frac{v_r}{\sqrt{v_{th}^2 + \xi^2}}. \tag{7.7}$$

The P Cyg-type line-profiles resulting from absorption of radiation in the line of sight to α Sco B and scattering of photons in an extended region around it have been calculated by Hagen et al. (1987). Based on observations with the International Ultraviolet Explorer (IUE) and the assumption of a radially symmetric velocity field and density distribution around the supergiant they obtained line profiles corresponding to a mass-loss rate of $\sim 10^{-6}\ M_\odot\,\mathrm{yr}^{-1}$. It was however noticed that different ions yielded different mass-loss rates.

In my study I neglected the contribution of the emission component that is due to the line scattering, because the most recent spectroscopic observations of α Sco B performed with HST/GHRS (Baade & Reimers 2007) show only a very small emission component due to the small aperture. I concentrated on these HST data because they provide a higher spectral resolution and a better signal-to-noise (S/N) ratio than previous data. For example, IUE provides a resolution of $\sim 20\,\mathrm{km\,s}^{-1}$ (Garhart et al. 1997) while the HST/GHRS spectra have a resolution of $\sim 3.5\,\mathrm{km\,s}^{-1}$. In terms of the S/N ratio, the 2.4 m mirror of HST of course outranks the 45 cm mirror of IUE.

A pure absorption line is described by

$$I_x = I_\mathrm{B} \exp\left(-\int \chi_x \,\mathrm{d}s\right). \tag{7.8}$$

7.1 Including hydrodynamics

For the calculation of absorption lines in α Sco I used a computer program called ZETAUR designed by Hempe (1982) to perform the integration described by Eq. 7.8. The program provides an automatic adjustment of the optical-depth increment at each integration step and a general treatment of the coordinate transformations that are necessary for the prediction of the flux measured by an observer from an arbitrary direction with respect to the orbit of the binary star. ZETAUR starts from the coordinates (Z'', P'', Q''), where Z'' points towards the observer, and P'' and Q'' are impact parameters with $Q'' = 0$ at the position of the primary star. These coordinates are transformed to an 'orbital' coordinate system (Z, P, Q), where Z and P lie in the plane of the orbit and P is pointing to the primary.

The transformation matrix is

$$\mathsf{T} = \begin{bmatrix} \cos(\omega+f)\sin i & \begin{matrix}\sin(\omega+f)\sin\Omega \\ -\cos(\omega+f)\cos\Omega\cos i\end{matrix} & \begin{matrix}\sin(\omega+f)\cos\Omega \\ +\cos(\omega+f)\sin\Omega\cos i\end{matrix} \\ -\sin(\omega+f)\sin i & \begin{matrix}\cos(\omega+f)\sin\Omega \\ +\sin(\omega+f)\cos\Omega\cos i\end{matrix} & \begin{matrix}\cos(\omega+f)\cos\Omega \\ -\sin(\omega+f)\sin\Omega\cos i\end{matrix} \\ -\cos i & -\cos\Omega\sin i & \sin\Omega\sin i \end{bmatrix} \tag{7.9}$$

(see Hempe 1982), where ω is the longitude of periastron as measured from the ascending node of the orbit, f the true anomaly, i. e. the angle between the periastron and the position of the star measured in the direction of motion, i is the inclination of the orbit, and $\Omega = [\tan(\omega+f)\cos i]^{-1}$ is the angle between the Q'' axis and the ascending node. The transformation reads

$$\begin{pmatrix} Z \\ P \\ Q \end{pmatrix} = \mathsf{T} \begin{pmatrix} Z'' \\ P'' \\ Q'' \end{pmatrix}. \tag{7.10}$$

This corresponds to three successive rotations, namely

1. a clockwise rotation by $\Omega + \pi/2$ about the Z'' axis,
2. a clockwise rotation by $\pi/2 + i$ about the resulting P'' axis, and
3. a counterclockwise rotation by $\omega + f + \pi$ about the resulting Q'' axis, so that the P axis points to the primary.

The density and velocity information is given by the hydrodynamic results produced by AMRCART. For the transfer of information between the two programs I modified the transformation described above to obtain a transformation $\mathsf{T}_{\mathrm{AMR}}$ from the coordinate system (Z'', P'', Q'') used in ZETAUR for arbitrary orbits to the AMRCART system. In the AMRCART coordinate system (x, y, z) the y axis points to the periastron of the orbit described in the rest frame of the primary star and the orbital motion is counterclockwise about the z axis. Therefore, the angle by which the third rotation in T is performed needs to be changed to $\omega + \pi$. The resulting transformation matrix reads

$$\mathsf{T}_{\mathrm{AMR}} = \begin{pmatrix} \cos\omega\sin i & \begin{matrix}\sin\omega\sin\Omega \\ -\cos\omega\cos\Omega\cos i\end{matrix} & \begin{matrix}\sin\omega\cos\Omega \\ +\cos\omega\sin\Omega\cos i\end{matrix} \\ -\sin\omega\sin i & \begin{matrix}\cos\omega\sin\Omega \\ +\sin\omega\cos\Omega\cos i\end{matrix} & \begin{matrix}\cos\omega\cos\Omega \\ -\sin\omega\sin\Omega\cos i\end{matrix} \\ -\cos i & -\cos\Omega\sin i & \sin\Omega\sin i \end{pmatrix}, \tag{7.11}$$

Table 7.1: Transitions seen in absorption in the spectrum of α Sco B.

Ion	E_l (cm^{-1})	E_u (cm^{-1})	Multiplet no.	λ_{vac} (Å)	Instrument
Cu II	0	73595.813	UV 3	1358.773	GHRS
Ni II	0	71770.83		1393.324	GHRS
Cr II	0	48491.053	UV 1	2062.236	GHRS
Zn II	0	48481.077	UV 1	2062.660	GHRS
Fe II	977.053	39109.307	UV 1	2622.452	GHRS
Ti II	94.110	30958.582	2	3239.971	UVES
Ti II	0	29544.451	1	3384.730	UVES
Ca II	0	25414.414	1	3934.775	UVES
Ca II	0	25191.518	1	3969.590	UVES

Notes. E_l and E_u are the energies of the lower and upper levels, respectively. The multiplet numbers refer to Moore (1952), the energies and vacuum wavelengths are taken from Morton (2003).

and the complete transformation is

$$\begin{pmatrix} x \\ y \\ z \end{pmatrix} = \begin{pmatrix} x_B \\ y_B \\ z_B \end{pmatrix} + \mathsf{T}_{AMR} \begin{pmatrix} Z'' \\ P'' \\ Q'' \end{pmatrix}. \tag{7.12}$$

7.2 Absorption lines in the spectrum of α Sco B

Baade & Reimers (2007) presented observations of circumstellar absorption lines in the spectrum of α Sco B obtained with HST/GHRS. In addition, circumstellar absorption has been observed with the UVES spectrograph at the VLT[1]. In this section, these observations will be compared to theoretical line profiles derived from the simulations presented in this work. The lines that are used for the comparison are listed in Table 7.1. Line profiles corresponding to the hydrodynamic simulations with the extreme values of $\dot{M}$ and v_∞ presented in Sect. 6.2 (cf. Figs. 6.7 to 6.9) are not presented here as they cannot reproduce the observed profiles. A set of three simulations in a smaller range of mass-loss rates is used instead (5×10^{-7}, 10^{-6}, 2×10^{-6} $M_\odot$ yr^{-1}), and the wind velocity is fixed at $v_\infty = 20$ km s^{-1}.

7.2.1 Simulation of line profiles

The α Sco system is seen approximately edge-on ($i = 90°$, see Sect. 3) and is assumed to have a circular orbit ($e \sim 0$). Therefore, the results from the hydrodynamic simulations at any time step can be used as input to ZETAUR. The ZETAUR program takes the parameters ω (see Sect. 7.1), the Julian date (JD) of the periastron passage T_0, the JD of the observation T_{obs}, and the time difference ΔT_{ecl}

[1]Program ID 076.D-0690(A)

between the periastron passage and the total eclipse as input. The spectra I used in this analysis were presented by Baade & Reimers (2007) and were recorded on September 17, 1995 at about 5 am (UTC), i. e. at $T_{\rm obs} \sim$ JD 2 449 977.7.

The remaining parameters have to be adjusted so that the configuration of α Sco in the AMRCART data is read out by ZETAUR in a way that corresponds to the configuration that was seen at the time of observation, i. e. with the B star at a position angle of $\delta = 23^\circ$ behind the supergiant. Based on the position of the B star ($x_{\rm B}$, $y_{\rm B}$, $z_{\rm B}$) given in the AMRCART coordinate system, the parameters are calculated as described in Sect. A.4.

Baade & Reimers (2007) found up to four absorption components in various lines of different ions and created a model based on concentric shells at different distances to the supergiant to explain these distinct components. They suggested episodic events of high mass-loss rates, each one followed by a period of low mass loss, which would indeed result in distinct components in the observed absorption lines. Now, the results of the hydrodynamic simulations presented in Sect. 6.2 show that the influence of the hot H II region around the B star constitutes a natural cause of density structures inside the common envelope, which may explain at least in part the observed absorption components.

As an example, Fig. 7.1 shows the simulated profile of the Zn II UV mult. 1 2062.660 Å absorption line, based on a simulation with $\dot{M} = 10^{-6}\ M_\odot\,{\rm yr}^{-1}$ and $v_\infty = 20\ {\rm km\,s}^{-1}$, along with a plot of the same line for the case of an undisturbed, spherically expanding wind with the same parameters. Obviously, the absorption component at $\sim -20\ {\rm km\,s}^{-1}$ is present in both lines, but the absorption profile that is based on the hydrodynamic simulation exhibits a more complex structure, which finds expression in three additional minima, namely at ~ -29, -7, and $3\ {\rm km\,s}^{-1}$. The radial velocities are measured relative to the center of mass of the system. Thermal broadening is included by applying a constant temperature of 5000 K, which is approximately the mean temperature inside the H II region. Microturbulence is not included in the calculation of the line profiles, so that all additional effects that influence the line profile are of hydrodynamic origin.

The distinct components seen in the absorption line presented in Fig. 7.1 are related to features of the density and velocity distribution along the line of sight to the B star. Figure 7.2 shows the number density of Zn^+ and the radial velocity as a function of distance to the B star along the line of sight. The absorption line profile resulting from these data is shown in Fig. 7.1. One important result is that the velocity is no longer a monotonic function of distance to the B star when hydrodynamic effects are included, but there is a broad minimum around ~ 4000 AU.

Figure 7.3 shows the dependence of the Zn II UV mult. 1 2062.660 Å and Cr II UV mult. 1 2062.236 Å lines on the mass-loss rate. While the position of the component at $\sim -20\ {\rm km\,s}^{-1}$ remains nearly unchanged, the position of the other strong component, which is associated to the increased density at the boundary of the H II region, shifts to lower velocities as the mass-loss rate decreases and the H II region becomes more extended. There is also a component at $\sim -29\ {\rm km\,s}^{-1}$, which is very weak in the Zn II line. The profiles of the Cr II line show that this

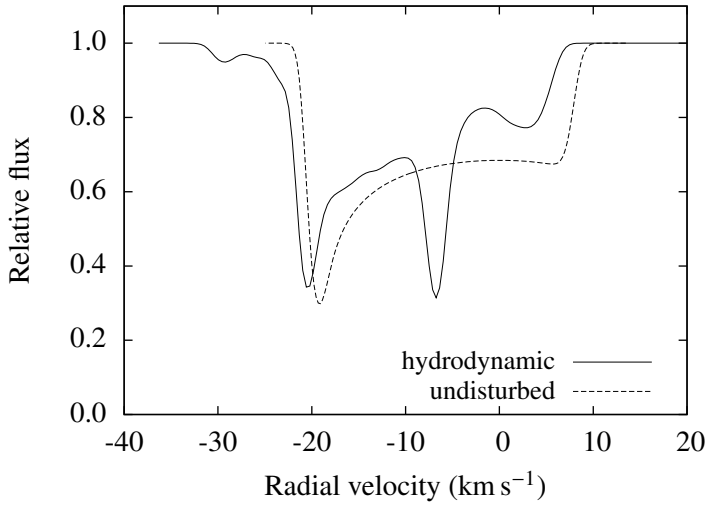

Figure 7.1: Calculations of the Zn II UV mult. 1 2062.660 Å absorption line based on a hydrodynamic simulation including ionization with $\dot{M} = 10^{-6}\ M_\odot\,\mathrm{yr}^{-1}$ and $v_\infty = 20\ \mathrm{km\,s}^{-1}$, and on an undisturbed, spherically expanding wind.

component is considerably stronger at lower mass-loss rates. This is because the wake of the H II region is more extended when the overall density is lower, so that the minimum of the radial velocity, shown in Fig. 7.2 for $\dot{M} = 10^{-6}\ M_\odot\,\mathrm{yr}^{-1}$, becomes broader and a higher number of particles along the line of sight move with velocities larger than the terminal wind velocity v_∞. That is, the larger extent of the volume containing gas at high velocities, which produces the absorption component at $-29\ \mathrm{km\,s}^{-1}$, overcompensates the effect of the decreased density.

In the Cr II line there is practically no absorption at positive velocities, because most chromium is doubly ionized throughout the H II region. In contrast, Zn^{++} is only present close to the B star, which is partly due to the different ionization potentials of Zn^+ (144 893 cm^{-1}) and Cr^+ (132 966 cm^{-1}). The relative abundances of H^+, Cr^+, and Zn^+ are shown in Fig. 7.4 as a function of distance to the B star along the line of sight.

The absorption component at the terminal wind velocity $v_\infty \sim -20\ \mathrm{km\,s}^{-1}$ in the profile based on an undisturbed, spherically symmetric wind, shown in Fig. 7.1 for the Zn II line, is also present in the absorption profiles including dynamic effects (see Figs. 7.1 and 7.3), and its position appears to be independent of the mass-loss rate. In the absorption profiles including dynamics the position of this component only slightly differs from v_∞, which is due to the orbital motion of the supergiant (its orbital velocity[2] is $v_\mathrm{M} \sim 1.7\ \mathrm{km\,s}^{-1}$) and the details of the velocity distribution along the line of sight (cf. Fig. 7.2). Note that for a given mass-loss rate the strong absorption components in the Zn II line are located at the same positions in the Cr II line.

[2]The simulations were carried out with an orbital period $P \sim 2562$ yrs, and stellar masses $M_\mathrm{A} = 18\ M_\odot$ and $M_\mathrm{B} = 6.6\ M_\odot$, which yields a semi-major axis of $D \sim 544$ AU.

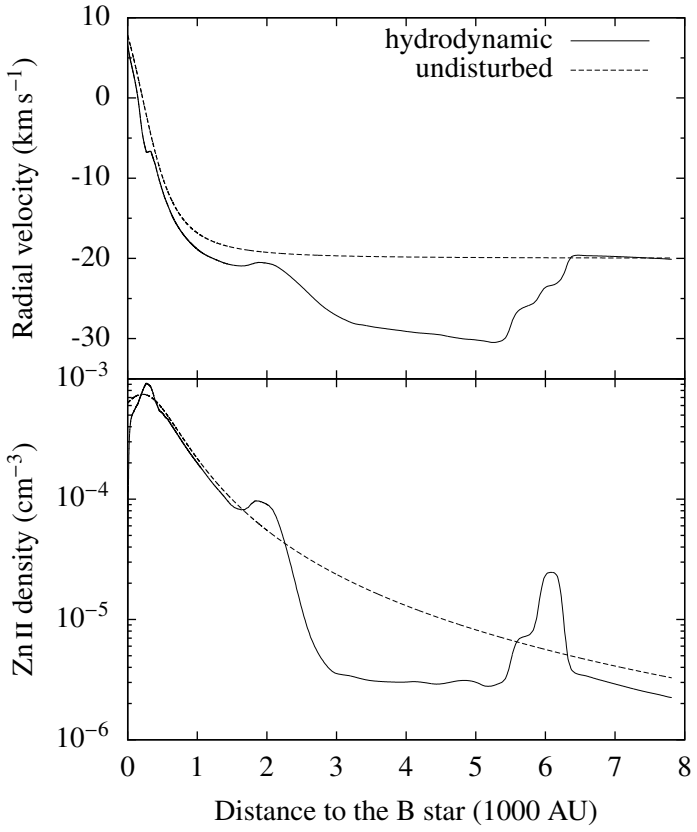

Figure 7.2: Radial velocity and Zn II number density along the line of sight to the B star, based on a hydrodynamic simulation and on an undisturbed, spherically expanding wind. These data correspond to the absorption line profiles shown in Fig. 7.1 ($\dot{M}$ = $10^{-6}\ M_\odot\,\mathrm{yr}^{-1}$, $v_\infty = 20\ \mathrm{km\,s}^{-1}$).

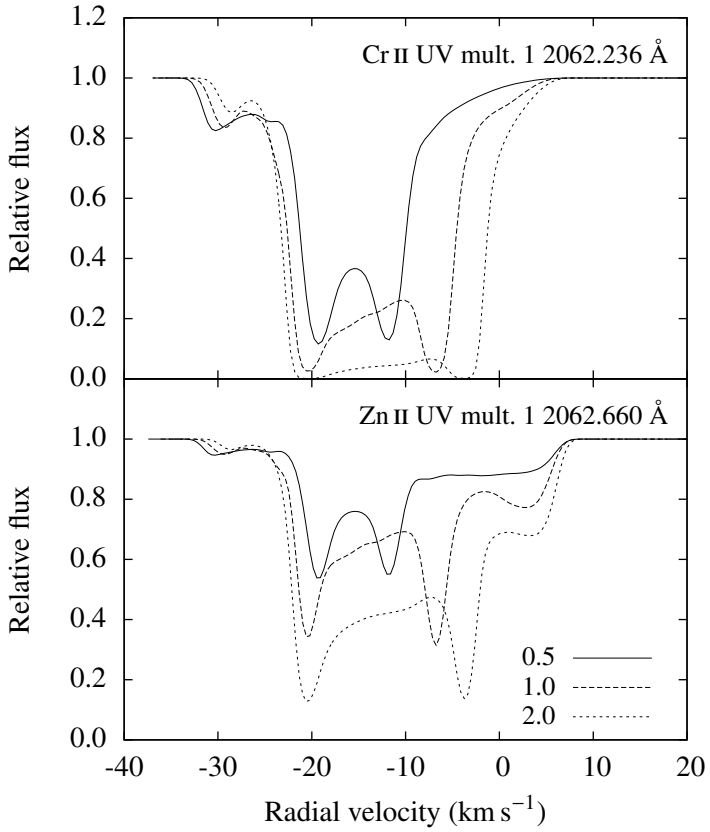

Figure 7.3: Absorption profiles of the Zn II UV mult. 1 2062.660 Å and Cr II UV mult. 1 2062.236 Å lines for different mass-loss rates (v_∞ = 20 km s^{-1}). The mass-loss rates are given at the bottom right of the figure in units of 10^{-6} $M_\odot$ yr^{-1}.

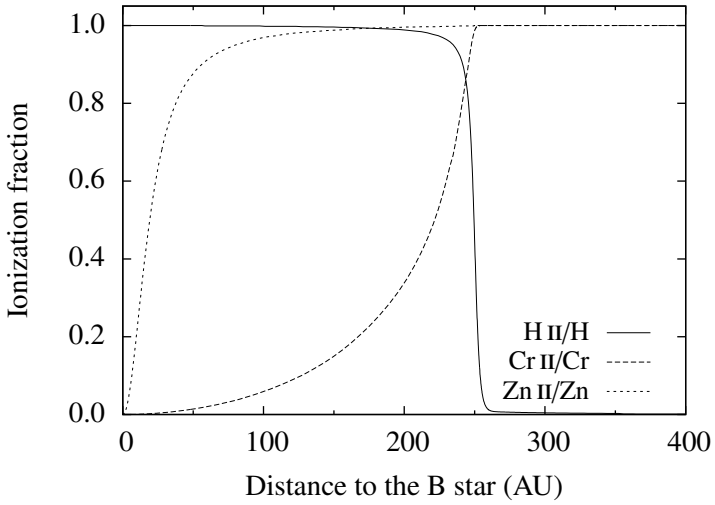

Figure 7.4: Ionization fractions of different ions as a function of distance to the B star along the line of sight. The data are derived from a simulation using $\dot{M} = 10^{-6}\ M_{\odot}\,\mathrm{yr}^{-1}$ and $v_{\infty} = 20\ \mathrm{km\,s}^{-1}$.

7.2.2 Calibration of the wavelength scale using UVES spectra

The positions of the observed absorption components in the GHRS spectra are slightly different in every line (Baade & Reimers 2007), which is due to the relatively large error of the wavelength calibration. The data were recorded using the Large Science Aperture of GHRS, which results in a maximum error of $\sim 4.5\ \mathrm{km\,s}^{-1}$ (Heap et al. 1995). The wavelength calibration of the spectra observed with VLT/UVES is much more accurate. It amounts to $\gtrsim 120\ \mathrm{m\,s}^{-1}$ (D'Odorico et al. 2000). The panel at the bottom left of Fig. 7.5 shows the Ca II mult. 1 (H and K) lines. There are three components in both lines, at −21.0, −13.6, and $-5.9\ \mathrm{km\,s}^{-1}$, respectively.

Now, supposing that the component at $-21\ \mathrm{km\,s}^{-1}$ in the Ca II lines is associated to the terminal wind velocity as suggested by the synthetic line profiles presented in the previous section, the positions of the GHRS lines can be calibrated by applying shifts that place the most blue-shifted strong component at $-21\ \mathrm{km\,s}^{-1}$, which is acceptable as long as the shifts are smaller than the maximum error of the GHRS wavelength calibration ($4.5\ \mathrm{km\,s}^{-1}$). Table 7.2 lists the shifts corresponding to the five GHRS lines presented in Fig. 7.5. The Cr II line is saturated, so that the positions of the strong absorption components are rather uncertain. Therefore, the shift determined for the Zn II line is used, which lies very close to the Cr II line. For the Fe II line the central component is used to define the shift, because the observed component near $-21\ \mathrm{km\,s}^{-1}$ is weak and not clearly pronounced.

Observed absorption lines of Ti II also show a strong absorption component at $\sim -21\ \mathrm{km\,s}^{-1}$, which may serve as an additional justification for identifying the position of this component with the terminal wind velocity. The two panels at the

Table 7.2: Velocity shifts applied to the GHRS spectra (see Fig. 7.5).

Transition	Shift ($\mathrm{km\,s^{-1}}$)
Cu II UV mult. 3 1358.773 Å	−3.2
Ni II 1393.324 Å	−4.2
Zn II UV mult. 1 2062.660 Å	−3.0
Cr II UV mult. 1 2062.236 Å	−3.0
Fe II UV mult. 1 2622.452 Å	−1.6

bottom right of Figure 7.5 show absorption line profiles of the Ti II multiplets 1 and 2.

7.2.3 Comparison to observed profiles

Figure 7.5 shows a selection of absorption lines observed with GHRS and UVES in the spectrum of α Sco B. The shapes of the line profiles produced by different ions or different energy levels of the same ion (Ti II) show a large variety. The observed absorption features depend on the excitation of fine-structure levels of the ions and the ionization of the corresponding element along the line of sight. Most of the lines exhibit three strong absorption components at the approximate positions −21, −14, and −6 $\mathrm{km\,s^{-1}}$, respectively. Some of the lines produced by the 0 $\mathrm{cm^{-1}}$ levels have an additional component at −29 $\mathrm{km\,s^{-1}}$ (Ti II 3384.730 Å, Cr II 2062.236, Zn II 2062.660 Å, and Ni II 1393.324 Å), which can be explained by the broad minimum of the radial velocity in the wake of the H II region far from the B star (see Figs. 7.3 and 7.2).

For the comparison presented in the following, a systemic velocity of $v_{\mathrm{sys}} = -1.3\ \mathrm{km\,s^{-1}}$ is added to the wavelength scale of the simulated profiles, which results from a comparison of the projected orbital velocities resulting from the adopted orbital configuration ($\delta = 23°$, $e = 0$) with the observed radial velocities. The measured radial velocity of the supergiant is $v_{r,\mathrm{M}} \sim -3\ \mathrm{km\,s^{-1}}$ (Evans 1967), and the radial velocity of the B star is $v_{r,\mathrm{B}} \sim 3\ \mathrm{km\,s^{-1}}$ (Kudritzki & Reimers 1978), which is consistent with the adopted orbital velocities of $v_{\mathrm{M}} = 1.7$ and $v_{\mathrm{B}} = 4.2\ \mathrm{km\,s^{-1}}$ if the systemic velocity is $\sim -1.3\ \mathrm{km\,s^{-1}}$.

Cr II, Cu II, Ni II, and Zn II

Figure 7.6 shows a comparison of the observed Cr II, Cu II, Ni II, and Zn II lines presented in Fig. 7.5 to theoretical profiles corresponding to a mass-loss rate of $\dot{M} = 2 \times 10^{-6}\ M_{\odot}\,\mathrm{yr^{-1}}$ and a wind velocity of $v_{\infty} = 20\ \mathrm{km\,s^{-1}}$. The simulated line profiles are convolved with a gaussian profile function with a FWHM of 3.5 $\mathrm{km\,s^{-1}}$ to account for the limited resolution of the HST/GHRS spectra.

Obviously, there are a number of differences between the simulated and the observed line profiles. First of all, there are only two strong components in the simulated profiles, whereas there are three in the observed profiles. Secondly, the

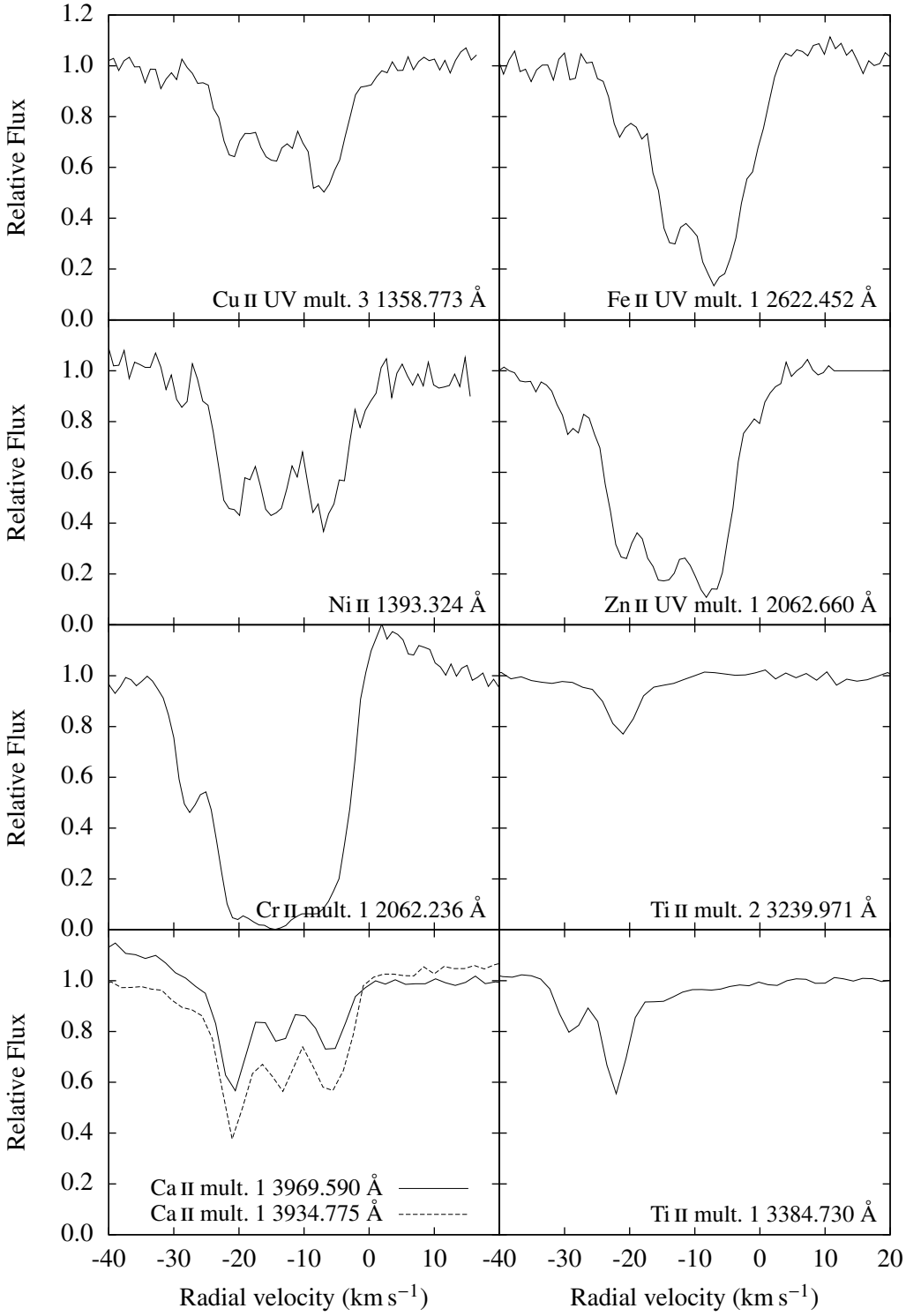

Figure 7.5: Absorption profiles observed in the spectrum of α Sco B with HST/GHRS (Cu II, Fe II, Ni II, Zn II, and Cr II lines) and VLT/UVES (Ti II and Ca II lines). The velocity scale of the GHRS lines is calibrated by applying the shifts listed in Table 7.2.

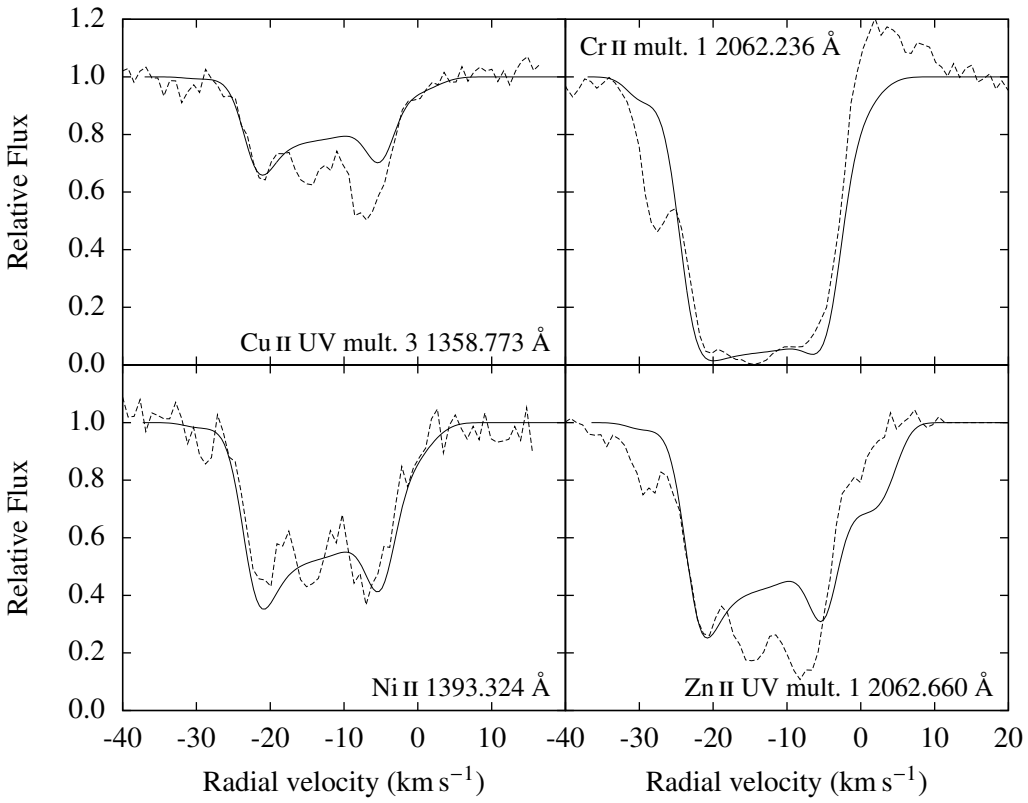

Figure 7.6: Comparison of theoretical line profiles (solid curves) corresponding to a mass-loss rate of $\dot{M} = 2 \times 10^{-6}\ M_{\odot}\,\mathrm{yr}^{-1}$ and a wind velocity of $v_{\infty} = 20\ \mathrm{km\,s}^{-1}$ with observations (dashed curves), including a velocity calibration provided by the UVES spectra (see Sect. 7.2.2) and a systemic velocity of $-1.3\ \mathrm{km\,s}^{-1}$.

observed component at -6 km s^{-1} is much stronger than predicted by the model calculations in the Zn II and Cu II lines. However, with the wavelength calibration described in the previous section the positions of the two strong components in the simulated profiles approximately match the positions of the outer two of the observed strong components. It turns out that, within the error of the wavelength calibration, the observed GHRS profiles are consistent with the assumption that the position of the most blue-shifted of the strong absorption components is at -21 km s^{-1}, as suggested by the absorption lines measured with UVES and by the theoretical lines, all of which include a strong absorption component at the position corresponding to the terminal wind velocity.

The weaker absorption component at ~ -29 km s^{-1}, which is clearly visible in the Cr II and the Zn II line, is very weak in the corresponding theoretical profiles. This may be due to the limited spatial resolution of the hydrodynamic simulations, which tends to smear out the narrow density enhancements produced by the shock front at the boundary of the H II region (cf. Sect. 6.5). The simulations predict a stronger absorption component at this position for lower mass-loss rates, especially in the Cr II line (see Fig. 7.3). This may be an indication of a time-dependent mass-loss rate, which could produce distinct absorption components corresponding to different mass-loss rates (see Sect. 9.2).

The equivalent widths of the observed profiles and the simulated profiles shown in Fig. 7.6 agree well. Moreover, the component at ~ -21 km s^{-1} of the simulated profiles gives a good fit of the observed components. The absorption in the components at -6 km s^{-1} is stronger in the observed lines, which may be due to interstellar absorption as all the lines result from transitions starting from the lowest energy levels of the ions. The theoretical absorption lines resulting from simulations using a mass-loss rate of $\dot{M} = 10^{-6}\ M_{\odot}$ yr^{-1}, as given by Reimers et al. (2008) based on a simplified model of the circumstellar shell neglecting dynamic effects, are much weaker than the observed ones. That shows the significant impact of the hydrodynamic effects, which will have to be considered in future studies of mass loss.

Differences between the observed and simulated profiles are to be expected, because the simulations do not account for a possible time dependence of the mass-loss rate. Indications of multiple shell ejection have been observed in IR images in both α Sco and α Ori (e. g. Danchi et al. 1994, see also Sect. 4.2). The additional third component in the observed lines seen in Fig. 7.6 at ~ -14 km s^{-1} could well be the result of such a discrete ejection. An additional complication of a comparison of observations with theory is the observed differential depletion (Baade & Reimers 2007). These effects may be the reason for a more complicated structure of the absorption profiles.

Fe II

The observed absorption profile of the Fe II UV mult. 1 2622.452 Å line presented in Fig. 7.5 results from the fine structure level in the ground term at 977.053 cm^{-1}, which corresponds to a total angular momentum quantum number $J = 1/2$. The

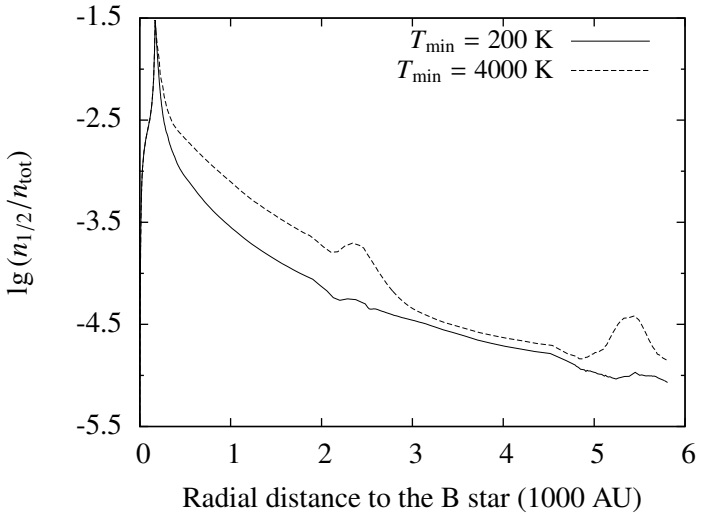

Figure 7.7: Relative population of the highest level of the a^6D term of Fe II, 977.053 cm^{-1}, as a function of distance to the B star for two different lower limits $T_{\rm min}$ of the electron temperature. $n_{1/2}$ is the density of ions in the corresponding state, and $n_{\rm tot}$ the total density of Fe^+. These data correspond to the simulation with $\dot{M} = 2 \times 10^{-6}\ M_\odot\,{\rm yr}^{-1}$ and $v_\infty = 20\ {\rm km\,s}^{-1}$.

population $n_{1/2}$ of this level cannot be reproduced by applying a constant scale factor to the total Fe^+ density, as would be expected if the levels were populated according to their statistical weights.

The Cloudy code, which was used to calculate the ionization and temperature structure inside the circumstellar shell, comprises a detailed model atom developed by Verner et al. (1999) incorporating the lowest 371 levels of the Fe^+ ion. When this model atom is used for the calculation of the excitation and ionization of iron along the line of sight to the B star, it also yields the population of the level at 977.053 cm^{-1}, which is the highest level in the ground term. Figure 7.7 shows the result for a mass-loss rate of $2 \times 10^{-6}\ M_\odot\,{\rm yr}^{-1}$. It turns out that the relative population of the level is very low inside the cool neutral wind. The population of the Fe II energy levels depends on the electron temperature, which determines the rate of collisions. The temperature inside the H II region is $\sim$ 5000 K, but the temperature in the H I region is not exactly known. Figure 7.7 shows the population of the 977.053 cm^{-1} level relative to the total Fe^+ abundance for two different lower limits $T_{\rm min}$ of the electron temperature, i. e. the temperature was not allowed to fall below the lower limit in these simulations.

Obviously, the relative population of the 977.053 cm^{-1} level steeply decreases after a peak at the boundary of the H II region. Figure 7.8 shows the absorption line profiles corresponding to the two cases displayed in Fig. 7.7 along with the observed absorption profile, which is shifted by $-1.6\ {\rm km\,s}^{-1}$ according to Table 7.2 (cf. the previous section). The slope of the right flank of the strong absorption components in the theoretical profiles does not exactly match the observed one, because there is a considerable amount of reemission, which is not included in the

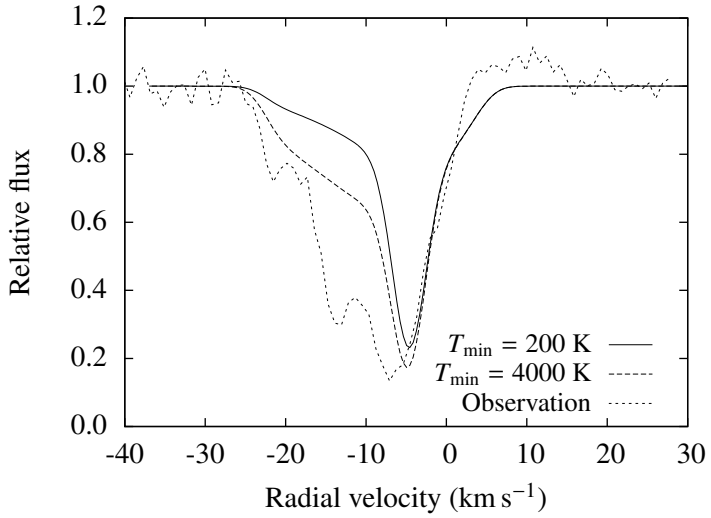

Figure 7.8: Observed and theoretical absorption profiles of the Fe II UV mult. 1 2622.452 Å line for $\dot{M} = 2 \times 10^{-6}\ M_\odot\,\mathrm{yr}^{-1}$ and $v_\infty = 20\ \mathrm{km\,s}^{-1}$. For the theoretical profiles, two different lower limits of the electron temperature were used in the corresponding plasma simulations (cf. Fig. 7.7).

calculation of the theoretical line profiles. The decrease of the absorption towards lower velocities qualitatively matches the observation, although the slope is much too steep in the theoretical profiles. The absence of the middle absorption component in the theoretical profiles is not surprising since it is absent in all theoretical profiles (cf. Sect. 7.2.1).

The assumption that the neutral part of the wind has a temperature of 4000 K is probably not realistic, and even in this case the predicted absorption is too weak in the outer parts of the envelope. A value of $T \lesssim 1000$ K in the H I region is more realistic. Apparently the calculation of the level population with Cloudy does not give correct results, maybe because of an underestimation of the rates of collisional or radiative processes that populate the level that is responsible for the absorption, or because of advection effects, which are not included in the simulations (see Sect. 6.4). In the plasma simulations, the gas is assumed to be at rest with respect to the B star, which may introduce another uncertainty in the calculation of the populations of fine-structure levels, as the velocity field may have considerable effects on the continuum pumping rates. However, the strength of the absorption component at $\sim -5\ \mathrm{km\,s}^{-1}$ approximately matches the strength of the observed component, so that the mass-loss rate of $2 \times 10^{-6}\ M_\odot\,\mathrm{yr}^{-1}$, which is consistent with the observed profiles of the lines of other ions (cf. Fig. 7.6), can be confirmed.

The results presented in this section suggest that the weakness of the absorption components of this Fe II line at -14 and $-21\ \mathrm{km\,s}^{-1}$ is due to the relatively high energy difference between the lowest level and the fine-structure level corresponding to the transition. Apparently the mechanisms that excite Fe II to higher fine-structure levels are not efficient in the outer parts of the circumstellar enve-

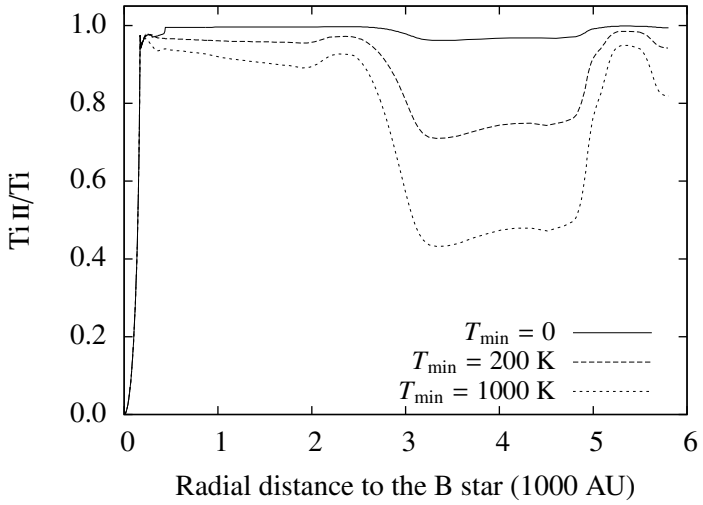

Figure 7.9: Ti^+ fraction along the line of sight for different lower limits applied to the temperature in a simulation using $\dot{M} = 2 \times 10^{-6}\ M_\odot\,\mathrm{yr}^{-1}$ and $v_\infty = 20\ \mathrm{km\,s}^{-1}$.

lope, i. e. at low densities, far from the B star and its H II region.

Ca II and Ti II

The number densities of Ca^+ and Ti^+ along the line of sight cannot be reproduced in the framework of the present model. In the case of Ti^+, the plasma simulations yield a density that is much too high and density gradients that are too steep to reproduce the observed absorption profiles. The ionization of Ti^+ is complicated because its ionization potential (13.576 eV) is close to the Lyman edge. Simulations show that the ionization of Ti^+ sensitively depends on the local temperature in the circumstellar shell (Fig. 7.9). The absence of the absorption components at -6 and $-14\ \mathrm{km\,s}^{-1}$ in the observed line profiles of Ti II shown in Fig. 7.5 suggests that most titanium is at least doubly ionized up to a large distance to the B star, i. e. even far outside the H II region. However, the absence of these components may also be due to dust depletion.

In the case of Ca^+, the predicted number density is much too low. In the whole circumstellar envelope Ca^{++} appears to be the dominant stage of ionization of calcium, and Ca^+ shows a very complex dependence on the varying conditions along the line of sight (see Fig. 7.10). Thus, the Ca II lines are inappropriate for mass-loss diagnostics. However, the observed profiles of Ca II H and K can be roughly reproduced by assuming that the distribution of the Ca II/Ca fraction behaves as the fraction H I/H of neutral hydrogen and by applying a scale factor of 2×10^{-3}. Figure 7.11 shows the result for Ca II H.

The simplified treatment of the corresponding model atoms may be the reason for the discrepancy between theory and observation in the case of Ca II and Ti II. The Cloudy code treats Ca^+ as a five-level atom, which includes the fine-structure levels of only the lowest three terms (4s, 3d, and 4p) with the corresponding transi-

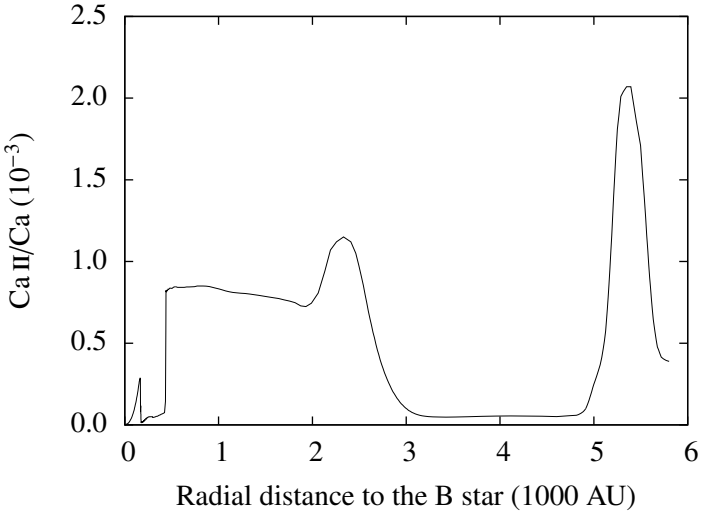

Figure 7.10: Ca^+ fraction along the line of sight for a simulation using $\dot{M} = 2 \times 10^{-6}$ $M_\odot\,\mathrm{yr}^{-1}$and $v_\infty = 20\,\mathrm{km\,s}^{-1}$.

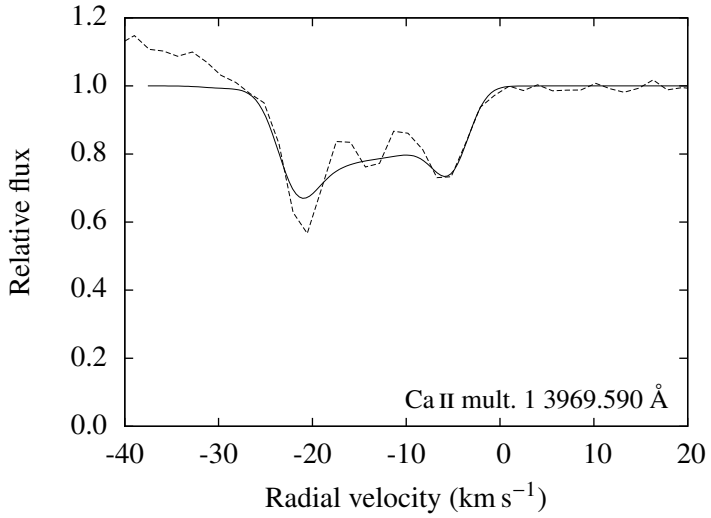

Figure 7.11: Observed (dashed curve) and theoretical (solid curve) absorption profile of Ca II H for a simulation using $\dot{M} = 2 \times 10^{-6}\ M_\odot\,\mathrm{yr}^{-1}$ and $v_\infty = 20\,\mathrm{km\,s}^{-1}$. For the calculation of the theoretical profile, it was assumed that the fractional Ca^+ density is given by $Ca^+/Ca = 2 \times 10^{-3} H^0/H$.

tions (multiplets 1, 2, and 1F). Ti^+ is treated in the framework of the scandium-like isoelectronic sequence as a five-level atom without resolving any fine-structure components, including only the terms a^4F, z^4G^o, z^4F^o, and the terms $^4F^o$ and $^4D^o$ of the configuration $3d(^2D)4s4p(^3P^o)$. Thus, for Ti^+, populations of individual fine-structure levels are not calculated. Moreover, only transitions to the ground term of Ti II are included in the simulation. The depletion of titanium due to dust formation is probably the most significant effect producing deviations from the observed data (cf. Baade & Reimers 2007).

Chapter 8

Optical line emission from the Antares nebula

The Antares emission nebula, which is associated to the H II region around α Sco B, is seen in the optical in Hα and various other emission lines, last described in detail by Reimers et al. (2008). The simulations presented above will be compared to observations of the Hα emission in Sect. 8.1. The most prominent emission lines result from forbidden transitions in Fe II, which will be used to compare observations to the simulations in Sect. 8.2. The observations were performed with UVES at the VLT using a long slit perpendicular to the line connecting the two stars, and yielded a scan of the emission nebula with a step size of $\sim 0\farcs5$, starting $0\farcs9$ west of the supergiant (see Fig. 8.1). The dimensions of the slit are $0\farcs4 \times 10''$ in the blue and $0\farcs4 \times 12''$ in the red arm (for details about the design of UVES see Dekker et al. 2000).

8.1 Hα emission

The plasma simulations described in Sect. 5.2 show that the strongest Hα emission in the Antares nebula emerges near the B star, where most hydrogen is ionized. This is shown for a cut parallel to the plane of the orbit in Fig. 8.2. Outside the H II region the emission is much weaker and follows the total density (Fig. 8.3). I performed simulations with the program Cloudy (see Sect. 5.2.1) to predict the Hα emission. Figure 8.4 shows the corresponding transitions. Cloudy combines the transitions that belong to the same pair of terms and treats Hα as a result of three transitions. See Table 8.1 for details.

8.1.1 Dependence of Hα production on spectral features of the B star

In an H II region, Hα is naturally produced by recombination of electrons and protons. Another important mechanism is pumping by Lyman line photons from the source of radiation, so that the presence of Lyman absorption or emission lines

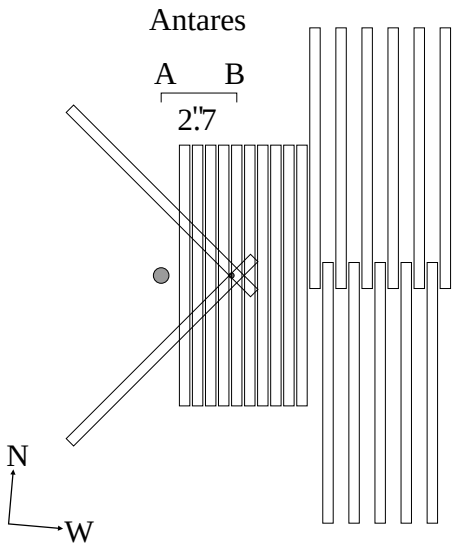

Figure 8.1: Slit positions used for the observations of the Antares nebula. The rectangles indicate the position and size of the slit in the blue arm relative to the α Sco system as it is seen in the sky. This is Fig. 1 in Reimers et al. (2008).

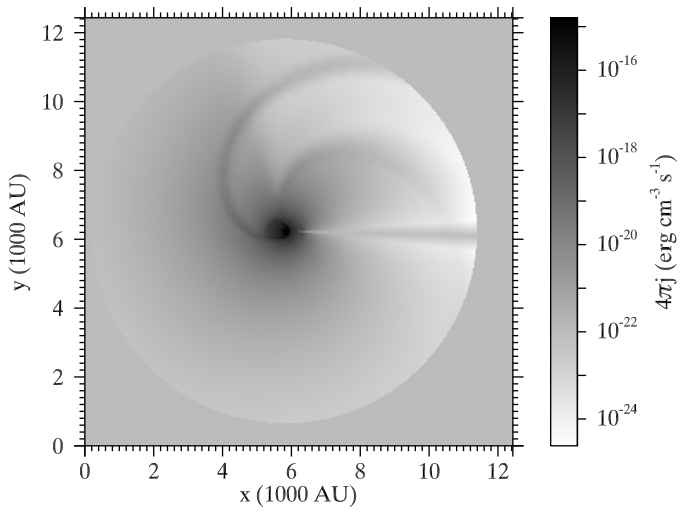

Figure 8.2: Hα emission resulting from a simulation with $\dot{M} = 2 \times 10^{-6}\ M_\odot\,\mathrm{yr}^{-1}$ and $v_\infty = 20\ \mathrm{km\,s}^{-1}$. The emission coefficient is calculated up to a distance of ~ 5694 AU from the B star, which is located at ($x \sim 5818$, $y \sim 6226$) AU. The horizontal structure that ranges from the center of the image to the boundary is an artifact produced by the interpolation routine (cf. Sect. 5.2.3). The corresponding density distribution is shown in Fig. 8.3

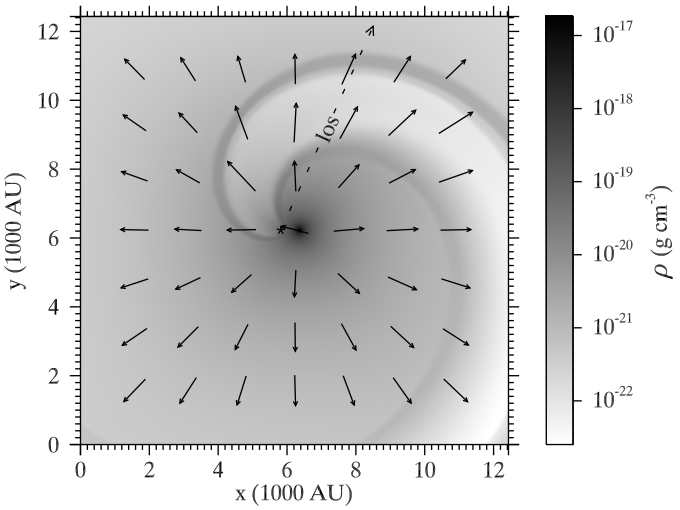

Figure 8.3: Density and velocity distribution resulting from a simulation with $\dot{M} = 2 \times 10^{-6}\ M_\odot\,\mathrm{yr}^{-1}$ and $v_\infty = 20\ \mathrm{km\,s}^{-1}$. The dotted arrow indicates the line of sight to the B star, whose position is marked by the asterisk.

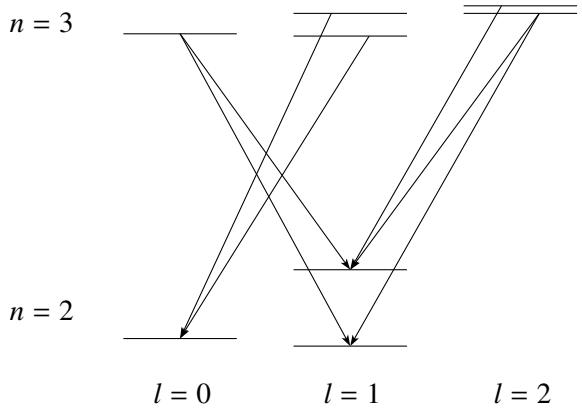

Figure 8.4: Transitions involved in the production of Hα emission. The differences in height of the fine structure levels corresponding to the same principal quantum number n are proportional to their energy differences (NIST Atomic Spectra Database, Ralchenko et al. 2011). l is the azimuthal quantum number.

Table 8.1: Transitions producing Hα emission.

Transition	λ (Å)	A_{ul} (10^5 s^{-1})	g_l	g_u	A'_{ul}(10^5 s^{-1})	g'_l	g'_u
$2p\,^2P^o_{1/2} - 3s\,^2S_{1/2}$	6562.752	21.046	2	2	63.101	6	2
$2p\,^2P^o_{3/2} - 3s\,^2S_{1/2}$	6562.909	42.097	4	2			
$2s\,^2S_{1/2} - 3p\,^2P^o_{3/2}$	6562.725	224.48	2	4	224.352	2	6
$2s\,^2S_{1/2} - 3p\,^2P^o_{1/2}$	6562.772	224.49	2	2			
$2p\,^2P^o_{1/2} - 3d\,^2D_{3/2}$	6562.710	538.77	2	4	646.109	6	10
$2p\,^2P^o_{1/2} - 3d\,^2D_{5/2}$	6562.852	646.51	4	6			
$2p\,^2P^o_{3/2} - 3d\,^2D_{3/2}$	6562.867	107.75	4	4			

Notes. The values in the first five columns were taken from the NIST Atomic Spectra Database (Ralchenko et al. 2011). λ is the wavelength in air, A_{ul} the Einstein coefficient for spontaneous emission, and g_l and g_u the statistical weights of the lower and upper level, respectively. The parameters in the last three columns, which are marked with a prime, give the values used by Cloudy to calculate Hα emission. They represent the 3s – 2p, 3p – 2s, and 3d – 2p transitions, respectively.

in the spectrum of the source of radiation affects the production of Hα photons. The B-star atmospheres presented in the TLUSTY grid (Lanz & Hubeny 2007) show strong absorption in the Lyman lines. As the Antares H II region is optically thin in Hα, the observed emission is solely determined by the population of the upper levels (cf. Fig. 8.4) and the transition rates, which are represented by the corresponding Einstein coefficients for spontaneous emission (see Table 8.1).

Figure 8.5 shows a B star spectrum for $\log g = 3.9$, $T_{\rm eff} = 18\,200$ K, and $R_B = 4.8\,R_\odot$ in the range of the Lyman lines. The dependence of the Hα emission on the intensity of the Lyman lines is illustrated in Fig. 8.6, which shows the rate of Hα emission per unit volume, $4\pi j$, as a function of radial distance to the B star in the direction towards the supergiant, for three different scale factors applied to the incident Lyman-line fluxes. j is the total frequency-integrated Hα emission coefficient for isotropic emission, i. e.

$$j = \sum_{l_u=0}^{2} \frac{h\nu_{3l_u\to 2l_l}}{4\pi} \int_0^\infty n_{3l_u} A'_{3l_u\to 2l_l} \phi_{3l_u\to 2l_l}(\nu)\,\mathrm{d}\nu, \tag{8.1}$$

where h is Planck's constant, $\nu_{3l_u\to 2l_l}$ the frequency of the transition, l_u is the azimuthal quantum number of the upper level, n_{3l_u} the number density of hydrogen atoms in the upper state ($n = 3$, $l = l_u$), $A'_{3l_u\to 2l_l}$ the Einstein coefficient for spontaneous emission from level ($n = 3$, $l = l_u$) to level ($n = 2$, $l = l_l$), and $\phi_{3l_u\to 2l_l}(\nu)$ the profile function of the Hα transition. The values of $A'_{3l_u\to 2l_l}$ are given in Table 8.1, and the levels involved in the calculation are illustrated in Fig. 8.4.

The spectral features at wavelengths redward of the Lyman lines have only minor effects on the Hα emission. As a proof, I substituted the spectrum of the B star in the range $\nu < 2.303$ PHz with the spectrum of a blackbody at $T = 18\,200$ K (see Fig. 8.7) and calculated the Hα emission again. Figure 8.8 shows

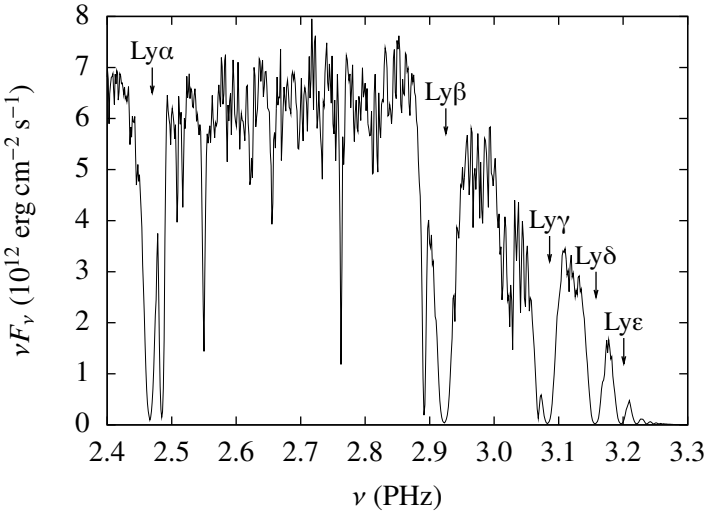

Figure 8.5: Lyman lines in the synthetic B-star spectrum used for the Cloudy simulations.

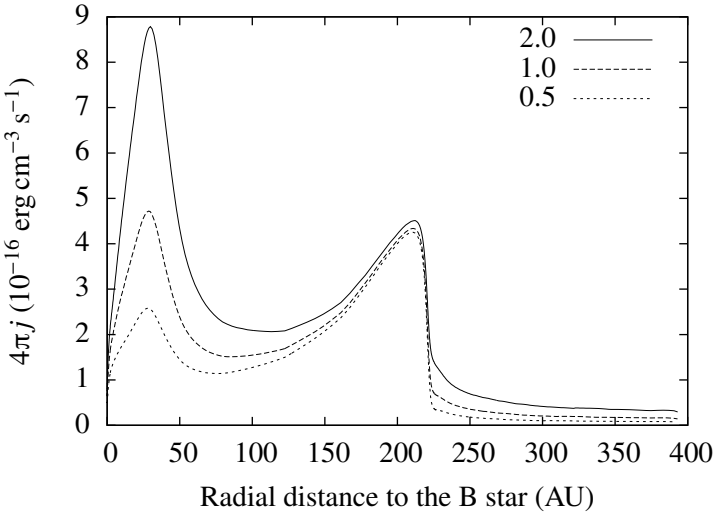

Figure 8.6: Hα emission calculated with Cloudy for three Lyman line pumping-rates in the direction towards the supergiant ($\theta = \pi/2,\ \phi = 0$). The numbers in the legend give the scale factors applied to the pumping rate that results from the Lyman-line flux in the spectrum of the B star.

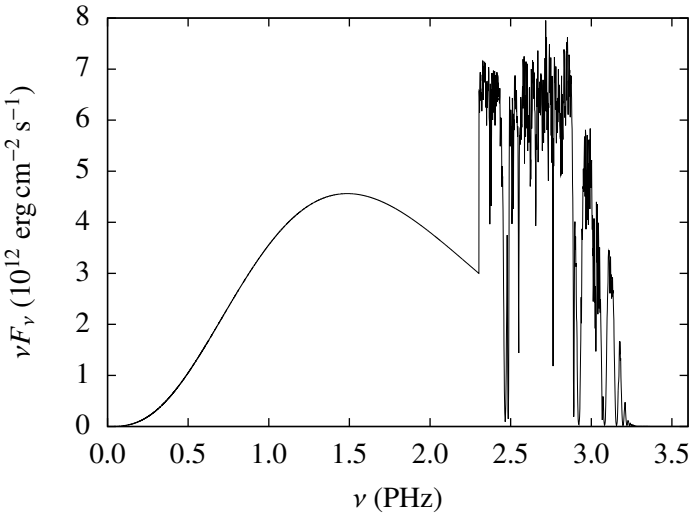

Figure 8.7: Substitution of the B-star spectrum with a blackbody spectrum for $\nu < 2.303$ PHz as a test for the sensitivity of Hα emission on spectral features redward of the Lyman lines.

the result together with the emission corresponding to the Cloudy simulation with the original B star spectrum for comparison. The effect of the spectral features in this frequency range on the resulting temperature distribution and ionization structure is negligible.

The sensitivity of the Hα emission produced in the H II region to changes of the input flux in the range of the Lyman lines requires a high-resolution input spectrum in the Cloudy simulations. For the calculations presented in this chapter I used a resolution of $\Delta\nu/\nu = 5 \times 10^{-4}$ (cf. Fig. 8.5).

8.1.2 Estimating the extent of the Hα emission

The spatial extent of the H II region is determined by the mass-loss rate of the supergiant and the Lyman-continuum flux of the B star, and can be measured by observing the spatial extent of the Hα emission from the Antares nebula (cf. Reimers et al. 2008). Figure 8.9 shows the Hα intensity distribution at 3.″4 from the supergiant, measured on the projected line connecting the two stars (see Fig. 8.1). The shape and extent of the observed and theoretical Hα intensity distributions agree, but the center of the theoretical distribution is shifted to higher velocities with respect to the observed distribution. This is probably due to the uncertainties in the geometry of the system and can be explained by an overestimation of the position angle of the line connecting the two stars relative to the plane of the sky ($\sin i = 1$ is only a rough estimate, and due to the long period it will be difficult to improve on this).

The intensity in Fig. 8.9 is given as a function of velocity. For a comparison of the spatial extent of the observed and theoretical emission, it is easier to compare the frequency-integrated emission as a function of position along the slit. The

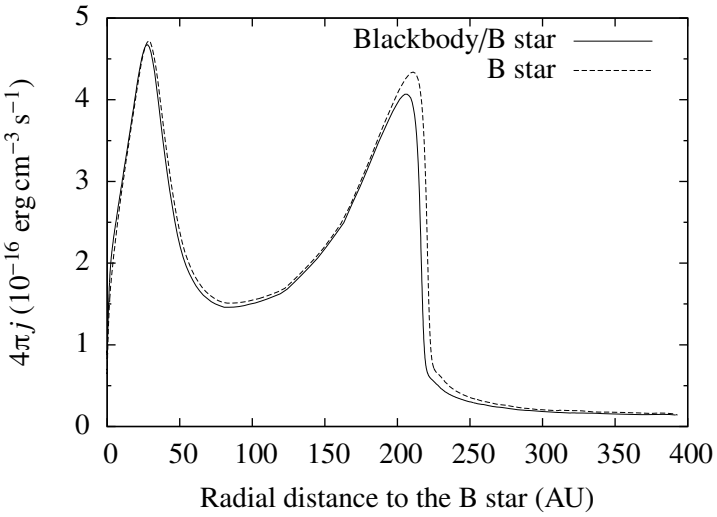

Figure 8.8: Hα emission resulting from simulations with the combined blackbody/B-star spectrum (Fig. 8.7) and the original B-star spectrum (Fig. 5.2).

integration of the theoretical data reads, assuming pure emission,

$$I = \int_{s_{\min}}^{s_{\max}} j(s)\mathrm{d}s, \tag{8.2}$$

where j is the emission coefficient defined in Eq. 8.1, and the range of the coordinate s, measured along the line of sight, is the same as in Eq. 8.3 (Sect. 8.2). The results are shown for different slit positions in Fig. 8.10 for a simulation with $\dot{M} = 2 \times 10^{-6}\ M_\odot\,\mathrm{yr}^{-1}$ and $v_\infty = 20\ \mathrm{km\,s}^{-1}$, along with the corresponding observational data. In this simulation, the slit skims only the outermost part of the H II region at the slit positions 1.″9 and 5.″4. Therefore, the theoretical data at these slit positions should be interpreted with care, because outside the H II region the Hα production is dominated by line pumping effects, which may not be well reproduced with the simplified approach used by Cloudy for the radiative transfer (see Sect. 5.2.1). The central minimum in the observations corresponding to 2.″4 is probably due to an artifact related to the data reduction. At the other slit positions, the simulated and observed distributions agree well in shape and extent.

Figures 8.11 and 8.12 present the same data for simulations with $\dot{M} = 10^{-6}\ M_\odot\,\mathrm{yr}^{-1}$, and $\dot{M} = 5 \times 10^{-7}\ M_\odot\,\mathrm{yr}^{-1}$, respectively, both using a terminal wind velocity of $v_\infty = 20\ \mathrm{km\,s}^{-1}$. These simulations obviously yield Hα distributions that are considerably broader than the observed ones. Besides, at positions far from the supergiant, i. e. at $\geq$ 4.″9 for the simulation with $\dot{M} = 10^{-6}\ M_\odot\,\mathrm{yr}^{-1}$ and at $\geq$ 3.″4 for $\dot{M} = 5 \times 10^{-7}\ M_\odot\,\mathrm{yr}^{-1}$, the theoretical Hα distributions do not reach zero at the ends of the slit. This is due to the larger extension of the H II region in these simulations, which is a result of the lower mass-loss rates. Figure 8.13 shows the distribution of the Hα emission coefficient j resulting from the simulation corresponding to $\dot{M} = 10^{-6}\ M_\odot\,\mathrm{yr}^{-1}$. The length of the slit used for the observations is 12″, which is equivalent to $\sim$ 2220 AU at the distance of α Sco,

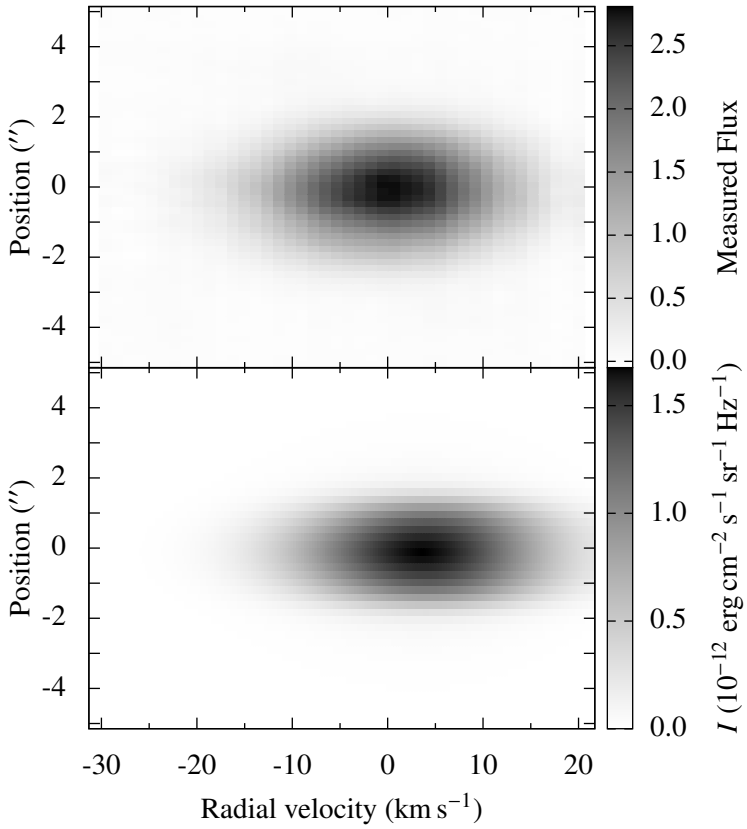

Figure 8.9: Hα emission at 3.″4 from the supergiant. The top panel shows the observed flux in arbitrary units, the bottom panel the intensity derived from a simulation with $\dot{M} = 2 \times 10^{-6}\ M_\odot\,\mathrm{yr}^{-1}$ and $v_\infty = 20\ \mathrm{km\,s}^{-1}$. The ordinate indicates the position along the slit. The theoretical intensity distribution is calculated as described in Sect. 8.2. As can be seen, cf. also Fig. 8.10, the theorical distribution is slightly too narrow, which means that the adopted mass-loss rate is here slightly too large. For the apparent velocity shift, see text p. 73.

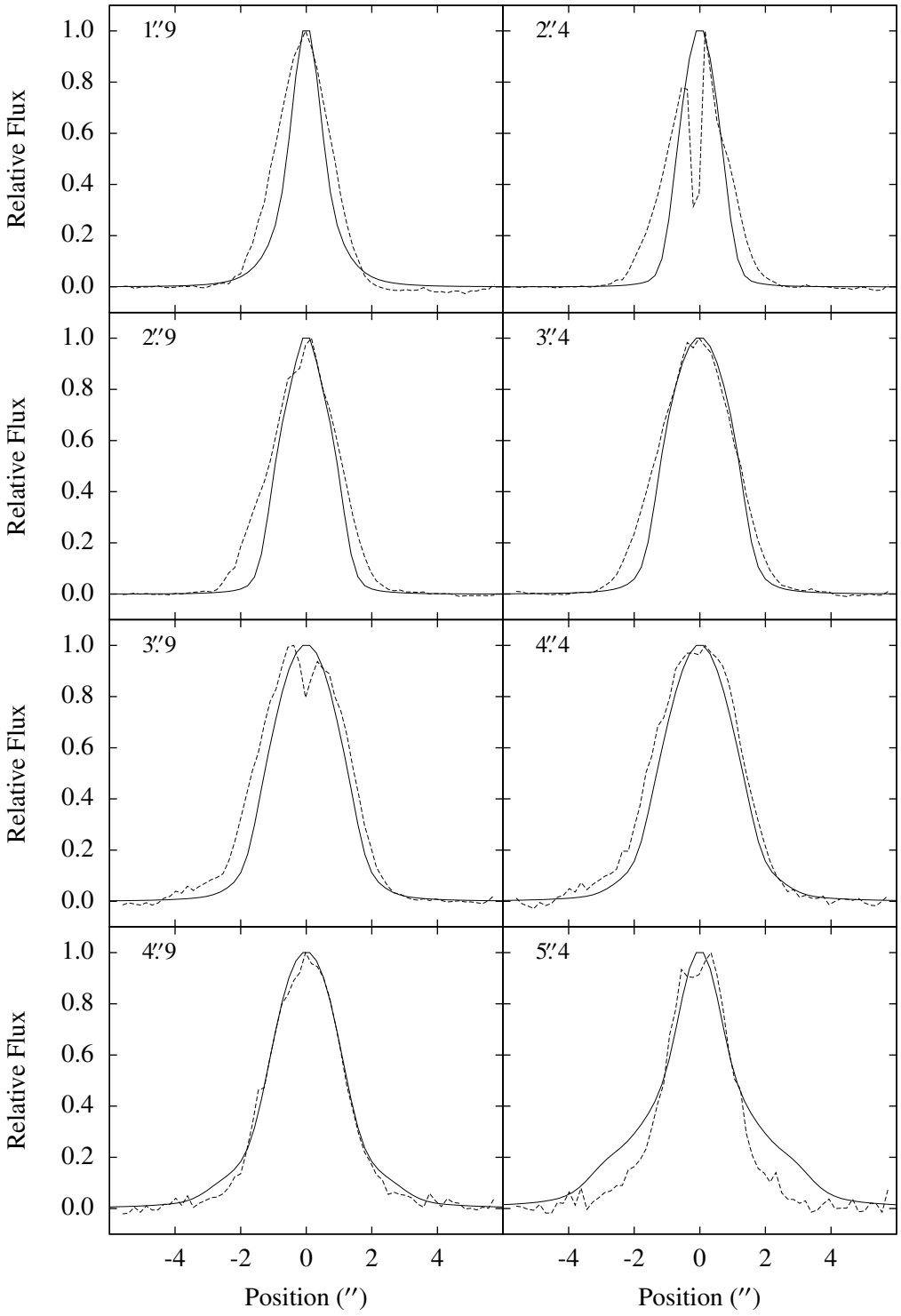

Figure 8.10: Frequency-integrated Hα flux as a function of position along the slit for a simulation with $\dot{M} = 2 \times 10^{-6}\ M_{\odot}\,\mathrm{yr}^{-1}$ and $v_{\infty} = 20\ \mathrm{km\,s}^{-1}$ (solid lines), and the corresponding observations (dashed lines).

and which only just covers the whole region of high emission located in the center of Fig. 8.13, which is associated to the H II region. In the case of a mass-loss rate of $\dot{M} = 5 \times 10^{-7}\ M_\odot\,\mathrm{yr}^{-1}$, this region is even more extended.

At 2.″4 and 2.″9, the Hα profiles corresponding to a mass-loss rate of 10^{-6} $M_\odot\,\mathrm{yr}^{-1}$(Fig. 8.11) look more similar to the observed data than the profiles corresponding to $2 \times 10^{-6}\ M_\odot\,\mathrm{yr}^{-1}$ (Fig. 8.10), while the observed data at the other slit positions further away from the supergiant are better reproduced by the model with the higher mass-loss rate. This may be due to the mass-loss rate being time-dependent.

8.2 [Fe II] emission

The most prominent emission lines seen in the Antares nebula are the forbidden iron lines that result from transitions corresponding to the multiplets a^6D – a^6S (4287.40 Å, 4359.34 Å, 4413.78 Å), a^6D – b^4F (4416.27 Å), and a^4F – b^4F (4814.55 Å). The spatial and spectral distribution of the line at 4814.55 Å (multiplet F20) was presented in detail by Reimers et al. (2008).

The data obtained with the Cloudy calculations (see Sect. 5.2) can be used to compare the results of the simulations to the observed data. Cloudy gives information about the emission coefficient j (Eq. 8.4) as a function of position. Together with the velocity distribution from the hydrodynamic simulations, these data can be used to calculate theoretical intensity distributions of emission lines. For the treatment of Fe II, Cloudy provides a large model atom developed by Verner et al. (1999). It includes the 371 lowest levels of the Fe^+ ion, i. e., up to 93 487.65 cm^{-1}.

Figure 8.14 shows the spatial distribution of the emission coefficient resulting from the Cloudy calculations for a mass-loss rate of $\dot{M} = 2{\times}10^{-6} M_\odot\,\mathrm{yr}^{-1}$. Outside the H II region, towards low densities and temperatures, Cloudy appears to have problems with the Fe II model atom. The emission coefficient does not change with density anymore when a certain arbitrary distance is reached. Therefore, $T_\mathrm{min} = 200$ K was used as a lower limit for the temperature (cf. the analysis of the Fe II absorption line in Sect. 7.2.3). A comparison of Fig. 8.14 to Fig. 8.3 shows that the [Fe II] emission is roughly correlated with the density, which is to be expected if collisions are the dominant excitation mechanism. In the region around ($x = 1600$ AU, $y = 450$ AU), i. e. in the proximity of the B star, the emission is high despite the relatively lower density. In this region, pumping effects and recombination are apparently more important for the excitation of the line.

Assuming pure emission, the emergent intensity is given by the integral

$$I_v(v) = \int_{s_\mathrm{min}}^{s_\mathrm{max}} j(s)\Phi[v_r(s) - v]\mathrm{d}s, \tag{8.3}$$

where s ranges from ~ -3730 AU to $\sim +3730$ AU along the line of sight, and the zero point lies in the plane defined by the line connecting the two stars and the

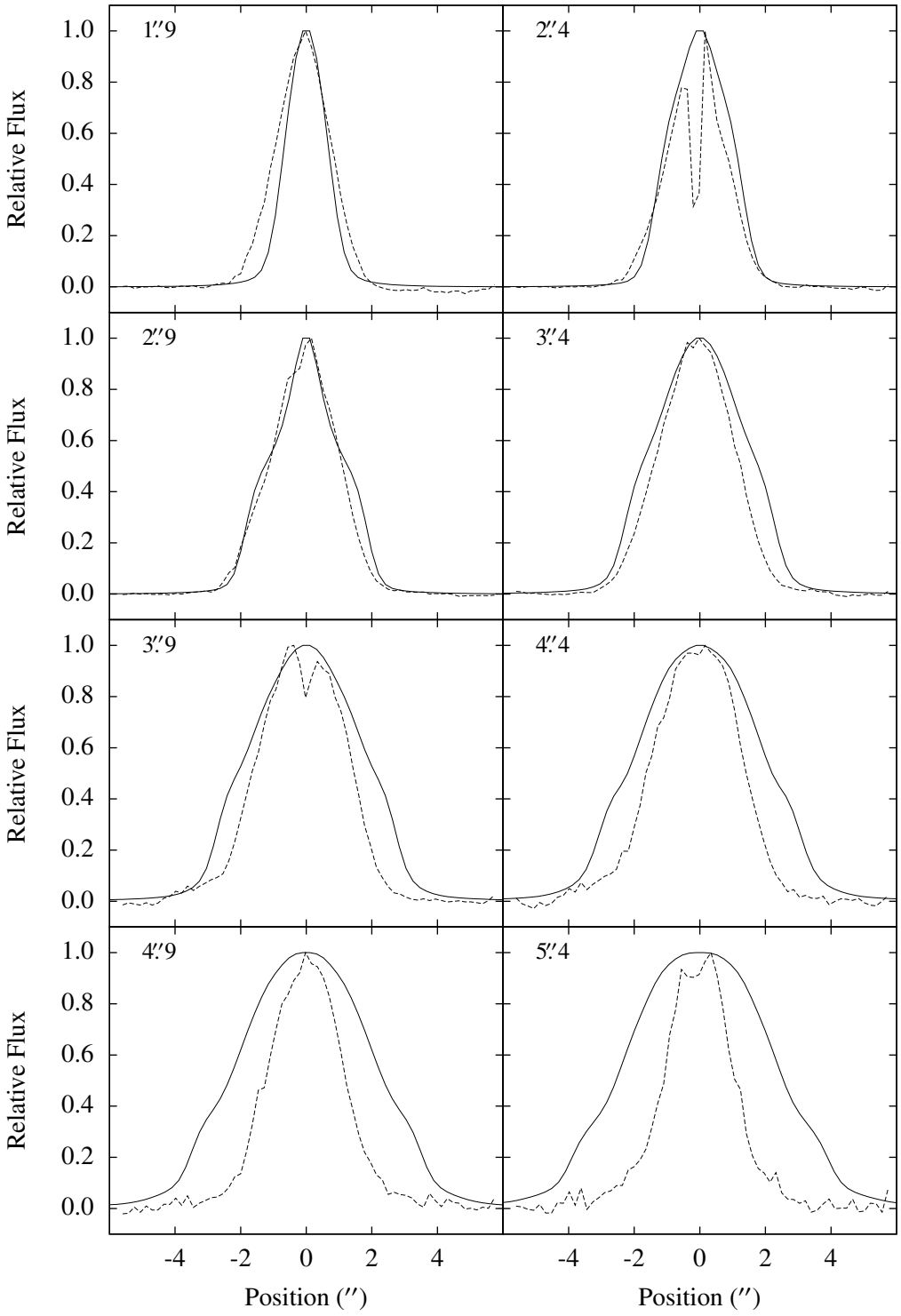

Figure 8.11: Frequency-integrated Hα flux as a function of position along the slit for a simulation with $\dot{M} = 10^{-6}\ M_{\odot}\,\mathrm{yr}^{-1}$ and $v_{\infty} = 20\ \mathrm{km\,s}^{-1}$. The solid lines are derived from the simulations, the dashed lines show the corresponding observations.

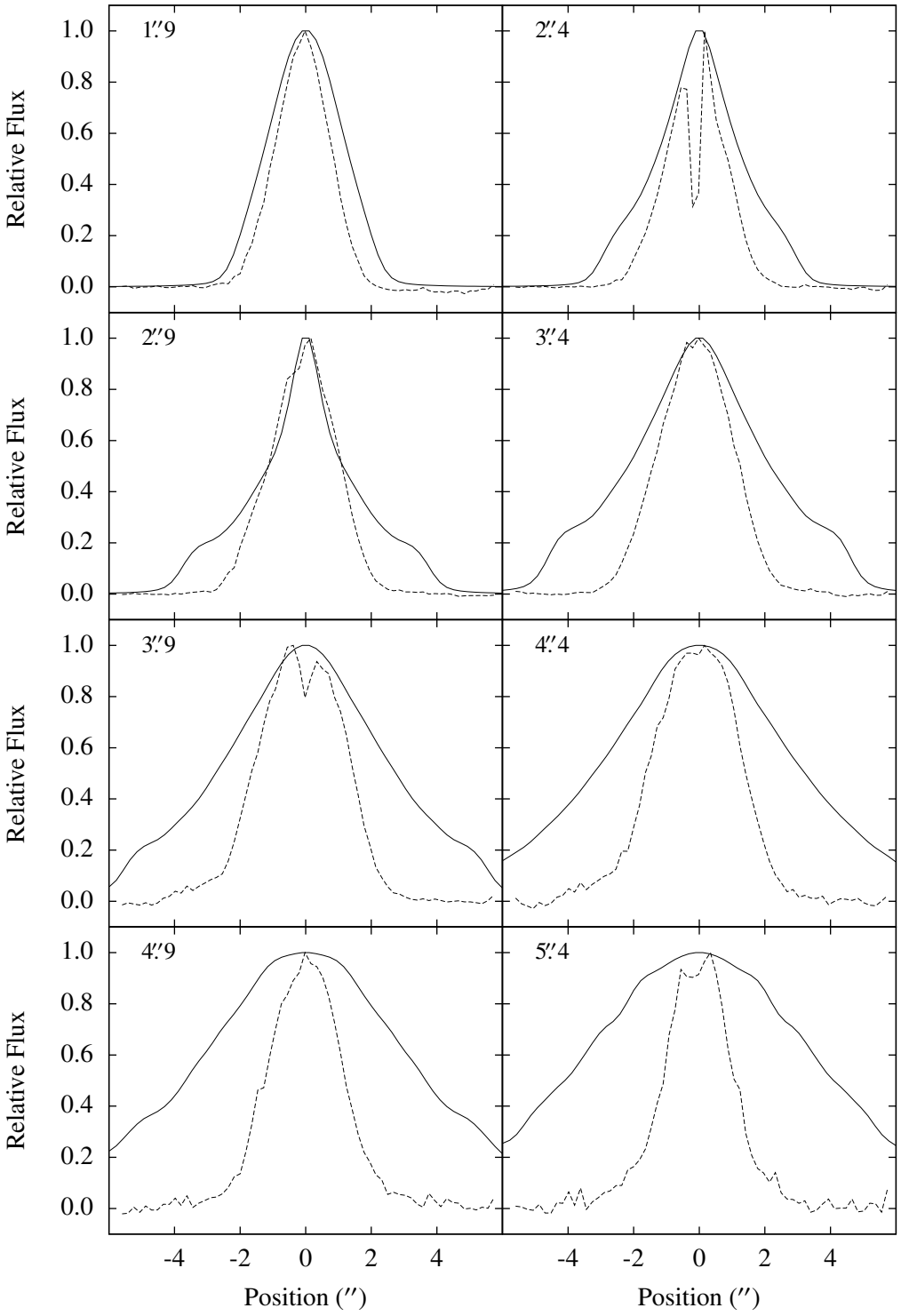

Figure 8.12: Frequency-integrated Hα flux as a function of position along the slit for a simulation with $\dot{M} = 5 \times 10^{-7}\ M_{\odot}\,\mathrm{yr}^{-1}$ and $v_{\infty} = 20\ \mathrm{km\,s}^{-1}$. The solid lines are derived from the simulations, the dashed lines show the corresponding observations.

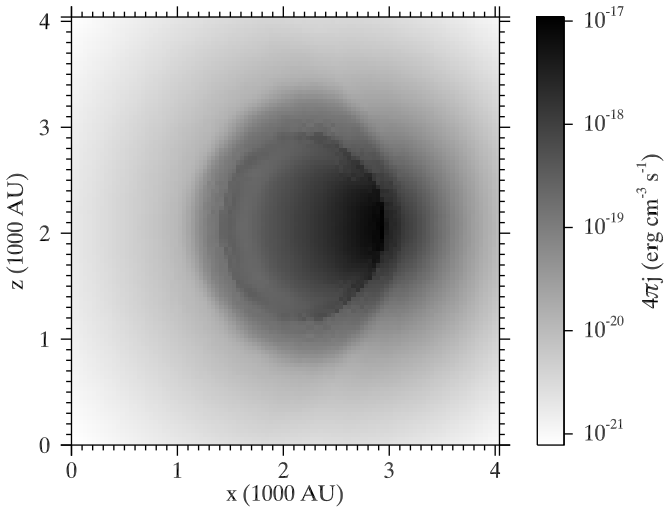

Figure 8.13: Distribution of Hα emission resulting from a simulation with $\dot{M} = 10^{-6}\ M_\odot\,\mathrm{yr}^{-1}$ and $v_\infty = 20\ \mathrm{km\,s}^{-1}$. This is a cut through the H II region, approximately parallel to the line connecting the two stars in the region where the H II region is most extended. The ordinate corresponds to the direction perpendicular to the plane of the orbit.

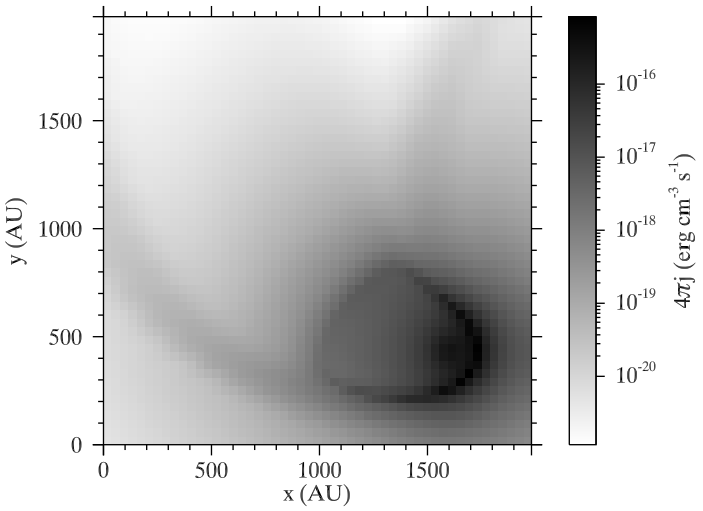

Figure 8.14: Distribution of the emission coefficient corresponding to the [Fe II] UV mult. 20F 4814.55 Å line resulting from a simulation with $\dot{M} = 2 \times 10^{-6}\ M_\odot\,\mathrm{yr}^{-1}$ and $v_\infty = 20\ \mathrm{km\,s}^{-1}$. This is a cut parallel to the plane of the orbit with the B star at ($x \sim 1600$, $y \sim 450$)

direction perpendicular to the orbit, so that the H II region is fully included. j is the emission coefficient for isotropic emission,

$$j = \frac{h\nu_{\rm lu} n_{\rm u} A_{\rm lu}}{4\pi} \int_0^\infty \phi(\nu) {\rm d}\nu, \tag{8.4}$$

resulting from the frequency $\nu_{\rm lu}$ of the transition, the number density $n_{\rm u}$ of ions in the upper state, the transition probability $A_{\rm lu}$, and the profile function $\phi(\nu)$. h is Planck's constant, $v_r(s)$ the radial velocity at s, and Φ a gaussian profile that introduces thermal broadening,

$$\Phi(v) = \frac{1}{\Delta v_{\rm D}\sqrt{\pi}} \exp\left[-\frac{v^2}{(\Delta v_{\rm D})^2}\right], \tag{8.5}$$

where the Doppler width $\Delta v_{\rm D}$ (see Eq. 7.2) is defined by pure thermal broadening with a temperature of 5000 K. Microturbulent broadening is not included, so that the hydrodynamic effects can be clearly identified. I_v is the intensity per unit radial velocity, and the intensity per unit frequency reads $I_\nu = \lambda_0 I_v$, where λ_0 is the rest wavelength of the transition.

For a comparison with the observations as presented in Fig. 8.9 for Hα, the spectral resolution of UVES and the seeing have to be considered. An analysis of the lines of the wavelength calibration lamp yields an average FWHM of 3.5 km s^{-1} in the vicinity of 4814.55 Å, in the range from 4789 to 4832 Å. I adopted this value for the spectral resolution of the UVES spectra. The seeing during the observations was $\sim$ 0.″6. Therefore, the theoretical intensity distributions are convolved with a gaussian profile of FWHM = 3.5 km s^{-1} along the frequency coordinate and with another gaussian corresponding to the seeing in the direction of the spatial coordinate along the slit. A systemic velocity of -1.3 km s^{-1} is added to the theoretical velocity scale (cf. Sect. 7.2.3).

As an example, Fig. 8.15 shows the distribution of the [Fe II] mult. 20F 4814.55 Å intensity at 3.″4 both for the observed and the simulated data. Obviously, the simulations do not yield a realistic picture of the [Fe II] emission for that slit position. The simulations suggest a circular structure around a central maximum at $\sim$ 5 km s^{-1}, while the maximum flux in the observed data is concentrated in a more compact structure, which is approximately circular but open to the bottom, between $\sim$ 0 and $\sim$ 8 km s^{-1} as measured at the center of the slit. The overall extent of the observed emission approximately agrees with the theoretical distribution and is consistent with the extent of the Hα emission in both the velocity and the spatial coordinate.

At 2.″4, between the two stars, the theoretical data look more similar to the observations, as shown in Fig. 8.16. Here, the theoretical data suggest a compact structure between -3.5 and 16 km s^{-1} with maximum emission at the edges. This is consistent with the observed flux distribution, which includes a horizontal structure near the center of the slit that is probably an artifact caused by the reduction procedure. The theoretical flux distribution is apparently red-shifted with respect to the observed distribution, which is also seen in the Hα distribution shown in Fig. 8.9.

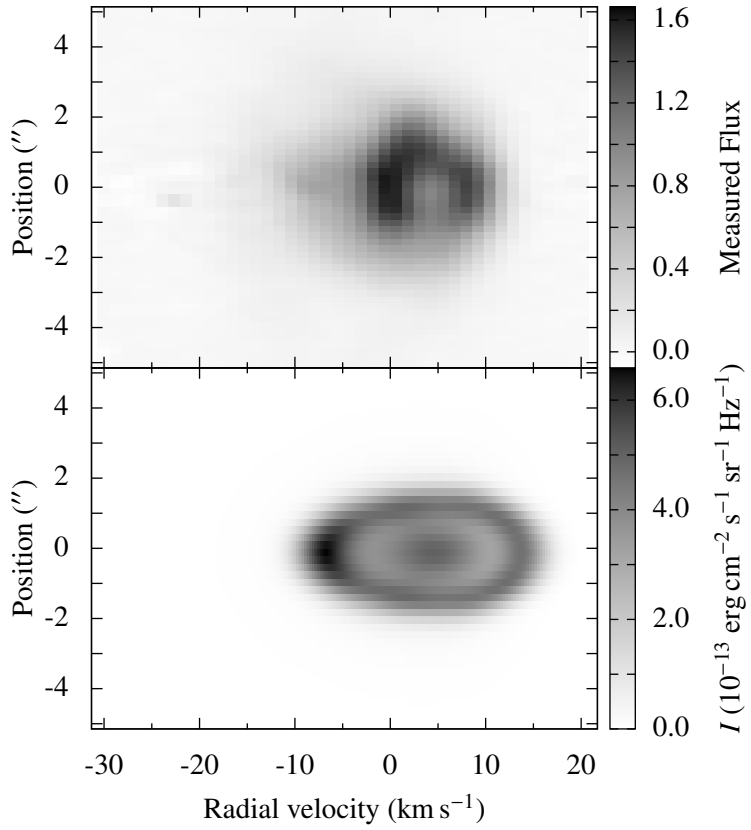

Figure 8.15: [Fe II] mult. 20F 4814.55 Å emission at 3.″4 from the supergiant. The top panel shows the observed flux in arbitrary units, the bottom panel the intensity derived from a simulation with $\dot{M} = 2 \times 10^{-6}\ M_\odot\,\mathrm{yr}^{-1}$ and $v_\infty = 20\,\mathrm{km\,s}^{-1}$. The ordinate indicates the position along the slit.

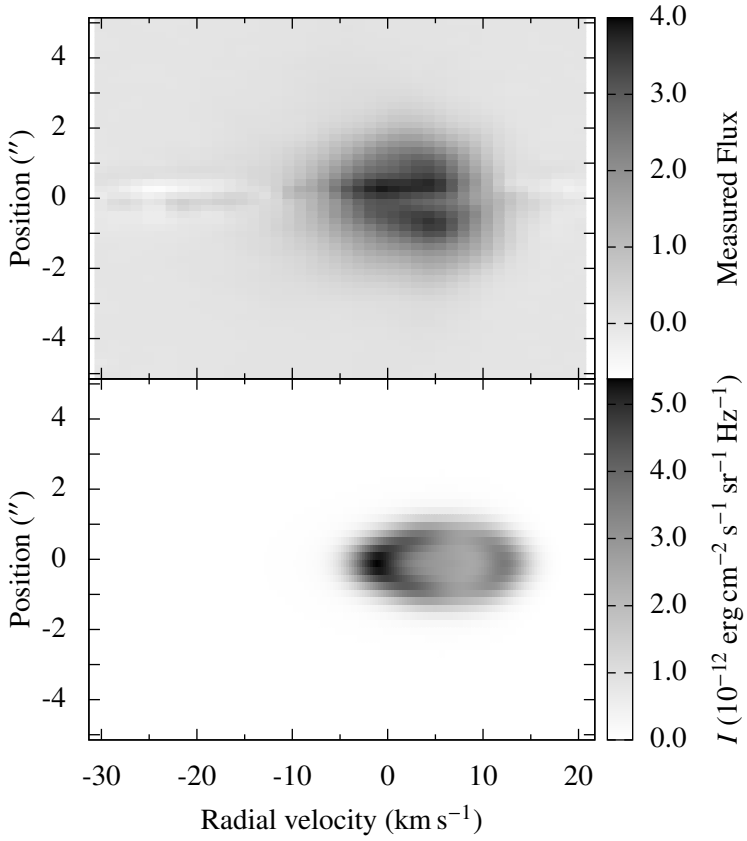

Figure 8.16: [Fe II] mult. 20F 4814.55 Å emission at 2.″4 from the supergiant. The top panel shows the observed flux in arbitrary units, the bottom panel the intensity derived from a simulation with $\dot{M} = 2 \times 10^{-6}\ M_\odot\,\mathrm{yr}^{-1}$ and $v_\infty = 20\,\mathrm{km\,s}^{-1}$. The ordinate indicates the position along the slit.

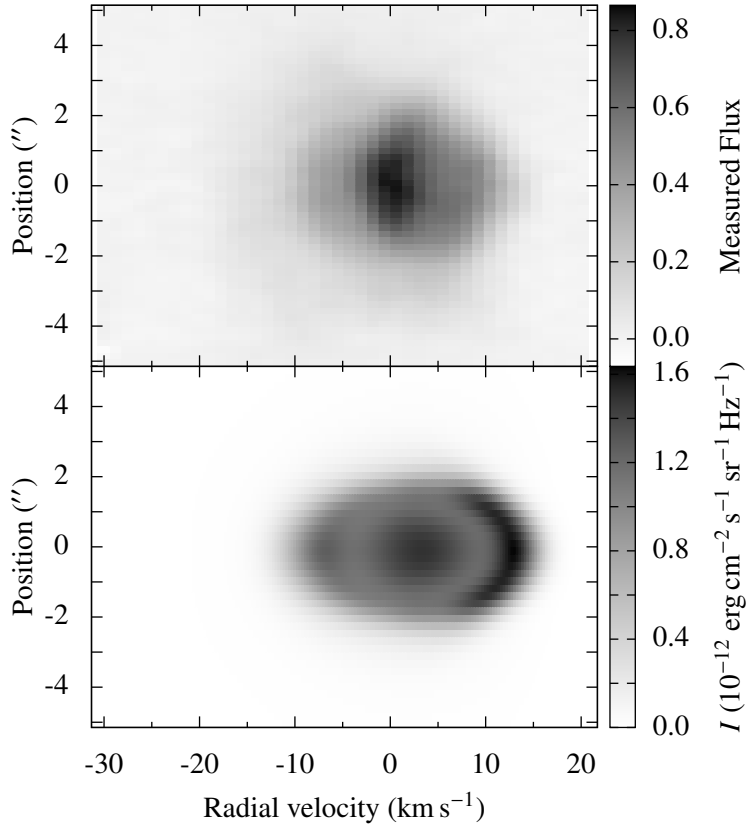

Figure 8.17: [Fe II] mult. 20F 4814.55 Å emission at 4.″4 from the supergiant. The top panel shows the observed flux in arbitrary units, the bottom panel the intensity derived from a simulation with $\dot{M} = 2 \times 10^{-6}\ M_\odot\ \mathrm{yr}^{-1}$ and $v_\infty = 20\ \mathrm{km\,s}^{-1}$. The ordinate indicates the position along the slit.

Figure 8.17 shows observed and theoretical flux distributions for the slit position at 4.″4. The ring-like structure in the simulated distribution, which is caused by the high-density boundaries of the H II region and is much more pronounced at positive velocities, is not seen in the observations, but both data sets exhibit a central maximum. A comparison to the data presented in Fig. 8.15 leads to the supposition that the central maximum in the theoretical flux distribution at 3.″4 is associated to the maximum in the observed data near 0 km s^{-1}.

The discrepancies between the observed and theoretical [Fe II] emission could be due to an inadequate treatment of the Fe^+ ion in the Cloudy code. Possible mechanisms that excite forbidden [Fe II] lines are collisions, continuum pumping, and recombination. The theoretical correlation between [Fe II] emission and density that is suggested by Fig. 8.14 is apparently not correct under the physical conditions in the Antares nebula. The emission may also be influenced by advection effects, which may be significant especially at the western boundary of the H II region (see Sect. 6.4), towards the open side of the wake. An alternative

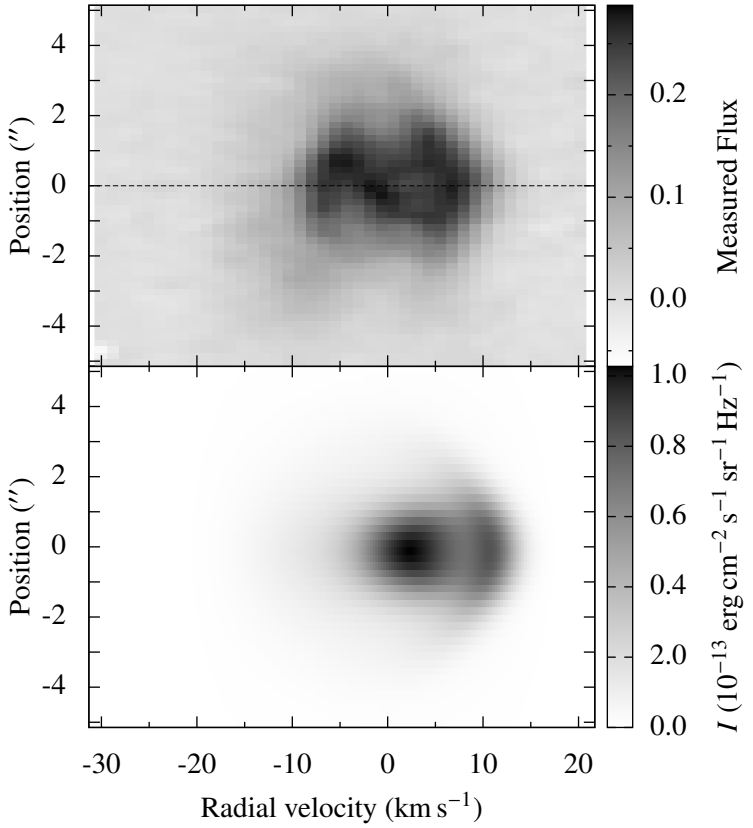

Figure 8.18: [Fe II] mult. 20F 4814.55 Å emission at 5.″4 from the supergiant. The top panel shows the observed flux in arbitrary units, the bottom panel the intensity derived from a simulation with $\dot{M} = 2 \times 10^{-6}\ M_\odot\ \mathrm{yr}^{-1}$ and $v_\infty = 20\ \mathrm{km\,s}^{-1}$. The ordinate indicates the position along the slit. Obviously, there is more emission from the upper (northern) half in the observed flux distribution.

explanation would be that due to dust depletion in the high density boundaries of the structure, a large fraction of Fe is not available for Fe II emission. This effect seems to increase with distance to the B star.

A common feature of the observed forbidden and allowed Fe^+ emission is an asymmetry with respect to the center of the slit, which is clearly visible e. g. at 5.″4 from the supergiant (Fig. 8.18). Apparently, there is more emission from the northern than from the southern half (see also Fig. 8.15). This is another indication of density structures that are not included in the model, which is symmetric with respect to the plane of the orbit. A deviation of the inclination from 90° would also cause such an asymmetry. However, the Hα flux distributions do not show any significant asymmetries.

Chapter 9

Discussion & Conclusions

9.1 The mass-loss rate

The hydrodynamic simulations presented in Sect. 6.2 show that the hot H II region that is moving with the B star through the circumstellar envelope of α Sco produces strong deviations from spherical symmetry in the density and velocity distributions. The theoretical absorption line profiles derived from these simulations (Sect. 7.2.1) exhibit a pronounced multi-component structure comparable to the observed line profiles presented in Fig. 7.5. The best match between theoretical and observed line profiles is achieved with a mass-loss rate of $\dot{M} = 2 \times 10^{-6}\ M_{\odot}\,\mathrm{yr}^{-1}$ and a wind velocity of $v_{\infty} = 20\ \mathrm{km\,s}^{-1}$ (Sect. 7.2.3). This value of the mass-loss rate is twice as high as the rate derived by Reimers et al. (2008), which was based on a spherically symmetric model of the circumstellar shell. This discrepancy is due to the decreased density in the wake of the H II region (see e. g. Fig. 8.3).

The range of values of $\dot{M}$ and v_{∞} that is covered by the simulations is rather small, owing to the limitations imposed by the large amount of computing time that the hydro code requires. As the AMRCART code is not adapted to modern parallel computing clusters, the hydrodynamic simulations were carried out on a single CPU core, while only the photoionization/radiative-transfer calculations were executed in parallel. A finer grid in $\dot{M}$ and v_{∞} would improve the accuracy of the resulting mass-loss rate, and it might be instructive to calculate models with different semi-major axes and position angles to account for the uncertainties in the orbital parameters (see next section). However, the theoretical data presented in this work and the available observations agree fairly well, and the remaining systematic errors are probably larger than the error that is due to the coarseness of the grid of models.

An important systematic error is introduced by the observed differential dust depletion (Baade & Reimers 2007). This effect depends on the considered element and on the local conditions in the circumstellar shell. It results in the observed absorption profiles being weaker than predicted for a given mass-loss rate. In contrast, interstellar absorption can make the absorption components near

0 km s^{-1} stronger than predicted by the model, which is probably responsible for the discrepancies in the Zn II 2062.660 Å and Cu II 1358.773 Å lines (Fig. 7.6). According to Snow et al. (1987) and Cardelli (1984), dust depletion is of minor importance for zinc, which means that the mass-loss rate can best be determined by use of the Zn II absorption lines.

In the present approach, the radiative transfer is treated in a simplified manner with the escape probability formalism (see Sect. 5.2.1). This is probably the major source of error in the calculation of the [Fe II] line emission, and the exact solution of the scattering problem would probably resolve some of the apparent discrepancies between the theoretical predictions and the observations. Moreover, some of the circumstellar absorption lines in the spectrum of α Sco B, e. g. Cr II 2062.236 Å, have P Cyg-type profiles, which cannot be reproduced with a pure absorption model. For a calculation of the reemission that is superposed in these lines on the absorption profile, exact radiative transfer simulations have to be included in the model.

A number of empirical mass-loss rates of ζ Aur systems were determined on the basis of spherically symmetric density and velocity distributions according to Eqs. 2.3 and 2.4 (see e. g. Che et al. 1983; Baade et al. 1996a). Some of these systems, e. g. ζ Aur and 31 Cyg, also contain H II regions, which may lead to even more severe dynamic effects than in α Sco due to the much smaller orbital periods. The current values of the mass-loss rates of these stars may have to be revised on the basis of more realistic models including dynamic processes as presented in this work for α Sco.

9.2 Asymmetries and time-dependent effects

The observations indicate an asymmetric, non-stationary character of the circumstellar shell of α Sco. The observed absorption lines exhibit an additional component at −14 km s^{-1}, which cannot be reproduced with the assumption of a constant mass-loss rate. Moreover, the integrated Hα flux (Figs. 8.10 to 8.12) also appears to indicate slightly different mass-loss rates at different distances to the B star (Sect. 8.1.2). The observations of [Fe II] emission reveal that the density distribution is not symmetric with respect to the plane of the orbit, which cannot be reproduced in the framework of the present model.

The uncertainties in the geometry of the α Sco system may partly account for the asymmetry of the observed [Fe II] emission and the shift of the theoretical emission in Hα and [Fe II] 4814.55 Å. The orbital parameters, such as the inclination, eccentricity, and the orbital velocities, are not well known because of the large orbital period (∼ 2560 yrs). Especially the radial velocity of the supergiant is hard to measure, because the observed velocity results from a superposition of pulsations and orbital motion (Smith et al. 1989).

The plasma calculations used for determining the temperature and ionization structure of the circumstellar envelope are based on the assumption that the time scales of cooling and heating are small compared to the dynamic time-scale. This

is not exact at the western boundary of the H II region (see Sect. 6.3), where also advection effects may have a significant impact on the ionization balance, as pointed out in Sect. 6.4. A model including time-dependent plasma-effects may considerably improve the understanding of the observed absorption and emission features and could be the subject of future studies.

9.3 Conclusions and Outlook

The results of the combination of observations with hydrodynamic and plasma simulations presented in this work show that the circumstellar envelope of the α Sco system is strongly influenced by dynamic effects. A calculation of absorption line profiles based on the simulated density and velocity distributions and ionization structure, and a comparison to HST/GHRS and VLT/UVES spectra reveal that the mass-loss rate was underestimated by a factor of two in earlier studies that were based on an undisturbed, spherically symmetric circumstellar shell. The resulting mass-loss rate of $\dot{M} = 2 \times 10^{-6}\ M_{\odot}\,\mathrm{yr}^{-1}$ is confirmed by an analysis of the Hα emission from the Antares nebula, which is based on spatially resolved emission distributions observed with VLT/UVES.

The theoretical absorption line profiles exhibit a multi-component structure as a natural result of the influence of the hot H II region that is moving with the B star through the wind of the primary. Three of the four observed components can be explained accordingly. However, the origin of the additional component at $-14\ \mathrm{km\,s}^{-1}$ seen in most absorption lines (Fig. 7.5) remains uncertain and is probably an indication of time-dependent mass-loss.

The structure of the [Fe II] line emission of the Antares nebula as observed with VLT/UVES cannot be reproduced correctly. A more sophisticated model including exact radiative transfer calculations and time-dependent simulations of the ionization balance allowing for advection effects would help to understand the remaining discrepancies between theory and observations. In this context, it would be desirable to parallelize the hydro code, which will make it possible to calculate a more extensive grid of models. Future projects may deal with these improvements of the model calculations.

Appendix A

Computational details

A.1 The temperature grid

For the calculation of the 3D temperature distribution, The 1D models calculated with Cloudy are distributed homogeneously in 3D space, i. e. with a constant increment in θ. The angle θ is measured from the upper pole, i. e. from the positive z direction in the AMRCART coordinate system, downwards, and the angle ϕ is measured counterclockwise from the direction towards the supergiant. The increment in ϕ in the plane of the orbit, i. e. at $\theta = \pi/2$, equals the increment in θ, which is determined by a given number N according to $\Delta\theta = \pi/(N-1)$. Only odd numbers are used for N so that there are always two models describing the temperature distribution on the line connecting the two stars, one away from the primary star, one towards it. In directions nearer to the poles, $\Delta\phi$ is increased according to $\Delta\phi = \pi/(N \sin\theta - 1)$, where the expression $N \sin\theta$ is rounded to the nearest integer that is ≥ 2. For $\theta = 0$ and $\theta = \pi$ one direction ($\phi = 0$) is calculated.

Thus, the total number of Cloudy simulations computed to cover the whole domain for a given N is

$$N_{\mathrm{Cl}} = 2 + \sum_{i=1}^{N-2} 2(N_i - 1), \tag{A.1}$$

where N_i is the number of directions calculated for a given $\theta_i = i\Delta\theta$,

$$N_i = \begin{cases} N \sin\theta_i, & \sin\theta_i \geq 2/N \\ 2, & \text{else} \end{cases}. \tag{A.2}$$

As the Cloudy simulations are independent of each other, they can be safely executed on different CPUs. The minimum wall-clock time is reached when the number of processors available for the simulation equals N_{Cl} (cf. Eq. 5.25). The simulations presented in this work are symmetric with respect to the orbital plane so that it is sufficient to cover only the lower half of the domain, i. e.

$$N_{\mathrm{Cl}}^{\mathrm{sym}} = 1 + \sum_{i=(N-1)/2}^{N-2} 2(N_i - 1). \tag{A.3}$$

A.2 Definition of atan2

The ordinary arctan function only gives results in the range $(-\pi/2, \pi/2)$. The calculation of some of the angles defined in Sect. 5.2.3 requires a function that gives values in the range (-π, π]. For such purposes a function with two arguments is defined as follows.

$$\mathrm{atan2}(y,x) = \begin{cases} \arctan\frac{y}{x}, & x > 0 \\ \arctan\frac{y}{x} + \pi, & x < 0, y \geq 0 \\ \arctan\frac{y}{x} - \pi, & x < 0, y < 0 \\ \frac{\pi}{2}, & x = 0, y > 0 \\ -\frac{\pi}{2}, & x = 0, y < 0 \\ 0 & x = 0, y = 0 \end{cases} \tag{A.4}$$

A.3 Data exchange between AMRCART and Cloudy

A.3.1 Passing density information from AMRCART to Cloudy

As AMRCART uses an adaptive mesh the spatial resolution of the density information is not the same for all parts of the grid. The A-MAZE package provides a code that can generate a grid of the density or other variables with a uniform resolution. I integrated this code as a subroutine into AMRCART so that the density information can be passed to Cloudy on a regular grid.

As the orbit of the α Sco system is assumed to be circular the edge lengths in x_{AC} and y_{AC} direction are always equal ($a_x = a_y = a$), while the edge length in z_{AC} direction can be smaller ($a_z \leq a$). As the resolution is equal in all directions, the ratio of the number of grid points along an edge of the computational domain in x_{AC} (y_{AC}) direction N_ρ and the number of points in z direction $N_{\rho,z}$ is

$$\frac{N_\rho}{N_{\rho,z}} = \frac{a}{a_z}. \tag{A.5}$$

The density information is passed to Cloudy in the form of a one-dimensional array with $N_\rho^2 N_{\rho,z}$ elements. When the density routine of a Cloudy simulation representing the (θ, ϕ) direction as seen from the secondary star (cf. Sect. 5.2.3) requests the density at a radial distance r, first the corresponding coordinates $\boldsymbol{r}_{\mathrm{AC}}$ in the AMRCART system are calculated via Eqs. 5.32 and 5.33. These coordinates are transformed to the integer values

$$\begin{pmatrix} i \\ j \\ k \end{pmatrix} = N_\rho \begin{pmatrix} x_{\mathrm{AC}} \\ y_{\mathrm{AC}} \\ z_{\mathrm{AC}} \end{pmatrix}, \tag{A.6}$$

where the integers on the left-hand side are obtained by rounding up the values on the right-hand side. If the elements of the density array are numbered starting from 1 these coordinates correspond to the element number $i+(j-1)N_\rho+(k-1)N_\rho^2$.

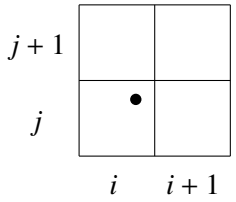

Figure A.1: Linear interpolation on the cartesian grid in the *xy* plane. The filled circle marks the position $(x_{\mathrm{AC}}, y_{\mathrm{AC}})$.

In order to improve the smoothness of the density data passed to Cloudy, a linear interpolation involving the adjacent grid cells is performed (cf. Press et al. 2007, pp. 132f.). Figure A.1 shows a typical situation projected onto a two-dimensional (2D) plane. The interpolated density resulting from these four grid cells is given by

$$\begin{aligned}\rho_{\mathrm{int},k} &= (1-\Delta x)(1-\Delta y)\rho_{i,j,k} + \Delta x(1-\Delta y)\rho_{i+1,j,k} + \\ &\quad \Delta x\Delta y\rho_{i,j+1,k} + (1-\Delta x)\Delta y\rho_{i+1,j+1,k}, \end{aligned} \tag{A.7}$$

where $\Delta x = x_{\mathrm{AC}}N_\rho - (i-0.5)$, $\Delta y = y_{\mathrm{AC}}N_\rho - (j-0.5)$, and $\rho_{i,j,k}$ is the $(i+(j-1)N_\rho + (k-1)N_\rho^2)$th element of the 1D density-array. This calculation is performed once again with the four adjacent grid cells on the nearest z level ($k-1$ or $k+1$), and the final value of the interpolated density is obtained by the simple interpolation

$$\rho_{\mathrm{int}} = \rho_{\mathrm{int},k\pm1} + \Delta z(\rho_{\mathrm{int},k} - \rho_{\mathrm{int},k\pm1}) \tag{A.8}$$

with $\Delta z = z_{\mathrm{AC}}N_{\rho,xy} - (k-0.5)$.

A.3.2 Coordinates used in the temperature interpolation

The positions of the corners of the rectangle shown in Fig. 5.4 in cartesian coordinates read

$$\boldsymbol{r}_1 = r_1\begin{pmatrix}\sin\theta_1\cos\phi_{\theta_1,1}\\ \sin\theta_1\sin\phi_{\theta_1,1}\\ \cos\theta_1\end{pmatrix},\ \boldsymbol{r}_2 = r_2\begin{pmatrix}\sin\theta_1\cos\phi_{\theta_1,2}\\ \sin\theta_1\sin\phi_{\theta_1,2}\\ \cos\theta_1\end{pmatrix}, \tag{A.9}$$

$$\boldsymbol{r}_3 = r_3\begin{pmatrix}\sin\theta_2\cos\phi_{\theta_2,1}\\ \sin\theta_2\sin\phi_{\theta_2,1}\\ \cos\theta_2\end{pmatrix},\ \text{and}\ \boldsymbol{r}_4 = r_4\begin{pmatrix}\sin\theta_2\cos\phi_{\theta_2,2}\\ \sin\theta_2\sin\phi_{\theta_2,2}\\ \cos\theta_2\end{pmatrix}, \tag{A.10}$$

and the positions of the points P and S are given by

$$\boldsymbol{r} = r\begin{pmatrix}\sin\theta\cos\phi\\ \sin\theta\sin\phi\\ \cos\theta\end{pmatrix},\ \text{and}\ \boldsymbol{r}_S = r_S\begin{pmatrix}\sin\theta\cos\phi\\ \sin\theta\sin\phi\\ \cos\theta\end{pmatrix},\ \text{respectively.} \tag{A.11}$$

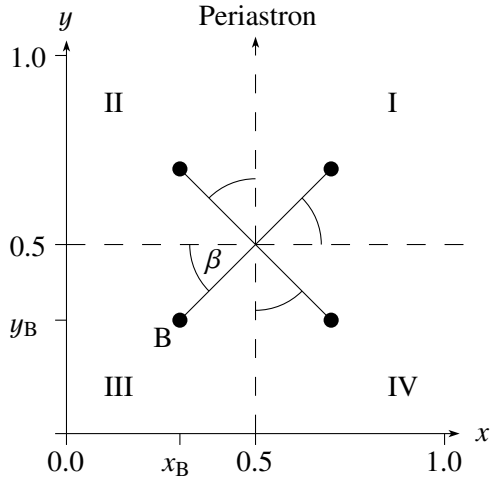

Figure A.2: The angle β is measured relative to one of the borders of the corresponding quadrant in the AMRCART domain.

The vector $\boldsymbol{d}_2$ that is used for the determination of r_S/r is chosen according to the rule

$$\boldsymbol{d}_2 = \begin{cases} \boldsymbol{r}_3 - \boldsymbol{r}_1, & \left|\phi - \phi_{\theta_2,1}\right| \leq \left|\phi - \phi_{\theta_2,2}\right| \\ \boldsymbol{r}_4 - \boldsymbol{r}_1, & \text{else} \end{cases}. \tag{A.12}$$

A.4 Calculation of ZETAUR input-parameters

With the given coordinates (x_B, y_B, z_B) of the secondary star in the AMRCART coordinate system the input parameters for ZETAUR for the calculation of line profiles in the spectrum of α Sco B (see Sect. 7.2.1) are calculated for the corresponding quadrant in the AMRCART domain (see Fig. A.2) according to the following equations.

- Quadrant I ($x > 0.5$, $y \geq 0.5$):

$$\beta = \arctan\frac{y - 0.5}{x - 0.5} \tag{A.13}$$

$$\omega = \frac{\pi}{2} + \delta - \beta \tag{A.14}$$

$$f = \frac{\pi}{2} + \beta \tag{A.15}$$

$$\gamma = \pi - \delta + \beta \tag{A.16}$$

- Quadrant II ($x \leq 0.5$, $y > 0.5$):

$$\beta = \arctan \frac{0.5 - x}{y - 0.5} \tag{A.17}$$

$$\omega = \begin{cases} \delta - \beta, & \beta \leq \delta \\ 2\pi - \beta + \delta, & \text{else} \end{cases} \tag{A.18}$$

$$f = \pi + \beta \tag{A.19}$$

$$\gamma = \frac{3}{2}\pi - \delta + \beta \tag{A.20}$$

- Quadrant III ($x < 0.5$, $y \leq 0.5$):

$$\beta = \arctan \frac{0.5 - y}{0.5 - x} \tag{A.21}$$

$$\omega = \frac{3}{2}\pi + \delta - \beta \tag{A.22}$$

$$f = \frac{3}{2}\pi + \beta \tag{A.23}$$

$$\gamma = \begin{cases} 2\pi - \delta + \beta, & \beta < \delta \\ \beta + \delta, & \text{else} \end{cases} \tag{A.24}$$

- Quadrant IV ($x \geq 0.5$, $y < 0.5$):

$$\beta = \arctan \frac{x - 0.5}{0.5 - y} \tag{A.25}$$

$$\omega = \pi + \delta - \beta \tag{A.26}$$

$$f = \beta \tag{A.27}$$

$$\gamma = \frac{\pi}{2} - \delta + \beta \tag{A.28}$$

The true anomaly f relates to the time of periastron passage via

$$T_0 = T_{\text{obs}} - \frac{f}{2\pi} P, \tag{A.29}$$

where T_{obs} is the JD of the observation and P the orbital period. γ is the angle between the periastron passage and the total eclipse, i. e.

$$\Delta T_{\text{ecl}} = \frac{\gamma}{2\pi} P. \tag{A.30}$$

Fig. A.3 shows an example with the B star in quadrant II. For a circular orbit ω has no physical meaning and is only used as an angular offset for the data input from the hydrodynamic results.

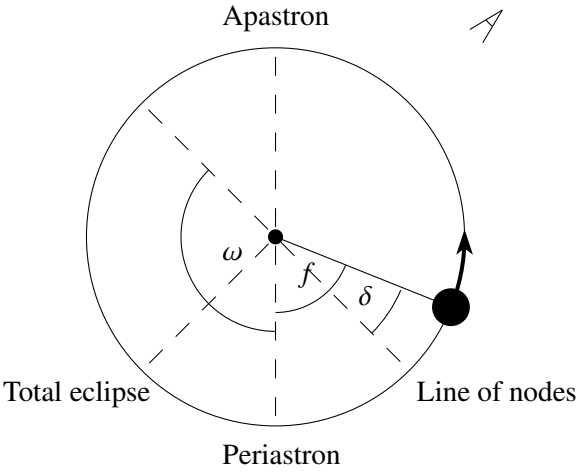

Figure A.3: ZETAUR input parameters for the line profile analysis of the observations described in Sect. 7.2.

Bibliography

Baade, R. 1998, in ESA Special Publication, Vol. 413, Ultraviolet Astrophysics Beyond the IUE Final Archive, ed. W. Wamsteker, R. Gonzalez Riestra, & B. Harris, 325–332

Baade, R., Kirsch, T., Reimers, D., et al. 1996a, ApJ, 466, 979

Baade, R., Kirsch, T., & Toussaint, F. 1996b, in Astronomical Society of the Pacific Conference Series, Vol. 109, Cool Stars, Stellar Systems, and the Sun, 9th Cambridge workshop, ed. R. Pallavicini & A. K. Dupree (San Francisco: Astronomical Society of the Pacific), 513–514

Baade, R. & Reimers, D. 2007, A&A, 474, 229

Barlow, M. J., Smith, L. J., & Willis, A. J. 1981, MNRAS, 196, 101

Barmin, A. A., Kulikovskiy, A. G., & Pogorelov, N. V. 1996, Journal of Computational Physics, 126, 77

Berger, M. J. & Colella, P. 1989, Journal of Computational Physics, 82, 64

Berger, M. J. & Oliger, J. 1984, Journal of Computational Physics, 53, 484

Bernat, A. P. 1977, ApJ, 213, 756

Bernat, A. P. 1982, ApJ, 252, 644

Bressan, A., Fagotto, F., Bertelli, G., & Chiosi, C. 1993, A&AS, 100, 647

Brott, I., de Mink, S. E., Cantiello, M., et al. 2011, A&A, 530, A115+

Cardelli, J. A. 1984, AJ, 89, 1825

Castor, J. I., Abbott, D. C., & Klein, R. I. 1975, ApJ, 195, 157

Che, A., Hempe, K., & Reimers, D. 1983, A&A, 126, 225

Curé, M., Cidale, L., & Granada, A. 2011, ApJ, 737, 18

Danchi, W. C., Bester, M., Degiacomi, C. G., Greenhill, L. J., & Townes, C. H. 1994, AJ, 107, 1469

Dekker, H., D'Odorico, S., Kaufer, A., Delabre, B., & Kotzlowski, H. 2000, in Society of Photo-Optical Instrumentation Engineers (SPIE) Conference Series, Vol. 4008, Optical and IR Telescope Instrumentation and Detectors, ed. M. Iye & A. F. Moorwood, 534–545, ISBN 978-0-81-943633-7

Deutsch, A. J. 1956, ApJ, 123, 210

D'Odorico, S., Cristiani, S., Dekker, H., et al. 2000, in Society of Photo-Optical Instrumentation Engineers (SPIE) Conference Series, Vol. 4005, Discoveries and Research Prospects from 8- to 10-Meter-Class Telescopes, ed. J. Bergeron, 121–130, ISBN 978-0-81-943630-6

ESA, ed. 1997, ESA SP, Vol. 1200, The Hipparcos and Tycho catalogues

Evans, D. S. 1967, in IAU Symposium, Vol. 30, Determination of Radial Velocities and their Applications, ed. A. H. Batten & J. F. Heard (London: Academic Press), 57–62

Ferland, G. J., Korista, K. T., Verner, D. A., et al. 1998, PASP, 110, 761

Fletcher, C. A. J. 1991, Computational Techniques for Fluid Dynamics 1. Fundamental and General Techniques, 2nd edn., Springer Series in Computational Physics (Berlin et al.: Springer-Verlag), ISBN 3-540-53058-4

Garhart, M. P., Smith, M. A., Turnrose, B. E., Levay, K. L., & Thompson, R. W. 1997, IUE NASA Newsletter, 57, 1, http://archive.stsci.edu/iue/manual/newsips/ (June 21, 2011)

Gräfener, G. & Hamann, W.-R. 2008, A&A, 482, 945

Haas, M. R., Glassgold, A. E., & Tielens, A. G. G. M. 1995, in ASP Conference Series, Vol. 73, Airborne Astronomy Symposium on the Galactic Ecosystem: From Gas to Stars to Dust, ed. M. R. Haas, J. A. Davidson, & E. F. Erickson, Astronomical Society of the Pacific, 397–404, ISBN 0-937707-92-9

Hagen, H.-J., Hempe, K., & Reimers, D. 1987, A&A, 184, 256

Hagen, W. 1978, ApJS, 38, 1

Hagen, W. 1982, PASP, 94, 835

Heap, S. R., Brandt, J. C., Randall, C. E., et al. 1995, PASP, 107, 871

Hempe, K. 1982, A&A, 115, 133

Henney, W. J., Arthur, S. J., Williams, R. J. R., & Ferland, G. J. 2005, ApJ, 621, 328

Hjellming, R. M. & Newell, R. T. 1983, ApJ, 275, 704

Hopmann, J. 1958, Mitteilungen der Universitätssternwarte Wien, 9, 135

Kudritzki, R.-P. & Puls, J. 2000, ARA&A, 38, 613

Kudritzki, R. P. & Reimers, D. 1978, A&A, 70, 227

Lafon, J.-P. J. & Berruyer, N. 1991, A&A Rev., 2, 249

Lamers, H. J. G. L. M. 1997, in Lecture Notes in Physics, Vol. 497, Stellar Atmospheres: Theory and Observations, ed. J. P. De Greve, R. Blomme, & H. Hensberge, European Astrophysics Doctoral Network (EADN) (Berlin et al.: Springer-Verlag), 159–185

Lamers, H. J. G. L. M. & Cassinelli, J. P. 1999, Introduction to Stellar Winds (Cambridge, UK: Cambridge University Press), ISBN 0-521-59565-7

Lanz, T. & Hubeny, I. 2007, ApJS, 169, 83

Lax, P. D. 1954, Communications on Pure and Applied Mathematics, 7, 159

Marsch, E. 2006, Living Reviews in Solar Physics, 3, URL (accessed on July 14, 2011): http://www.livingreviews.org/lrsp-2006-1

Marsh, K. A., Bloemhof, E. E., Koerner, D. W., & Ressler, M. E. 2001, ApJ, 548, 861

Mihalas, D. 1978, Stellar atmospheres, 2nd edn., ed. G. & M. Burbidge, A Series of Books in Astronomy and Astrophysics (San Francisco: W. H. Freeman and Company)

Moore, C. E. 1952, in Circular of the National Bureau of Standards, Vol. 488, An ultraviolet multiplet table, ed. Moore, C. E. (Washington: US Government Printing Office)

Morton, D. C. 2003, ApJS, 149, 205

Ofman, L. 2010, Living Reviews in Solar Physics, 7, URL (accessed on July 13, 2011): http://www.livingreviews.org/lrsp-2006-4

Parker, E. N. 1958, ApJ, 128, 664

Parker, E. N. 1960, ApJ, 132, 175

Pauldrach, A., Puls, J., & Kudritzki, R. P. 1986, A&A, 164, 86

Press, W. H., Teukolsky, S. A., Vetterling, W. T., & Flannery, B. P. 1992, Numerical recipes in C. The art of scientific computing, 2nd edn. (Cambridge, UK: Cambridge University Press)

Press, W. H., Teukolsky, S. A., Vetterling, W. T., & Flannery, B. P. 2007, Numerical recipes. The art of scientific computing, 3rd edn. (Cambridge, UK, et al.: Cambridge University Press), ISBN 978-0-521-88068-8

Puls, J., Vink, J. S., & Najarro, F. 2008, A&A Rev., 16, 209

Ralchenko, Y., Kramida, A. E., Reader, J., et al. 2011, NIST Atomic Spectra Database (ver. 4.1.0), URL (accessed on June 20, 2011): http://physics.nist.gov/asd3, National Institute of Standards and Technology, Gaithersburg, MD

Reimers, D. 1975, Mémoires de la Société Royale des Sciences de Liège, 8, 369

Reimers, D. 1987a, in IAU Symposia Proceedings, Vol. 122, Circumstellar Matter, ed. I. Appenzeller & C. Jordan (Dordrecht: Reidel Publishing Company), 307–318, ISBN 90-277-2512-8

Reimers, D. 1987b, in Lecture Notes in Physics, Berlin Springer Verlag, Vol. 292, Solar and Stellar Physics. Proceedings of the 5th European Solar Meeting, ed. E.-H. Schröter & M. Schüssler, European Physical Society (Berlin et al.: Springer-Verlag), 139–156, ISBN 3-540-18678-6

Reimers, D., Hagen, H.-J., Baade, R., & Braun, K. 2008, A&A, 491, 229

Rybicki, G. B. 1984, in Methods in Radiative Transfer, ed. Kalkofen, W. (Cambridge, UK: Cambridge University Press), 21–64

Sanner, F. 1976a, ApJ, 204, L41

Sanner, F. 1976b, ApJS, 32, 115

Smith, M. A., Patten, B. M., & Goldberg, L. 1989, AJ, 98, 2233

Snow, Jr., T. P., Buss, Jr., R. H., Gilra, D. P., & Swings, J. P. 1987, ApJ, 321, 921

Suzuki, T. K. & Inutsuka, S. 2005, ApJ, 632, L49

Toro, E. F. 1999, NUMERICA: A Library of Source Codes for Teaching, Research and Applications, URL (accessed on May 17, 2010): http://www.numeritek.com/, (Cheadle Hulme, UK: Numeritek Ltd.)

Toro, E. F. 2009, Riemann Solvers and Numerical Methods for Fluid Dynamics. A Practical Introduction, 3rd edn. (Berlin: Springer-Verlag), ISBN 978-3-540-25202-3

Tuthill, P. G., Haniff, C. A., & Baldwin, J. E. 1997, MNRAS, 285, 529

van der Hucht, K. A., Bernat, A. P., & Kondo, Y. 1980, A&A, 82, 14

van Leeuwen, F. 2007, Astrophysics and Space Science Library, Vol. 350, Hipparcos, the New Reduction of the Raw Data (Berlin: Springer Science + Business Media B. V.)

Verner, E. M., Verner, D. A., Korista, K. T., et al. 1999, ApJS, 120, 101

Vink, J. S., Muijres, L. E., Anthonisse, B., et al. 2011, A&A, 531, A132+

Walder, R. & Folini, D. 2000, in Astronomical Society of the Pacific Conference Series, Vol. 204, Thermal and Ionization Aspects of Flows from Hot Stars, ed. H. Lamers & A. Sapar, 281–286

Walder, R. & Folini, D. 2003, in IAU Symposium, Vol. 212, A Massive Star Odyssey: From Main Sequence to Supernova, ed. K. van der Hucht, A. Herrero, & C. Esteban, 139–147

Willson, L. A. 2000, ARA&A, 38, 573

Willson, L. A. 2009, in ASP Conference Series, Vol. 412, The Biggest, Baddest, Coolest Stars, ed. D. G. Luttermoser, B. J. Smith, & R. E. Stencel, Astronomical Society of the Pacific, San Francisco, 137–148

Acknowledgments

The present thesis was accomplished in the framework of my PhD studies at the Hamburger Sternwarte, and I wish to express my gratitude to the people who have contributed to its completion. First of all, I would like to thank Dieter Reimers for the interesting research topic and his support in the accomplishment and funding of my work, and Robert Baade for many helpful discussions and for carefully reading and commenting the manuscript of this text. I also wish to thank Peter Hauschildt for providing me access to the computing facilities that I used for most of the simulations presented in this work. Finally, I thank the Universität Hamburg for a grant for the last year of my PhD studies.